June 2021

Modeling, Control and Analysis of Inverter-Based Generators in the Power Grids

Yangkun Xu
University of South Florida

Scholar Commons Citation

Xu, Yangkun, "Modeling, Control and Analysis of Inverter-Based Generators in the Power Grids" (2021). *USF Tampa Graduate Theses and Dissertations.*
https://digitalcommons.usf.edu/etd/9734

Modeling, Control and Analysis of Inverter-Based Generators in the Power Grids

by

Yangkun Xu

A dissertation submitted in partial fulfillment
of the requirements for the degree of
Doctor of Philosophy
Department of Electrical Engineering
College of Engineering
University of South Florida

Major Professor: Zhixin Miao, Ph.D.
Lingling Fan, Ph.D.
Chung Seop Jeong, Ph.D.
Achilleas Kourtellis, Ph.D.
Kaiqi Xiong, Ph.D.

Date of Approval:
June 16, 2021

Keywords: Subsynchronous oscillation (SSO), Frequency coupling, Stability analysis, Hybrid Boost Converter (HBC)

Dedication

To my loving parents and my girlfriend

Acknowledgments

First and foremost, I would like to express my sincerest appreciation to my advisor Dr. Zhixin Miao for his support and encouragement during my Ph.D. studies. He does the best he can to make learning easier for me not only researching on the hot topics, but also providing me the excellent research environment.

I would also like to thank Dr. Lingling Fan. Her deep knowledge, extensive experience, endless guidance, and sharp insights had a serious influence on my growth, both as an individual and as a professional.

Secondly, I would like to truly thank the rest of my committee members: Dr. Chung Seop Jeong, Dr. Achilleas Kourtellis, Dr. Kaiqi Xiong, and Dr. Pei-Sung Lin for their encouragement, helpful comments, and suggestions. I would like to extend my special gratitude to Dr. Christos Ferekides, Dr. Jane Harvey, Dr. Jennifer Schneider, †Dr. Ralph Fehr, Dr. Yingzhong Gu and Dr. Jin Tan who have encouraged and inspired me along my Ph.D. journey.

I owe my thanks to my former and recent colleagues from the smart grid power system lab, in particular: Dr. Vahid Rasouli, Dr. Lakshan Piyasinghe, Dr. Javad Khazaei, Dr. Ahmad Tazay, Dr. Anas Almunif, Yan Ma, Dr. Yin Li, Dr. Minyue Ma, Dr. Alqahtani Mohammed, Yi Zhou, Li Bao, Miao Zhang, Rabi Kar, Sulaiman Almutairi, Abdullah Alassaf, Zhengyu Wang, Ratik Mittal, Huazhao Ding ... to name but a few! Thank you for all the discussions, help and enjoyable time I spent with them over the years at the office.

Last but not least, I would like to especially thank my love, Lulu Wei, my father, Chunhong Xu, and my mother, Lanping Yang for unconditional love, support, and encouragement. Without you, I would not have been able to survive and thrive in my Ph.D. program.

For above peoples, thank you from the bottom of my heart for… everything!

Table of Contents

List of Tables

List of Figures

Abstract

Nowadays, the inverter-based generators (IBGs) has been exponentially integrated into the power grid due to environment and energy saving concerns. However, the high penetration of low inertia IBGs brings new problems on the system stability. The main objectives of this dissertation are to: 1- carry out large-signal analysis to identify the stability issues and small-signal analysis to assess the stability of the power systems, and 2- provide a standard measuring procedure to identify the admittance of IBGs. In addition, investigation on a novel DC-based IBGs architecture is carried out. In this dissertation, one widely used IBG is investigated: Type-4 wind turbine generators (WTGs).

The first part of the research conducts a thorough analysis including validation, identification of potential stability risks, and in-depth physical insights on the stability issues for high penetration of grid integrated type-4 wind. The state-space based time-domain modeling approach is employed. The power grid considers Texas transmission grid's characteristics and adopts two assumptions: noncompensated network with weak grid consideration and series compensated network with weak grid consideration. The latter is used to shorten electric distance of transmission lines. The stability issue manifests as subsynchronous oscillation (SSO) in the research. To investigate the SSO issue, small-signal stability analysis is required, which requires building linearized analytical models with state variables constant at steady-state. Thus, the state-space analytical models are developed based on the different grid-side converter (GSC)'s control mode. Eigenvalue analysis and participation factor analysis are then carried out to offer an entire picture of system modes and further identify influencing factors. Because the analytical model is a simplified model which only include the essential dynamics, a rigorous validation will be carried out to validate the analysis results against the simulation results from EMT testbeds including full dynamics.

The second part of the research focuses on identifying the SSO issue using admittance-based frequency-domain modeling approach. Impedance models can be efficiently derived as the frequency-domain transfer function from the analytical models with device's terminal voltage treated as the input and the current flowing into the device as the output. But if IBGs are black boxes, the measurements-based approach to find the frequency-domain impedance is prevailing. The impedance or admittance model of IBGs can be obtained by either perturbation-based experiments (e.g., frequency scan) or time-domain data-based identification (e.g., Eigensystem Realization Algorithm (ERA) method relying on step responses). The resulting current/voltage ratio is the admittance measurement, which can be a scalar or a matrix. The scalar admittance is suitable to assess SSO for type-3 wind. However, it has limitation on stability analysis of type-4 wind grid integration systems due to strong frequency-coupling effect. This part provides the theoretic derivation to shed insights on frequency coupling effect observed in the static *abc*-frame, and provides a clear guide line of sequence-domain admittance measuring procedure. Furthermore, with a system splitting into a source and a load subsystem, the ratio of the source-load impedance can be used to determine stability using Nyquist stability criterion. Meanwhile, s-domain admittance model-based eigenvalue analysis can be employed to give an entire picture of the system poles and their trajectories for a varying parameter.

In addition to the modeling and analysis work, this dissertation also includes investigation on a single-stage multi-port hybrid boost converter (HBC) to regulate the dc and ac loads simultaneously, provide a high voltage gain ratio, while maintaining the closed-loop stability of the entire power system. The HBC features the simple architecture reducing the unnecessary processes of dc/dc and dc/ac conversions compared with conventional architecture of DC-based power system. This part provides the critical aspects of the operation of the HBC including the grid-following control strategy and hybrid pulse width modulation methodology.

This dissertation has led to one accepted IEEE transaction paper and one journal paper in revision process.

Chapter 1: Introduction

1.1 Background

Nowadays, the inverter-based generators (IBGs), such as wind turbine generators (WTGs) and solar photovoltaics (PVs), has been exponentially integrated into the power grid due to environment and energy saving concerns. It is estimated that wind and solar PV will provide 20% and 14% respectively of the nation's electricity generation in 2030 [1, 2]. In the past, the power system dynamics were largely dominated by the characteristics of the synchronous generators. Whereas nowadays, the rapid increasing penetration of the IBGs is beginning to predominantly affect the dynamics of modern power system. The dynamic responses of IBGs (defined by controllers) differ from conventional synchronous generators (defined by flux linkage, etc.).

Grid operators now facing operational situation that the generation from IBGs displaces substantial amount of generation from synchronous generators. IBGs are interfaced with the power grid through power electronic inverters. A challenge is the interaction between IBGs and power grid introducing the stability issues to the power systems. For example, subsynchronous oscillations (SSO) events are frequently observed in the IBGs integrated system since 2009.

In response to aforementioned challenges, grid planners and operators are analyzing the dynamic performance of the power system to show how IBGs behave and how to assess the stability and security of power systems. Special focuses are placed on the modeling of IBGs used in power system dynamic studies. Furthermore, the new controllers or control algorithms for IBGs are designed to provide fast dynamic response capability to contingency events.

1.2 Statement of Problems

1.2.1 IBGs under Weak Grid Conditions

The grid strength is generally indicated by the short circuit ratio (SCR), which is defined as the ratio of short circuit power capacity S_c at the point of common coupling (PCC) bus to the rated power of the installed capacity of the wind farm S_N

$$SCR = \frac{S_c}{S_N} = \frac{V_g^2/Z_g}{V_g^2/Z_N} \approx \frac{1}{Z_g^{pu}} \tag{1.1}$$

where Z_g is the real value of the short circuit impedance, Z_N is the impedance base based on the rated grid voltage V_g, and Z_g^{pu} is the per unit value of the short circuit impedance of the AC grid. According to the IEEE Standard 1204-1997 [3], the AC grid can be classified as:

- Strong grid with a high SCR value (SCR>3)
- Weak grid with a low SCR value (2≤SCR≤3)
- Very weak grid with a very low SCR value (SCR<2)

Large scale IBGs are usually located in the remote areas far from the load centers. A long transmission line results in the large grid impedance. As a result, the grid strength becomes weak.

Real-world stability issues due to voltage-source converter (VSC) with weak grid interconnection have been studied in the literature [4–8]. Most of oscillations manifest as low-frequency oscillations which have been observed in an offshore wind farm of United Kingdom [9], solar PV system of California [10], etc. In 2015, Subsynchronous oscillations (SSO) events were observed in the type-4 wind in the Xinjiang Uygur Autonomous Region, China [6]. As shown in Fig. 1.1, most of wind farms are installed at substation A and B. With the increasing installed wind power capacity, the SCR is low (about 1.3 or even less), and thus the AC grid becomes relatively weak. The power experiences oscillations from 20 Hz to 40 Hz during SSO events. Such power oscillations would even spread to the whole main grid and triggered torsional vibration on shafts of turbo-generators in the remote thermal power plants because oscillation frequencies matched torsional frequencies in some of turbo-generators. Eventually, those affected generators were disconnected from the main grid.

1.2.2 IBGs in Series Compensated Networks

Weak grid is one of major factors that makes the system stability worse. An efficient method to strong grid is implementing series compensation on long extra-voltage transmission line. The series

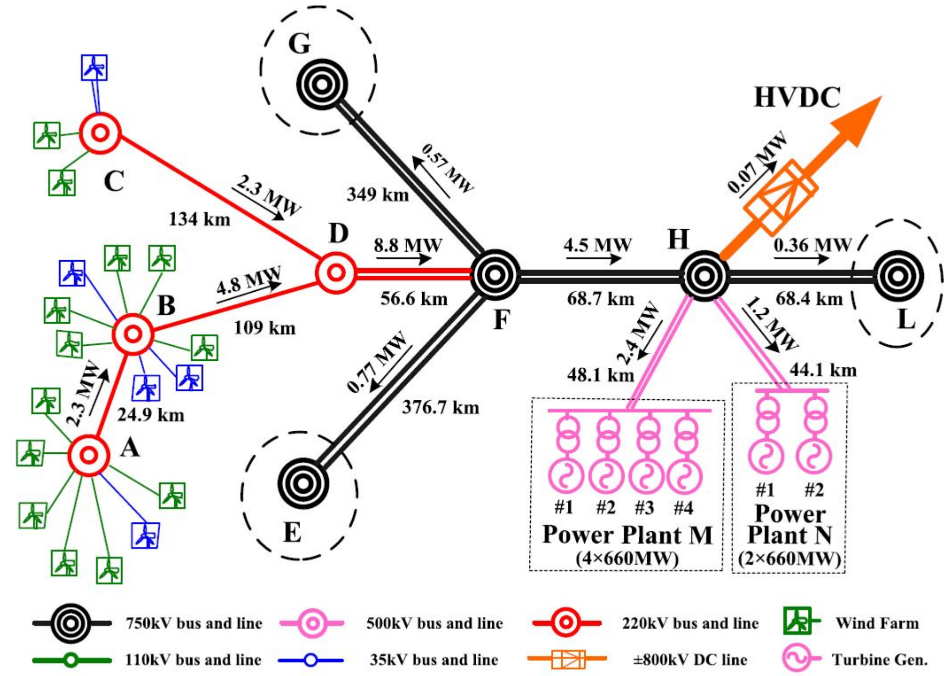

Figure 1.1: Wind farms with relatively weak AC network in the Xinjiang Uygur Autonomous Region experienced sub-synchronous oscillations in 2014.

compensated network not only increases the power transfer capability, but also improves system stability and provides voltage control. However, it also brings another type of SSO due to the LC resonance. Thus, we also use subsynchronous resonance (SSR) to refer to this type of SSO.

SSR events due to type-3 wind radial connection with series compensated transmission lines have been observed in South Central Minnesota [11], North China [12], and Texas [13, 14]. For example, a SSR event was observed in Electric Reliability Council of Texas (ERCOT) in 2009 [13]. As shown in Fig. 1.2, a single line-to-ground fault tripped the 345 kV Ajo-Lon Hill line. 200 MW type-3 wind radially connected to Rio Hondo 50% series compensated transmission line. The subsynchrnous voltage and currents immediately grew. This in turn causes damages in both series capacitors and wind turbine equipments.

1.3 Motivation and Existing Studies

Inspired by the aforementioned system stability issues, there is a need of accurate dynamic IBGs modeling to carry out the stability analysis. Both state-space models and admittance models will be employed for stability analysis. The purpose of adequate dynamic modeling is to observe

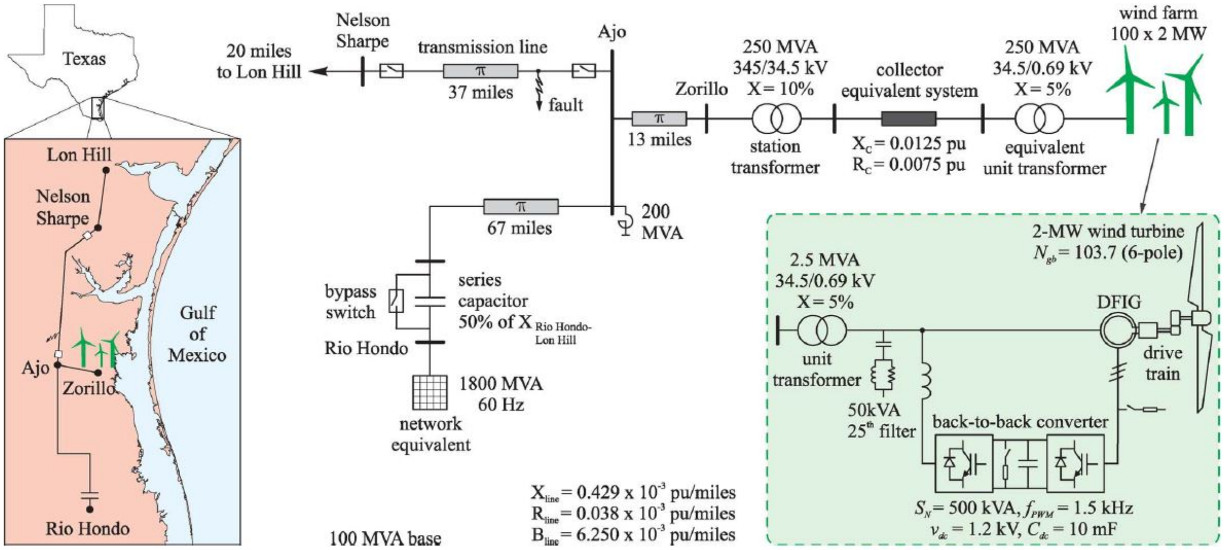

Figure 1.2: Type-3 wind with series-compensated network in the south Texas experienced sub-synchronous oscillations in 2009.

the impact of IBGs on the power grids during contingency events such as tripping of transmission line and offer insights to dynamic phenomena.

1.3.1 IBGs in Series-compensated Network with Weak Grid Condition

SSO have been observed in real world for type-3 wind farms interconnected to series compensated networks. It is natural to pose this question: Are type-4 wind farms immune to SSRs? Very few research exists to address this question except [15] and [16]. PSCAD simulation studies in [15] demonstrate that a type-4 wind with its grid side converter (GSC) in active power and ac voltage control mode is immune from SSR issues. This remark is also stated in [12], where the authors remarked that based on observations from real-world SSR events, type-4 wind made no contribution to SSR. Strong grid assumption is made in the study systems in [12, 15]. But with higher and higher IBGs penetration, weak grid condition is more of a concern.

It is thus natural to examine stability issues of type-4 wind farms in series compensated networks while considering weak grid condition. The only existing research that conducts small-signal stability analysis of type-4 wind farm in series compensated grids with weak grid consideration is [16]. Reference [16] uses analytical modeling approach (impedance-based approach) to study this engineering problem. Type-4 wind turbine's grid side converter (GSC) is assumed in dc-link voltage control mode. The findings of [16] indicate that there are potential stability risks due to non-passivity of type-4 wind admittance in subsynchronous frequency range. GSC control (e.g., PLL parameters, reactive power control), and GSC operating condition (e.g., active power exporting level) influences the non-passivity. While [16] identified potential stability risks due to non-passivity of GSC, non-passivity cannot be used to explain the particular dynamics that may be associated with series compensated network. In addition, the stability analysis method presented in [16] does not offer a whole picture of the entire system's dynamic modes. Validation against electromagnetic transient (EMT) testbeds with full details is also missing.

The particular interest of the research is to offer the quantitative measure and physical insights through the state-space model building and eigenvalue based analysis. The goal is to conduct a thorough analysis with validation and offer insights of potential stability issues in weak and series compensated grids with high penetration of IBGs.

1.3.2 IBGs Admittance Identification for Stability Prediction

From the perspective of the grid industry, wind turbine models are often black boxes supplied by manufacturers. While electromagnetic transient (EMT)-type simulation can provide accurate representation and simulation results, EMT is computing expensive. Thus, the frequency scanning method to find frequency-domain impedance or admittance measurements is a popular tool adopted by the industry for quick screening [17]. With a system splitting into source and load subsystem, the ratio of source-load impedance can be used to determine stability using Nyquist stability criterion [18]. In [19], a simplified type-3 wind impedance model in the static frame is employed to successfully demonstrate SSO in a series compensated network due to induction generator effect.

The impedance or admittance model of a wind turbine or a wind farm can be obtained by frequency scans or the harmonic injection method [20–23]. A measurement testbed is first set up by connecting a wind farm to a perturbation voltage source and a constant voltage source. Varying the perturbation voltage source's frequency, current into the wind farms is analyzed using fast Fourier transform (FFT) to find Fourier coefficients or phasors for the corresponding frequency components. The resulting current/voltage ratio is the admittance measurement.

Positive-sequence impedance has been used in the grid industry and shown to be effective in detecting SSO in the type-3 wind with series compensation [17]. On the other hand, it is found that the positive sequence impedance cannot assess stability accurately for grid-connected converters due to significant frequency-coupling phenomena [24]. This point has been recently confirmed for type-4 wind turbines in [25].

Therefore, it is necessary to establish impedance or admittance including frequency-coupling effect. In the literature, there are two types of admittance models for three-phase converters. Based on the static frame, a sequence-domain model can be measured. Based on the synchronously rotating *dq*-frame, a *dq*-domain admittance can be found. Reference [26] shows that the two types of admittances are equivalent. In [27], sequence-domain admittance is measured for a type-4 wind turbine modeled in an EMT simulation package and used for stability analysis.

While a procedure of sequence-domain admittance measurement is given in [26], there are many subtle details not given. Nor these details can be found in the literature. In addition, there exists confusion in the definition on positive-sequence and negative-sequence components. For example, in [24,26], if the static *abc*-frame's perturbation frequency ω_1 (primary frequency) is notated as the positive sequence frequency, the negative frequency is defined as $\omega_1 - 2\omega_0$ where ω_0 is the nominal frequency. In the case of 70 Hz positive-sequence voltage perturbation in a 60 Hz three-phase system, 50 Hz positive-sequence component and 70 Hz positive-sequence component appear in the current. Based on the notation used in [24], the 70 Hz perturbation in voltage results in 70 Hz positive-sequence component and -50 Hz negative-sequence component. The second component indeed is 50 Hz positive sequence. Thus the notation is confusing. Instead, we adopt the notation of mirror frequency $2\omega_0 - \omega_1$ (also used in [17,28]) as the component indeed appearing in the current when a harmonic component at ω_1 frequency is injected into a voltage. Due to frequency coupling, both primary frequency component and the mirror frequency component will appear. If the mirror frequency is negative, that means the system sees a negative-sequence component.

Furthermore, while the frequency scanning method is the state-of-the-art measurement method, the outcome is admittance measurement, instead of an input/output model or a s-domain admittance. For example, [25] conducted frequency scan and obtained *dq*-domain admittance frequency-domain measurements for a type-4 wind farm. To arrive at a *s*-domain admittance model, frequency-domain data fitting methods, e.g., vector fitting [29], are required as an additional step. Recent research shows that *s*-domain admittance can be found using time-domain data [30] and admittance-based eigenvalue analysis can accurately predict stability compared to Bode plots [31].

The particular interest of the research is to provide the theoretic derivation to shed insights on frequency coupling effect observed in the static *abc*-frame, and provides a clear guide line of sequence-domain admittance measuring procedure. The goal is to demonstrate the effectiveness of stability prediction using the admittance measurements obtained by three methods: frequency scans in the static frame and the *dq*-frame, and time-domain data-based identification.

1.4 Approaches for IBGs Stability Assessment

State-of-the-art methods for IBGs stability analysis is shown in Fig. 1.3. For IBGs grid integration dynamic studies, the research can be carried out using either EMT simulation or small-signal analysis.

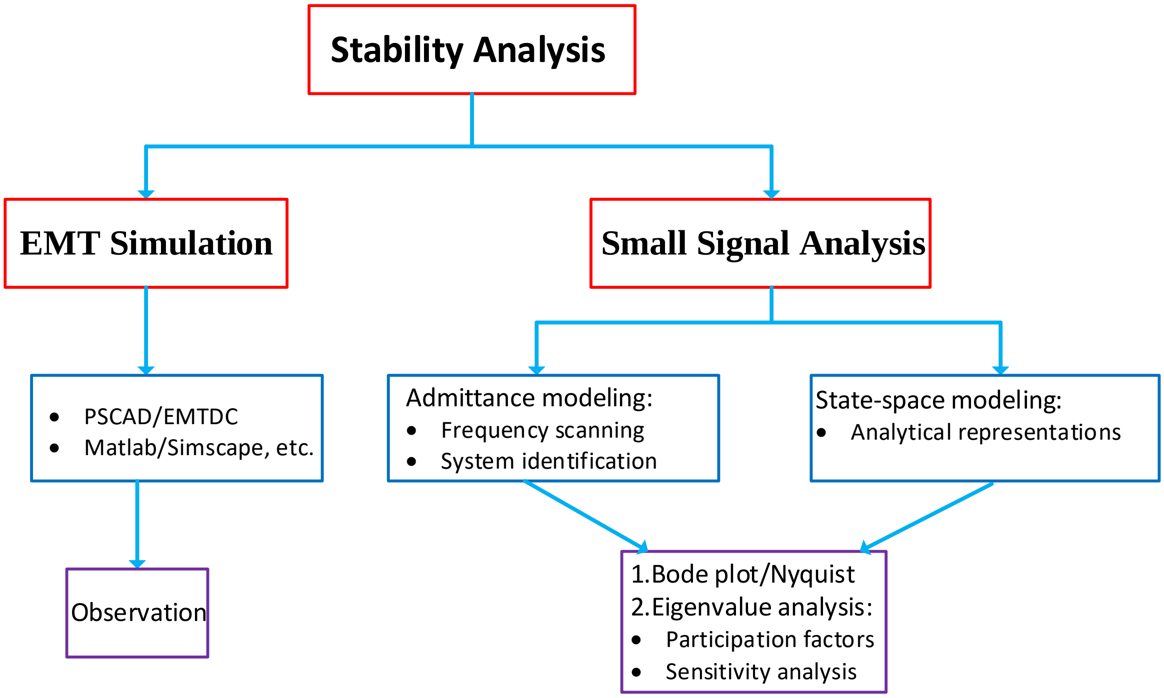

Figure 1.3: State-of-the-art methods for IBGs stability assessment.

Electromagnetic transient (EMT) simulations perform experiment based studies to analyze the particular power system dynamics and to benchmark validation of the accuracy of small-signal analysis in a specific application. The popular simulation tools are MATLAB/Simscape electrical and PSCAD/EMTDC. The EMT model includes full dynamics including electromechanical dynamics, controller dynamics, and protection limitation, etc. However, it cannot offer insights to dynamic phenomena.

For offering in-depth insights, the efficient tool is small signal analysis. There are two major small-signal model building approaches: state-space based time-domain modeling approach which are built with state variables constant at steady-state (e.g., [32,33]) and impedance-based frequency domain modeling approach which are obtained by only the measurements at external terminals (e.g., [18, 34–36]). Both approaches can effectively assess the stability of the system and can be converted to each other through an analytical relation [37].

State-space based approach is normally adopted for the white box devices with knowledge of the internal structure. Imagine a model of IBGs integrated with the power grids, the state variables are discrete due to the switching events. The grid-side converter (GSC) will be replaced with an average model (see section 2.1.3) and is treated as a three-phase *abc*-frame controllable voltage source. The state variables related to voltage and current are periodic at steady-state. The Park's transformation [38] is then employed to convert the *abc*-frame to the *dq*-reference frame. The resulting model has constant state variables at steady-state. With initialization procedures to find the equilibrium points, the model can then be linearized using numerical perturbation (e.g., MATLAB command: `linmod`) at a certain operational condition. The eigenvalue analysis can be conducted to extract oscillation modes from the linearized model and assess the stability of each mode. This approach is described in section 3.3.

Admittance-based approach is suitable for both white box and black box devices. It utilizes most often either the analytical model or measurements to obtain the frequency-domain admittance or impedance using the harmonic injection method through experiments. The outcome is admittance measurement, instead of an input/output model or a s-domain admittance. The system is split into a source and a load subsystem [18]. Based on the ratio of the source-load impedance, Nyquist stability criterion-based analysis will be applied [19]. As indicated by [23], Generalized Nyquist Criterion is not capable of giving an entire picture of the system poles and their trajectories for a varying parameter. As a comparison, eigenvalue analysis relying on Laplace transform has that capabilities but cannot be conducted with only frequency-domain admittance. Admittance-based eigenvalue analysis is only possible when s-domain admittance model is available.

[21] presents a framework of s-domain admittance-based modeling framework, including data-driven admittance identification, network admittance aggregating, and stability analysis via the network admittance. The proposed algorithms and analysis method are to be implemented in various applications. Once the frequency-domain admittance measurements are obtained, the frequency-domain data fitting methods, e.g., vector fitting [29] are employed to find the s-domain admittance model. The s-domain admittance based stability analysis is not a commonly used stability analysis method. This method of finding system eigenvalues through a s-domain admittance was proposed in [39] in 1970s and is elaborated in chapter 4. This method finds few applications due to two reasons. For a simple circuit that can be viewed as a source and a load subsystem, frequency-domain analysis methods such as Generalized Nyquist Criterion are popular. On the other hand, for a sophisticated power grid with many nodes, the state-space modeling approach is popular and has been adopted by major power system dynamic analysis software packages, e.g., PowerTech Lab's SSAT.

1.5 IBGs with Hybrid Boost Converter

In the alternating current (AC)-based power system such as large-scale power plants, the widely used IBG is wind turbine generator which output ac. Both ac/dc rectifier and dc/ac inverters are required. In the direct current (DC)-based power system such as dc microgrids or dc distribution systems, the solar PV panels are advantageous since it has high power quality, low maintenance cost, and suitability in the small-scale plants. Output from solar PV is dc. The dc/ac inverters are required. One of the challenges in the case of high dc voltage applications or grid connected applications is the low dc voltage (15-45 V) of solar PV [40], which in turn, step-up dc/dc converters are needed. The step-up dc voltage gain ratio is desired as large but practically limited on account of the impact of power switches, rectifier diodes, the equivalent series resistance of inductors and capacitors, and the saturation effects of the inductors and capacitors [41]. Very often in the literature is presented that the architecture of DC-based power system employs the step-up dc-dc converter to supply the dc loads and cascade the grid connected voltage source converter (VSC) to step-up dc-dc converter to supply the ac loads [42–44]. This architecture is well understood with extensive research in the recent years. In the case of large penetration of IBGs is integrated into the power grid, separate converter with individual controller is required to achieve dc/dc and dc/ac conversions. This largely increases power loss, system complexity, and reduces the reliability of the entire power system.

Therefore, interests on a novel architecture of the DC-based power system, which aim to reduce the conversion process to a minimum, are growing rapidly. Some of researchers proposed the hybrid boost converter (HBC) [45–48]. The term "HBC" refers to a converter has the capability to provide bidirectional power flow between ac and dc loads simultaneously with the presence of a dc power source. The HBC features the simple architecture reducing the unnecessary processes of dc/dc and dc/ac conversions compared with conventional architecture. The novel architecture will be validated to supply the ac and dc loads simultaneously meanwhile providing a high dc voltage gain ratio in chapter 5.

1.6 Outline of the Dissertation

The structure of the dissertation is organized as follows.

Chapter 1 gives a brief introduction of the IBGs research including background, statement of the problems, motivations, existing studies, and approaches for stability assessment.

Chapter 2 presents detailed characteristics of IBGs in the power grids. The state-of-the-art modeling assumptions of IBGs are introduced to facilitate the system planning and analysis. Furthermore, the cascade vector control structure of VSC in power grid integration is presented.

Chapter 3 presents the modeling and analysis of IBGs in series compensated networks under weak grid conditions. The subsynchronous oscillation (SSO) is investigated in type-4 wind farm. Relying on the analytical models, eigenvalue-based and impedance-based small-signal stability analysis are carried out. It is found that increasing series compensation level, under weak grid conditions, poses oscillatory stability issues due to interaction of a mode associated to the grid-side converter and a mode associated with network LC resonance. The results are validated against two EMT testbeds with full dynamics in MATLAB/Simscape and PSCAD/EMTDC, respectively.

Chapter 4 presents the admittance identification of IBGs for stability prediction. The frequency-coupling impedance modeling of type-3 or type-4 wind farms are introduced to investigate the SSO. Three methods to measure frequency-domain impedance for wind farms are presented: frequency scans in the static frame and the *dq*-frame, and time-domain data-based identification. Further, s-domain admittance model-based eigenvalue analysis is carried out to demonstrate the effectiveness of stability prediction.

Chapter 5 presents a single-stage multi-port hybrid boost converter (HBC) to supply dc load and ac load simultaneously in grid connected DC-based power system. Detailed modeling of the HBC in the closed-loop control is demonstrated and developed in an EMT testbed in MATLAB/Simscape. The effectiveness and robustness of HBC are examined to regulate the dc and ac output while maintaining the closed-loop stability.

Chapter 6 summarizes the research conclusions of the dissertation and gives suggestions for the future work.

Chapter 2: Characteristics of IBGs

This chapter presents the characteristics of inverter-based generators (IBGs) connected to the point of common coupling (PCC) bus at the transmission or distribution level. The scope of this dissertation is to study power system dynamic studies relevant to grid integration. Special focus will be placed on the type-4 wind turbine generators (WTGs) which interface with power grids through grid-following voltage source converters. This leading to impacts on the power system dynamics mainly rely on the grid-side converter.

2.1 Modeling Assumptions

Modeling each component of IBGs in details will increases complexity and introduces heavy computational burden in simulation. Grid industry usually employs the simplified models accounting for the phenomena being investigated. The study objective of this dissertation is dynamics studies with grid integration. Thus, some modeling assumptions are adopted for efficient computation.

2.1.1 Aggregation Methodologies

A large scale IBG generally consists of tens of hundreds of inverter-based units. It is not practical to represent each generator individually in terms of the system orders and simulation time. It has been reported by several recent studies [49–53], there is no mutual interaction between wind turbines or solar PV units in the case of well-tuned converters. Meanwhile, considering the fact that a wind farm usually includes the same type of WTGs which are operating under very similar conditions. Therefore, a single-machine equivalent is reasonable to represent multiple identical WTGs or solar PV units as long as their static and dynamic settings are similar. This simplification have been used in several studies [54–59] showing that a single-machine equivalent is adequate for analyzing power system dynamics.

2.1.2 Transmission Simplification

Certain system interaction studies, such as sub-synchronous resonance (SSR), are dynamic behaviors more of the transmission than other parts. Thus, the local transmission is ignored. This assumption has been proved in most publication with good approximation in this kind of studies.

The equivalent long-distance transmission is represented with step-up transformers and a transmission line dominated by inductors. IEEE first benchmark model is provided in 1977 [60] for SSRs investigation. It is noted that a simple radial RLC circuit is able to produce both transient and self-excitation problems as severe as any observed in the analysis of the actual system. This simplification is reasonable and supported by several studies [56–59]. Thus, in this research, a RL or RLC circuit is used to represent the transmission line. The high grid reactance is adopted to simulate the long-distance line under weak-grid condition. This method is also used in the [61–63] to analyze the stability issues under weak grid conditions.

2.1.3 Averaging Technique

Electromagnetic transient (EMT) simulation with full details playes an important role in studying the power system dynamics.

The existing EMT dynamic simulation models include two kinds of models: average (non-switching) EMT model and detailed switching EMT model. The difference is the average model replaces the switching model of the voltage source converter (VSC) with an equivalent dynamic average-value model (AVM). Compared to the discrete waveform obtained using pulse width modulation (PWM), the AVM only considers the fundamental part and thus adopts a three-phase controllable voltage source to represent the VSC. The generated ac voltage averages over one cycle of the switching frequency ignoring the harmonics. The averaging technique is proposed to present a continuous nonlinear converter in 1977 [64].

Both average model and detailed model are able to precisely investigate the dynamics relevant to grid integration. But average model has significant simulation efficiency compared to the detailed model because the simulation of the switching events introduces unnecessary computational burden.

2.1.4 Converter Controls

It is reported that the dynamic responses of IBGs are defined by the controller of the grid-side converter (GSC) and the transmission line [65, 66]. It is reasonable to only consider the control features of GSC while ignoring the rest dynamics.

Using the cascaded vector control, the outer d-axis control loop of GSC may assumes dc-link voltage control mode or real power control mode [67]. If the dc-link dynamic is considered, the dc-link voltage control mode regulates the dc-link voltage to correspondingly modulate the real power of the whole system. The real power control mode assumes the dc-link voltage as a constant while directly regulating the real power refer to its control reference value. Large size IBGs' GSCs prefers power control mode [68]. This fact is also confirmed by [15], a study carried out by Siemens where power control mode is assumed for GSC.

There are two q-axis control loops of GSC to regulate the reactive power: one is the reactive power control mode and the other is the PCC voltage control mode [69, 70]. The reactive power control mode modulates the reactive power refer to its control reference value. The PCC voltage control mode regulates the PCC voltage which is associated with the reactive power of the whole system.

2.2 Cascade Vector Control Structure

The scheme of simplified IBG with a grid-following control method is shown in Fig. 2.1. The IBR connect to the power grid through a GSC which injects the active and reactive power to the power grids based on the outer control setpoints. The GSC synchronizes the the point of common connection (PCC) voltage with the grid voltage using a PLL. The overall cascade control structure is shown in Fig. 2.2. It includes the outer control loop and the faster inner current control loop. Both loops' controllers adopt proportional-integral (PI) controllers and are modeled in the converter dq-reference frame, which is a reference frame (denoted by superscript c) that rotates synchronously with the PCC voltage. The GSC output voltages (v_d, v_q) are generated from the current orders i_{1d}^* and i_{1q}^* by the decoupled inner current control loop. The reference current i_{1d}^* is determined by either the real power control or the DC-link voltage control. Meanwhile, i_{1q}^* is generated by either the PCC voltage control or the reactive power control.

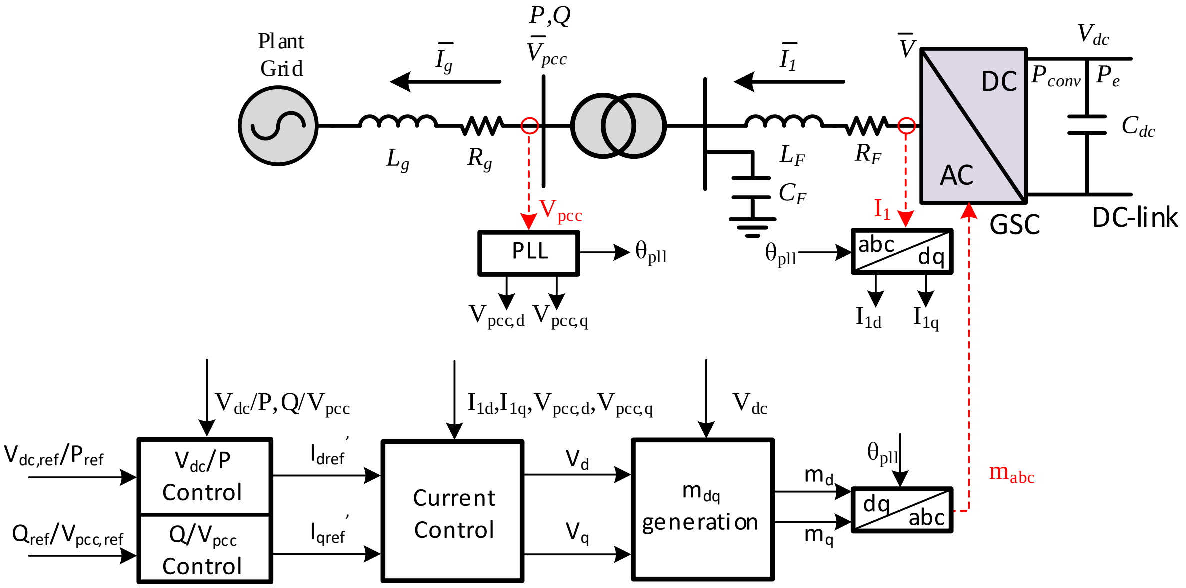

Figure 2.1: The scheme of simplified IBG with a grid-following control method.

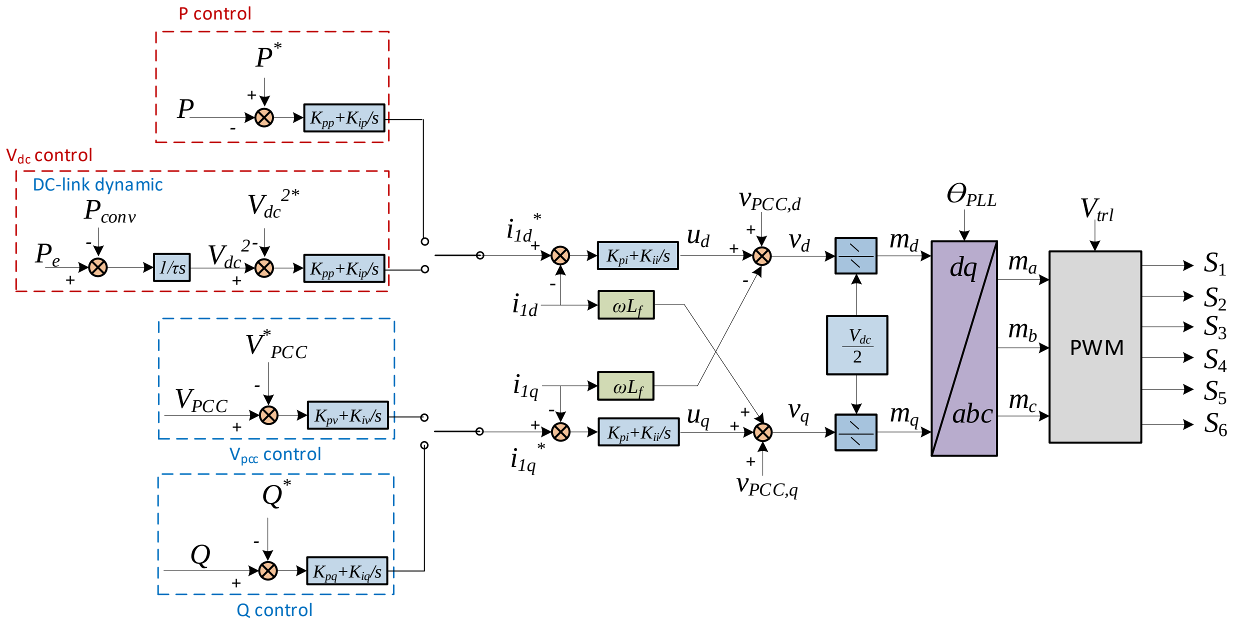

Figure 2.2: Grid-following GSC control loop.

2.2.1 Outer Control Loop

Indicated in [71], the outer DC-link voltage controller is used to generate the reference signal i_d^* to regulate the DC-link voltage, and, thus, balance the power flow in the system. The energy in the capacitor can be expressed as

$$\frac{C_{dc}}{2}\frac{dV_{dc}^2}{dt} = P_e - P_{conv} \tag{2.1}$$

where P_e is the active power before the DC-link capacitor, and P is the active power from the GSC. Per unitizing above equation leads to

$$\underbrace{\frac{C_{dc}V_{base,dc}^2}{2P_{base}}}_{\tau}\frac{dV_{dc}^{\mathrm{pu}2}}{dt} = P_e^{\mathrm{pu}} - P_{conv}^{\mathrm{pu}} \tag{2.2}$$

Using Park transformation, the active and reactive powers flowing into the power grid in the converter dq-reference frame are represented as follows:

$$\begin{cases} P & = v_{\mathrm{pcc},d}^c i_{1d}^c + v_{\mathrm{pcc},q}^c i_{1q}^c \\ Q & = v_{\mathrm{pcc},q}^c i_{1d}^c - v_{\mathrm{pcc},d}^c i_{1q}^c \end{cases} \tag{2.3}$$

where subscripts 'd' and 'q' denote the quantities in d-q reference frame. The decoupled dq-axis control method is implemented, with d-axis aligns with the PCC voltage phasor using PLL, to achieve the independent control ($v_{\mathrm{pcc},d}^c = V_{\mathrm{PCC}}, v_{\mathrm{PCC},q}^c = 0$). The powers can be simplified as $P = V_{\mathrm{PCC}} i_{1d}^c$ and $Q = -V_{\mathrm{PCC}} i_{1q}^c$. It is observed that active power can be controlled by the d-axis current i_{1d}^c. Meanwhile, with this simplification, (2.2) can be rewritten as

$$\tau\frac{dV_{dc}^{\mathrm{pu}2}}{dt} \approx P_e^{\mathrm{pu}} - V_{\mathrm{PCC}} i_{1d}^c \tag{2.4}$$

It is found that the square of DC-link voltage can also be controlled by the d-axis current i_{1d}^c.

Similarly, the PCC voltage control or reactive power control loop using the same criterion as that for DC-link voltage control loop design, the q-axis current i_{1q}^{c} is controlled by either PCC voltage or reactive power.

2.2.2 Inner Control Loop

The dynamic equation of the ac-side can be expressed as follows:

$$L_F \frac{di_{abc}}{dt} = V_{abc} - R_F i_{1,abc} - V_{pcc,abc} \tag{2.5}$$

where V_{abc} is the ac output terminal voltage of the GSC.

Using Park's transformation, (2.5) can be expressed in dq-frame as follows:

$$L_F \frac{di_{1d}}{dt} = L_F \omega(t) i_{1q} + v_d - R_F i_{1d} - v_{pcc,d} \tag{2.6}$$

$$L_F \frac{di_{1q}}{dt} = -L_F \omega(t) i_{1d} + v_q - R_F i_{1q} - v_{pcc,q} \tag{2.7}$$

The current equations in Laplace-domain are written as follows:

$$i_{1d}(s) = \frac{1}{L_F s + R_F} \underbrace{(L_F \omega i_{1q} + v_d - v_{pcc,d})}_{u_d(s)} \tag{2.8}$$

$$i_{1q}(s) = \frac{1}{L_F s + R_F} \underbrace{(-L_F \omega i_{1d} + v_q - v_{pcc,q})}_{u_q(s)} \tag{2.9}$$

where u_d and u_q are the outputs of the PI controllers which are designed to track the current references i_{1d}^{*} and i_{1q}^{*}.

2.2.3 Phase Locked Loop

There are several Phase-locked-loop (PLL) topologies such as Quadrature PLL (Q-PLL), Enhanced PLL (E-PLL), Second-Order Generalized Integrator PLL (SOGI-PLL), and Synchronous Reference Frame PLL (SRF-PLL). In this dissertation, SRF-PLL is employed to align the d axis of dq-frame with the PCC voltage.

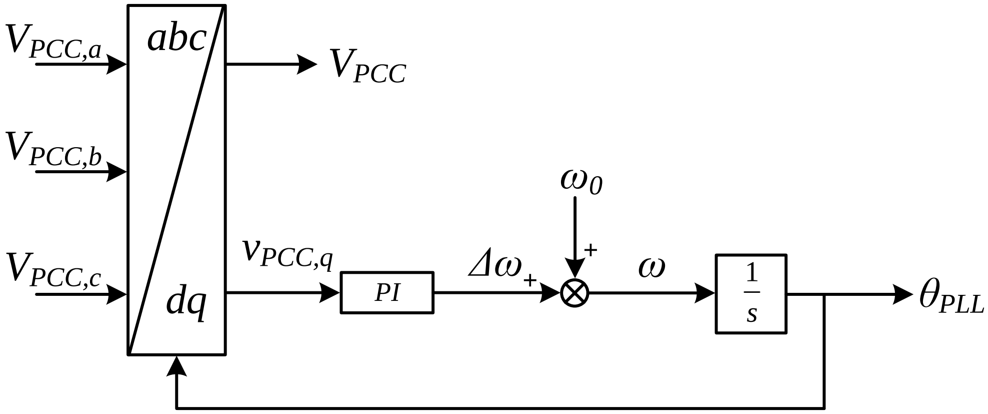

Figure 2.3: Block diagram of the SRF-PLL.

Fig. 2.3 shows the configuration of the PLL. The output angle θ_{PLL}, is produced by a feedback loop which regulates $v_{pcc,q}$ to zero, can be obtained as

$$\begin{cases} \theta_{PLL} & = \theta_0 + \int \omega dt \\ \omega & = \omega_0 + K_p v_{PCC,q} + K_i \int v_{PCC,q} dt \end{cases} \tag{2.10}$$

where θ_0 is the steady-state phase angle of the PCC voltage, ω_0 is the fundamental frequency of the grid, and K_p and K_i are the proportional and integral gains of the PI controller, respectively. This way, the input voltage's space vector is now aligned with the PCC voltage based on θ_{PLL}. That is to say, $v_{pcc,d} = V_{PCC}$ and $v_{pcc,q} = 0$.

Chapter 3: Modeling and Analysis of IBGs in Weak and Series Compensated Networks

3.1 Introduction

This chapter [1] presents the modeling and stability analysis of type-4 wind in series compensated networks with weak grid consideration. Type-4 wind is claimed to be immune from subsynchronous resonances (SSRs) that have been experienced by type-3 wind with radial connection to series compensated lines. Strong grid assumption is normally made in the study systems. But when the grid is weak, the wind farm models for power system dynamic studies, e.g., the WECC model, may result in inaccurate stability analysis. Thus, this chapter will develop a dynamic model suitable for stability analysis of Type-4 wind farms with weak grid interconnection and examine this claim through simplified analytical model building, analysis based on linearized models, and validation against electromagnetic transient (EMT) testbeds with full details.

Indicated in [65], for power system dynamic studies, type-4 WTG system's machine dynamics, and machine-side converter (MSC) dynamics can all be ignored. In other words, the grid dynamics are dominated by the control features of grid-side converter (GSC). Therefore, two analytical models of type-4 wind farm with radial connection to a series compensated line are built in *dq*-frames with GSC control included. The GSC is represented by the average model. That is to say that the GSC switching details are ignored and the converter is treated as a *dq*-frames voltage source. The main difference of the two models is in GSC's control mode, with one model assuming real power control and the other assuming dc-link voltage control. Relying on the analytical models, an efficient approach is demonstrated to obtain frequency-domain impedance models. With initialization procedures to find the equilibrium points, develpoed analytical models can then be linearized at a certain operational condition and small-signal analysis will be carried out using eigenvalue analysis

---

[1] The majority of this chapter was published in IEEE Transactions on Energy Conversion [72], 2019. Permissions are included in Appendix A.

and frequency-domain impedance model-based analysis. Potential stability risk is demonstrated and factors caused stability risk are explored. The small-signal analysis results will be validated against two EMT testbeds with full details in MATLAB/Simscape and PSCAD/EMTDC, respectively.

3.2 EMT testbeds of Type-4 Wind in Series Compensated Networks

The first testbed is a 5 MW type-4 wind grid integration system in PSCAD/EMTDC. This EMT model is a detailed switching model. The schematic diagram of Testbed 1 is shown in Fig. 3.1a. This type-4 wind turbine consists of a permanent magnet synchronous generator (PMSG) to convert mechanical energy to electric energy, and a back-to-back voltage source converters to convert variable frequency ac to 60 Hz ac. This testbed is developed from a demo system in PSCAD/EMTDC where the machine-side converter (MSC) realizes Maximum Power Point Tracking (MPPT) and the GSC assumes dc-link voltage control. The testbed is adjusted to have the GSC realize MPPT control so the outer control of GSC is in real power control mode. The MSC is adjusted to control dc-link voltage. Between the two converters, there is a dc chopper employed to avoid overvoltage on the dc-link capacitor [73].

The second testbed is an average model which is developed based on a demo system in MATLAB/Simscape. Fig. 3.1b shows the 100 MW type-4 wind grid integration testbed with GSC in dc-link voltage control mode. The electricity generated by a synchronous generator is rectified to dc electricity through a diode-bridge rectifier. The dc electricity then passes through a dc/dc boost converter to achieve dc voltage at a different voltage level. MPPT is implemented in the dc/dc boost converter. The parameters of the system are shown in Table 3.1. The values are in pu if not specified.

3.3 Analytical Models of Type-4 in Series Compensated Networks

Two analytical models are built to reflect the two testbeds. In analytical models, wind turbine representation is simplified with only GSC control included. For GSC with dc-link voltage control mode, the dc-link capacitor dynamics is also included. Modeling details of analytical model with weak grid are elaborated in [33]. For this study, the grid dynamics now include LC resonance dynamics.

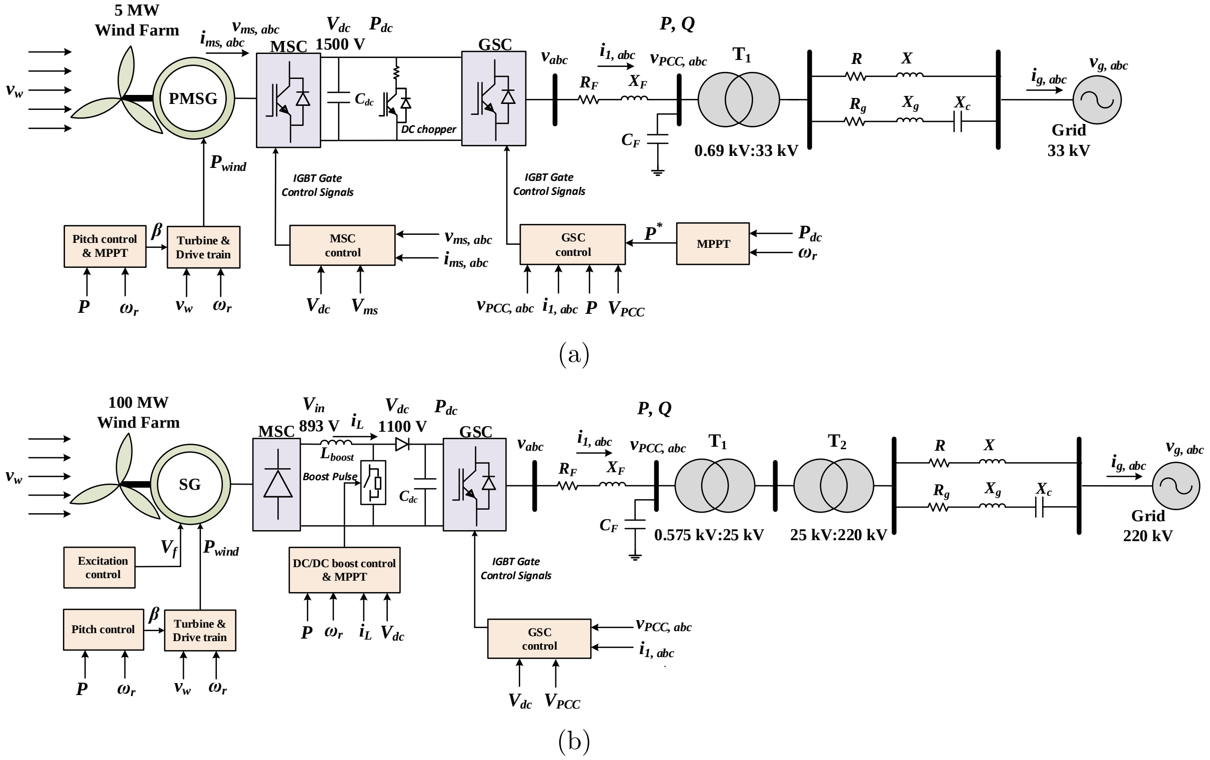

Figure 3.1: EMT testbeds of type-4 wind in series compensated networks.

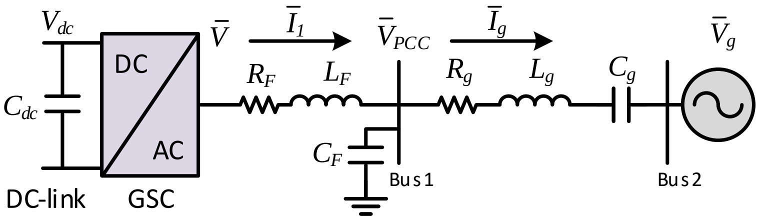

Figure 3.2: A type-4 wind farm with radial connection to a series compensated line.

Table 3.1: Parameters of type-4 wind testbeds and analytical Models.

Description		**Parameters**	**Values**
Testbed 1 PSCAD	base	Sb	5 MW
	Vbase	AC side	690 V, 33 kV
	Vbase	DC side	1500 V
	Power	P	1
	Line	X_g	1
	DC-link	C_{dc}	0.1 F
Testbed 2 MATLAB/ SimPower	base	Sb	100 MW
	Vbase	AC side	575 V, 25 kV, 220 kV
	Vbase	DC side	1100 V
	Power	P	0.9
	Line	X_g	0.7
	dc-link	C_{dc}	0.09 F
	dc/dc inductance	L_{boost}	1.2 mH
Poles		p	2
Rotor speed of generator		ω_r	1
Rated wind speed		v_w	11 m/s
Nominal frequency		f	60 Hz
Converter filter		R_F	0.003
		X_F	0.15
Shunt capacitor susceptance		B_c	0.3
Transformer T_1		R_{T1}	0.0005
		X_{T1}	0.005
Transformer T_2		R_{T2}	0.0005
		X_{T2}	0.005
X over R ratio		X/R	10
Inner current control		(K_{pi}, K_{ii})	0.4758, 3.2655
Power control		(K_{pp}, K_{ip})	0.25, 25
dc-link control		(K_{pp}, K_{ip})	0.25, 25
AC voltage control		(K_{pv}, K_{iv})	0.2, 20
PLL1		$(K_{p,pll1}, K_{i,pll1})$	60, 1400
PLL2 for Model 1, Testbed 1		$(K_{p,pll2}, K_{i,pll2})$	150, 10000

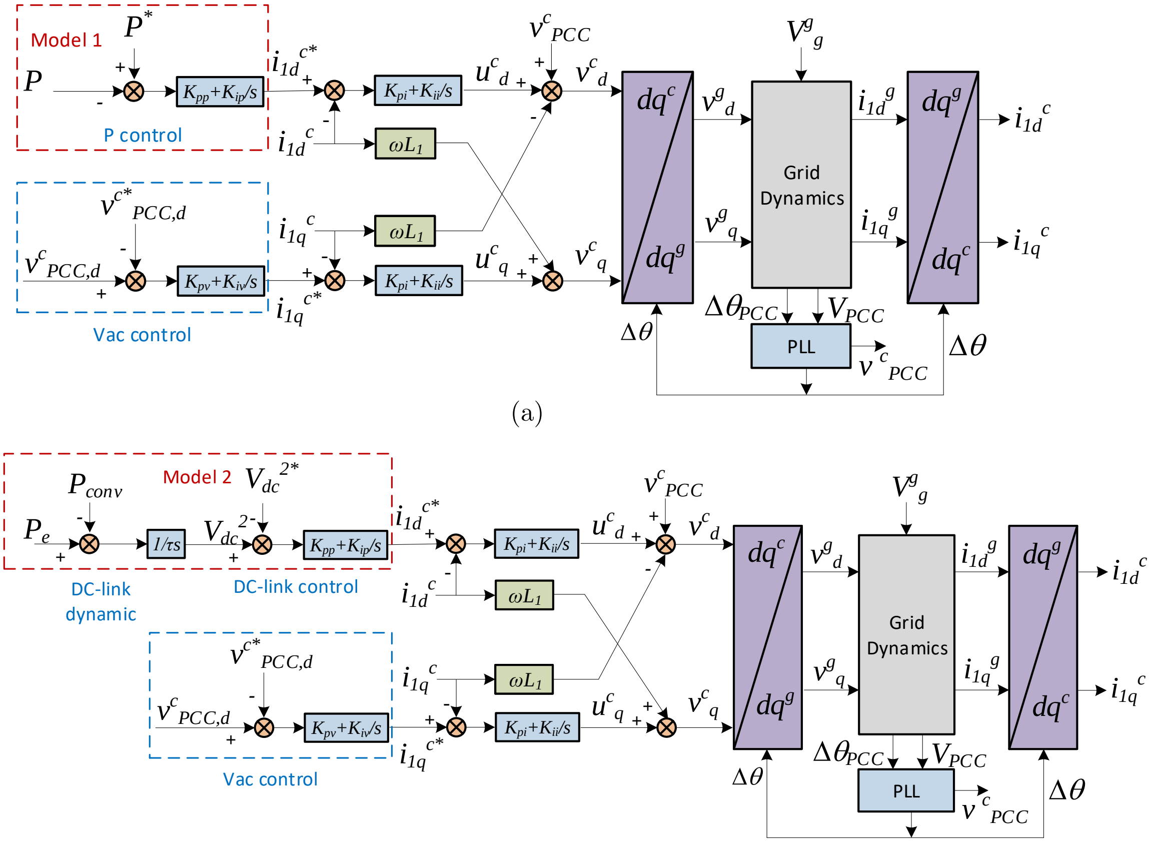

(a)

(b)

Figure 3.3: Analytical Model 1 with GSC in power control mode and analytical Model 2 with GSC in dc-link voltage control mode.

Fig. 3.2 presents the system circuit topology. The analytical models are presented in Fig. 3.3, to represent the study system with the GSC's outer control loops, inner current control loops, phase-locked-loop (PLL), and grid dynamics. The GSC is represented by the average model and is treated as a *dq*-frames voltage source. The outer and inner control loops adopt proportional-integral (PI) controllers and are modeled in the converter *dq*-reference frame, which is denoted by superscript *c*. Considering the PLL is employed to guarantee that the d-axis of *dq* frame aligns with the PCC voltage phasor $\vec{v}_{\mathrm{PCC}}$, it is assumed that $v^{c}_{\mathrm{PCC},d} = V_{\mathrm{PCC}} = V_{\mathrm{PLL}}$, $v^{c}_{\mathrm{PCC},q} = 0$. The grid dynamics are modeled in the grid *dq*-reference frame. Hence, at steady-state, all state variables are constant. With this feature, linear models can be derived using numerical perturbation.

In Model 1, GSC is in power control mode. The power order is assumed to be a known parameter. In Model 2, GSC is in dc-link voltage control mode. The modeling of the outer and inner feedback control loops are elaborated in section 2.2. The PLL, grid dynamics, and the system initialization for the proposed analytical models will be given in the following.

3.3.1 Phase Locked Loop

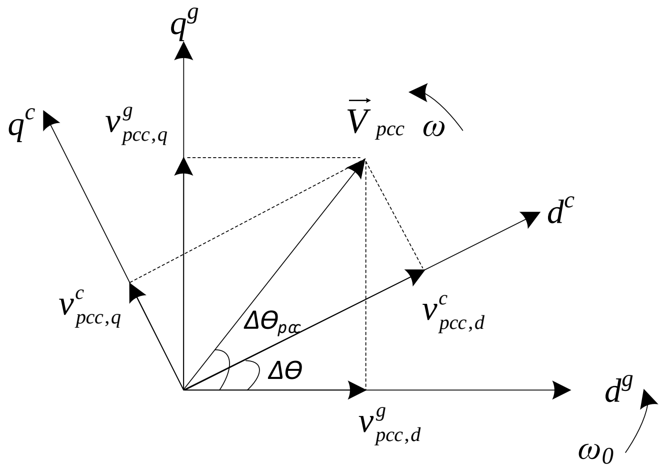

Figure 3.4: Spatial relationships between grid and converter *dq* reference frame.

As shown in Fig. 3.3, *dq*-frames in the analytical model include the converter *dq*-reference frame (denoted by superscript '*c*') and grid *dq*-reference frame (denoted by superscript '*g*'). The most critical step of system modeling is the transformation from converter *dq*-reference frame to the grid *dq*-reference frame. Fig. 3.4 shows the space vector diagram of PCC voltage and the spatial relationships between both reference frames. The angular frequency of the PCC voltage is ω as distinguished from the grid nominal frequency ω_0. Considering the PLL accurately tracks the angle of the PCC voltage (θ_{PCC}) to synchronize the converter voltage with the grid voltage in steady state, thus at steady state, $\omega = \omega_0$ and the phase displacement θ_{PCC} between PCC voltage space vector and grid reference d-axis can be assumed to be the same as the angular difference between both dq-frames. That is to say, $\theta_{\text{PCC}} = \theta$.

The relationship between voltage space vectors in the converter dq-reference frame and grid dq-reference frame is shown as follows:

$$\left(v^g_{pcc,d} + jv^g_{pcc,q}\right) e^{j\omega_0 t} = \vec{v}_{pcc,abc} = \left(v^c_{pcc,d} + jv^c_{pcc,q}\right) e^{j\theta} \tag{3.1}$$

Reorganizing above equation, the following equation of both dq-frames transformation can be obtained:

$$v^g_{pcc,d} + jv^g_{pcc,q} = \left(v^c_{pcc,d} + jv^c_{pcc,q}\right) e^{j\Delta\theta} \tag{3.2}$$

where $\Delta\theta = \theta - \omega_0 t$.

A simple second-order PLL is assumed. Structure of the PLL is shown in Fig. 3.5. The PCC voltage magnitude V_{PCC} and $\Delta\theta_{\text{PCC}}$ can thus be obtained by

$$\begin{cases} V_{\text{PCC}} & = \sqrt{v^{g^2}_{\text{PCC},d} + v^{g^2}_{\text{PCC},q}} \\ \Delta\theta_{\text{PCC}} & = \tan^{-1}\left(\frac{v^g_{\text{PCC},q}}{v^g_{\text{PCC},d}}\right) \end{cases} \tag{3.3}$$

V_{PCC} and $\Delta\theta_{\text{PCC}}$ are fed to the PLL to generate V_{PLL} and $\Delta\theta$. The dq components of $\vec{v}^c_{\text{PCC}}$ in the converter dq-reference frame are deduced as follows:

$$\begin{cases} v^c_{\text{PCC},d} & = V_{\text{PCC}} \cos\left(\Delta\theta_{\text{PCC}} - \Delta\theta\right) \\ v^c_{\text{PCC},q} & = V_{\text{PCC}} \sin\left(\Delta\theta_{\text{PCC}} - \Delta\theta\right) \end{cases} \tag{3.4}$$

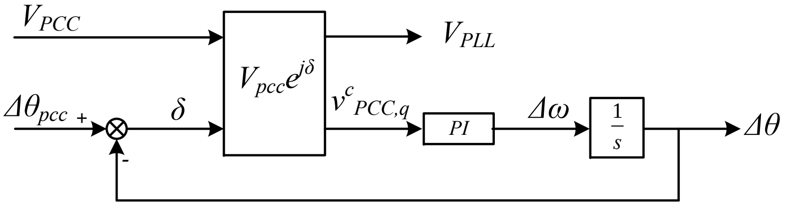

Figure 3.5: Block diagram of a simple second-order PLL.

It is assumed $\Delta\theta = \Delta\theta_{\mathrm{PCC}}$ in steady state, we have $v^c_{\mathrm{PCC},d} = V_{\mathrm{PCC}} = V_{\mathrm{PLL}}$ and $v^c_{\mathrm{PCC},q} = 0$. $v^c_{\mathrm{PCC},q}$ is the input of the PI controller to generate the frequency deviation $\Delta\omega$. The PLL output angle $\Delta\theta$ is then obtained by integrating $\Delta\omega$.

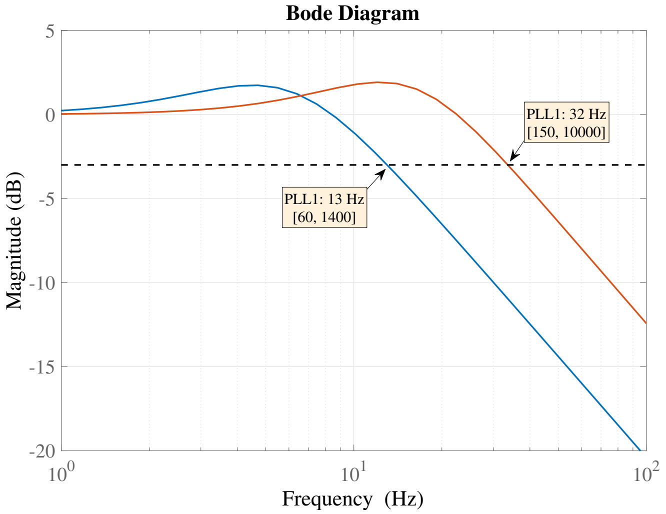

Figure 3.6: PLL 1 and PLL 2 with different bandwidth.

Effect of PLL parameters on stability is examined. Two sets of parameters are considered. PLL 1 has proportional and integral gains as (60, 1400). PLL 2 has proportional and integral gains as (150, 10000). The two PLLs have bandwidths of 13 Hz and 32 Hz respectively. Their close-loop transfer functions from the input angle to the output angle are plotted and shown in Fig. 3.6.

3.3.2 Grid Dynamics

The grid dynamics are modeled in the grid dq-reference frame, which rotates at the nominal speed ω_0.

The grid dynamics block has the converter voltage and grid voltage as input or known parameters. Both the converter voltage and the grid voltage are assumed to be three-phase balanced. At stead-state, their dq-frame variables all assume constant values.

The state variables of the grid dynamics block include the series capacitor voltage, the shunt capacitor voltage, the grid current, and the converter output current, all in dq-frame. Total, there are eight state variables.

The grid dynamics in the grid dq-frame can be derived from abc-frame space vector based differential equations. The dq-frame differential equations are expressed as follows:

$$\begin{cases} \frac{di^g_{1d}}{dt} &= \frac{1}{L_F}(v^g_d - v^g_{PCC,d} - R_F i^g_{1d} + L_F\omega_0 i^g_{1q}) \\ \frac{di^g_{1q}}{dt} &= \frac{1}{L_F}(v^g_q - v^g_{PCC,q} - R_F i^g_{1q} - L_F\omega_0 i^g_{1d}) \\ \frac{di^g_{g,d}}{dt} &= \frac{1}{L_g}(v^g_{PCC,d} - v^g_{c,d} - v^g_{g,d} - R_g i^g_{g,d} + L_g\omega_0 i^g_{g,q}) \\ \frac{di^g_{g,q}}{dt} &= \frac{1}{L_g}(v^g_{PCC,q} - v^g_{c,q} - v^g_{g,q} - R_g i^g_{g,q} - L_g\omega_0 i^g_{g,d}) \\ \frac{dv^g_{PCC,d}}{dt} &= \frac{1}{C_F}(i^g_{1d} - i^g_{g,d} + C_F\omega_0 v^g_{PCC,q}) \\ \frac{dv^g_{PCC,q}}{dt} &= \frac{1}{C_F}(i^g_{1q} - i^g_{g,q} - C_F\omega_0 v^g_{PCC,d}) \\ \frac{dv^g_{c,d}}{dt} &= \frac{1}{C_g}(i^g_{g,d} + C_g\omega_0 v^g_{c,q}) \\ \frac{dv^g_{c,q}}{dt} &= \frac{1}{C_g}(i^g_{g,q} - C_g\omega_0 v^g_{c,d}) \end{cases}$$

where i^g_{1d}, i^g_{1q}, $i^g_{g,d}$, $i^g_{g,q}$, v^g_d, v^g_q, $v^g_{PCC,d}$, $v^g_{PCC,q}$, $v^g_{c,d}$, $v^g_{c,q}$ and $v^g_{g,d}$, $v^g_{g,q}$ are the d and q components of the converter current, grid current, converter voltage, PCC voltage, capacitor voltage, and grid voltage.

3.3.3 System Initialization

To carry out the eigenvalue analysis, an initialization is essential to calculate the steady-state initial values of the state variables [74]. Newton Raphson (NR) method is used here to determine the certain operation condition.

In this research, the analytical model is an fourteen-order dynamical system. fourteen state variables, that includes eight state variables related to grid dynamics (i^g_{1d}, i^g_{1q}, $i^g_{g,d}$, $i^g_{g,q}$, $v^g_{PCC,d}$,

$v^g_{PCC,q}$, and $v^g_{c,d}$, $v^g_{c,q}$), two state variables related to PLL ($\Delta\omega, \Delta\theta$), two state variables related to outer control loops (i^c_d, i^c_q), and two state variables related to inner current control loops (u_d, u_q), should be initialized.

According to Fig. 3.2, the nodal admittance matrix Y is formed as follows:

$$Y = \begin{bmatrix} Y_{11} & Y_{12} \\ Y_{21} & Y_{22} \end{bmatrix} \tag{3.5}$$

where

$$Y_{ij} = G_{ij} + jB_{ij} = \begin{cases} Z_g^{-1} & i = j \\ -Z_g^{-1} & i \neq j \end{cases} \tag{3.6}$$

To regulate the q-axis current independently, either reactive power control mode or the PCC voltage control mode is adopted in practical modeling approach. The initialization process for both feedback controls will be described in the following.

3.3.3.1 Reactive Power Control

If the analytical model adopts the reactive power control mode, the voltage space vector of bus 2 (grid) are fixed at $\bar{V}_2 = 1\angle 0°$. Meanwhile initial guesses of the voltage magnitude and angle of bus 1 (PCC bus) are chose as $V_1^{(0)} = 1$ and $\theta_1^{(0)} = 0°$ respectively which are updated with each iteration k.

The net real and reactive injection power at the PCC bus, are written as equations (3.7) and (3.8) [75].

$$P^{c(k)} = \sum_{j=1}^{2} V_1 V_j \left[G_{1j}\cos(\theta_1 - \theta_j) + B_{ij}\sin(\theta_1 - \theta_j)\right] \tag{3.7}$$

$$Q^{c(k)} = \sum_{j=1}^{2} V_1 V_j \left[G_{1j}\sin(\theta_1 - \theta_j) - B_{1j}\cos(\theta_1 - \theta_j)\right] \tag{3.8}$$

where V_j is the voltage magnitude of bus j and θ_j is the voltage angle of bus j. The calculation of the powers are then compared with the scheduled values to obtain the mismatch:

$$\Delta^{(k)} = \begin{bmatrix} P^{c(k)} - P^{sch} & Q^{c(k)} - Q^{sch} \end{bmatrix}^T \tag{3.9}$$

where P^{sch} and Q^{sch} are the scheduled real and reactive power at bus 1, respectively. The superscript T means the transpose of the matrix. The iterative scheme of NR method can be represented as

$$x^{(k+1)} = x^{(k)} - J^{-1} \cdot \Delta^{(k)} \tag{3.10}$$

where

$$x = \begin{bmatrix} V_1 & \theta_1 \end{bmatrix}^T \tag{3.11}$$

and J is the Jacobian matrix of partial derivatives of (3.7) and (3.8) with respect to x, as shown in (3.12). The elements of Jacobian matrix is required to calculate in each iteration.

$$J = \begin{bmatrix} \frac{\partial P^c}{\partial V_1} & \frac{\partial P^c}{\partial \theta_1} \\ \frac{\partial Q^c}{\partial V_1} & \frac{\partial Q^c}{\partial \theta_1} \end{bmatrix} \tag{3.12}$$

Repeat (3.10) until the tolerance of the powers mismatch in (3.9) is less than 0.00001. After tolerance achieves convergence, the voltage phasors $\bar{V}_{pcc} = V_1\angle\theta_1$ can be obtained. Then, the current phasor of transmission line, shunt filter, and RL filter can be found, respectively.

$$\bar{I}_g = \frac{\bar{V}_{pcc} - \bar{V}_g}{Z_g} \tag{3.13}$$

$$\bar{I}_F = \bar{V}_{pcc} \times j\omega C_F \tag{3.14}$$

$$\bar{I}_1 = \bar{I}_g + \bar{I}_F \tag{3.15}$$

Hence the converter output voltage and voltage across the series capacitor can be calculated as

$$\bar{V} = \bar{V}_{pcc} + (R_F + j\omega_0 L_F)\bar{I}_1 \tag{3.16}$$

$$\bar{V}_C = \bar{I}_g \times (-jX_{C_g}) \tag{3.17}$$

As shown in Fig. 3.5, the initial value of $\Delta\theta$ is assigned a value from the angle of PCC voltage θ_1. The initial value of $\Delta\omega$ is considered as zero. Applying the *abc* to grid *dq*-reference frame transformation, eight voltage components ($v_d^g, v_q^g, v_{\mathrm{PCC},d}^g, v_{\mathrm{PCC},q}^g$, $v_{c,d}^g$, $v_{c,q}^g$ and $v_{g,d}^g$, $v_{g,q}^g$) and four current components (i_{1d}^g, i_{1q}^g and $i_{g,d}^g$, $i_{g,q}^g$) are obtained. With the initial value of $\Delta\theta$, the grid to converter frame transformation can be performed using the equation in (3.2) to find $v_d^c, v_q^c, v_{\mathrm{PCC},d}^c, v_{\mathrm{PCC},q}^c$, $v_{c,d}^c$, $v_{c,q}^c$, $v_{g,d}^c$, $v_{g,q}^c$, i_{1d}^c, i_{1q}^c and $i_{g,d}^c$, $i_{g,q}^c$. Considering $v_{\mathrm{PCC},d}^c = V_{\mathrm{PLL}}$ and $v_{\mathrm{PCC},q}^c = 0$ at steady state, the initial values of u_d and u_q (outputs of the current loop PI controllers) can be computed as follows:

$$\begin{cases} u_d &= L\omega i_q^c + v_{1d}^c - V_{\mathrm{PLL}} \\ u_q &= -L\omega i_d^c + v_{1q}^c \end{cases} \tag{3.18}$$

All initial parameters are obtained.

3.3.3.2 PCC Voltage Control

If the analytical model adopts the PCC voltage control mode, the voltage space vector of bus 2 and voltage magnitude of bus 1 are given as $\bar{V}_2 = 1\angle 0°$ and $V_1 = 1$ respectively. The voltage angle θ_1 of bus 1 is easily calculated by using the real power equation in (3.7). The current space vector are then computed using (3.13), (3.14), and (3.15). The other initial parameters are obtained in the same way as that of the section 3.3.3.1.

After the operation conditions are identified via initialization, the system stability with varying series compensation level will be investigated in the following sections.

3.4 Model 1 Analysis and Validation

The analytical model (Model 1) with GSC in active power control model is shown in Fig. 3.3a. The system is assumed to operate and send out 1 pu wind power to grid ($P = 1$) and the

PCC voltage is at nominal level ($V_{\text{PCC}} = 1$ pu). The grid strength without series compensation is assumed to be weak ($X_g = 1$ pu). The analytical model is linearized under various operation conditions to obtain linear models and small-signal analysis are followed. Validation is carried out using the PSCAD/EMTDC testbed with full dynamics.

3.4.1 Eigenvalues and Participation Factor Analysis

The series compensation (sc) level varies from 10% to 75% with a step size of 2.5%. The eigenvalues are plotted and presented in Fig. 3.7. Figs. 3.7a and 3.7b demonstrate the effect of PLL 1 and PLL 2 on system stability, respectively. Fig. 3.7c and Fig. 3.7d are the zoom in plots focusing on the subsynchronous range.

Three modes of less than 100 Hz frequencies are identified to be influenced significantly by series compensation.

It is found that when PLL has a low bandwith, the dominant mode is a 3 Hz mode. With series compensation increasing, this mode moves to the left-half-plane (LHP) and the system becomes more stable. On the other hand, when PLL has a higher bandwith, the dominant mode is a 15 Hz mode. With series compensation increasing, this mode moves to the right-half-plane (RHP) and the system becomes less stable. If series compensation is at 27.5% or more, the system loses stability.

The eigenvalues at two marginal sc conditions are presented in Table 3.2. There are fourteen eigenvalues in Model 1. Participation factors (PFs) are computed for each eigenvalue to identify the most influential states. The info has been listed in Table 3.3. Unstable modes are highlighted in bold fonts. The oscillatory eigenvalues $\lambda{=}\alpha+j\beta$ under marginal condition are used to determine oscillatory frequency as well as damping ratio. The oscillatory frequency is defined as $f{=}\beta/2\pi$ and damping ratio $\zeta{=}{-}\alpha/\sqrt{\alpha^2+\beta^2}$. It can be seen that there are two modes $\lambda_{1,2}$, $\lambda_{4,5}$ above 100 Hz located in the left half-plane (LHP) far from the imaginary axis. PF analysis indicates that the two modes are related to shunt capacitor and transmission line inductance.

The PFs are computed for the three modes under 100 Hz: mode $\lambda_{6,7}$ in the range of $60 \sim 65$ Hz, mode $\lambda_{8,9}$ in the range of $8 \sim 20$ Hz, and a mode $\lambda_{11,12}$ of about $3 \sim 5$ Hz, are listed in Table 3.3.

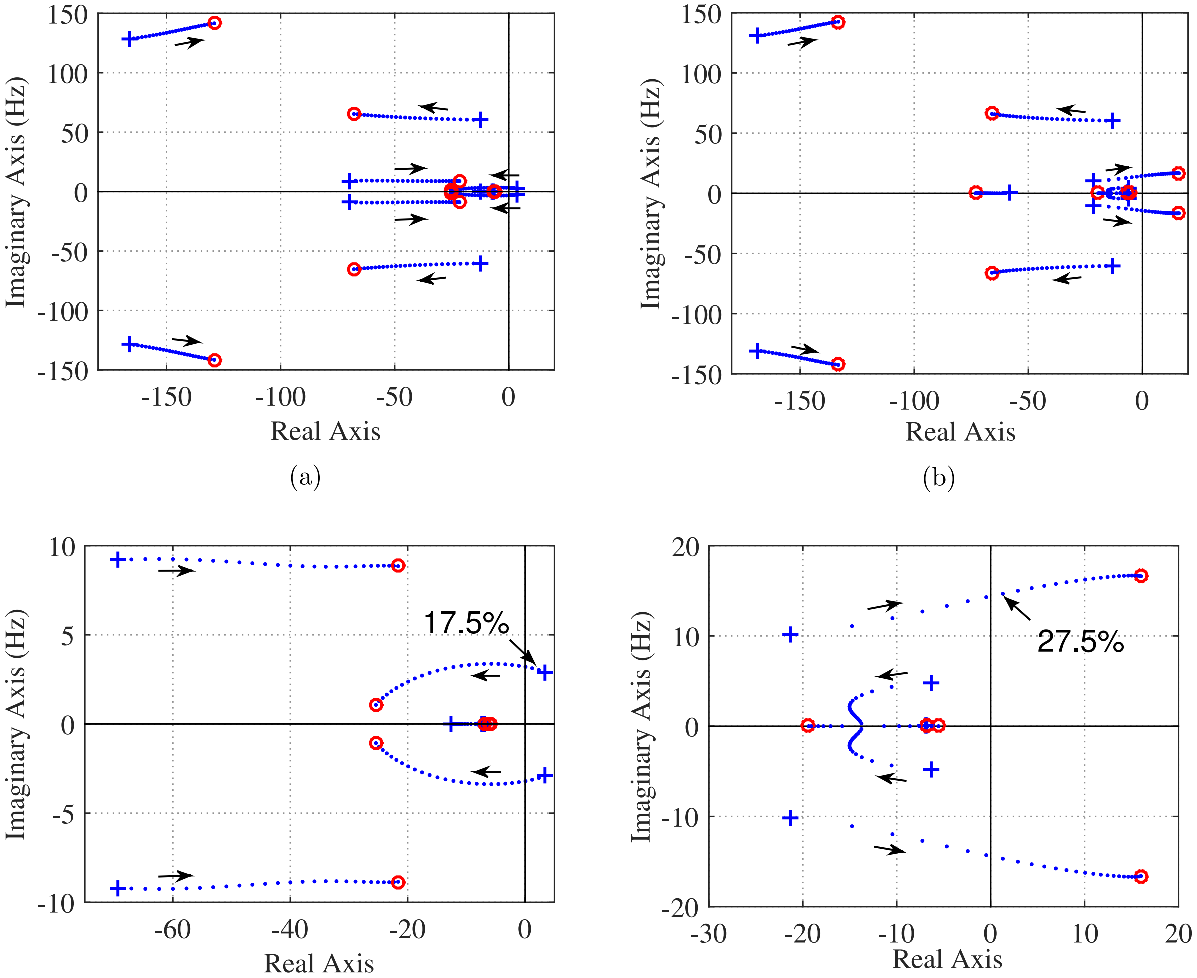

(a) (b)

(c) (d)

Figure 3.7: Eigenvalues loci for Model 1 where GSC is in power control mode with PLL 1 and PLL 2.

Table 3.2: Modes description for the power control under marginal conditions.

	Mode	**Eigenvalue**	**Damping ratio**	**Freq. (Hz)**	**Most relevant states**
PLL 1 (sc=17.5%)	$\lambda_{1,2}$	$-532.6 \pm 1856.0i$	0.276	295.4	C_F, L_g
	λ_3	-1260.7	-	-	-
	$\lambda_{4,5}$	$-160.8 \pm 816.2i$	0.193	129.9	C_F, L_g
	$\lambda_{6,7}$	$-21.2 \pm 381.3i$	0.056	60.7	C_g
	$\lambda_{8,9}$	$-62.3 \pm 58.1i$	0.731	9.3	PLL, Outer loop PI, L_g
	λ_{10}	-12.6	-	-	-
	$\boldsymbol{\lambda_{11,12}}$	$\mathbf{0.1 \pm 20.1}\boldsymbol{i}$	**0.005**	**3.2**	**PLL, Outer loop PI**
	λ_{13}	-6.9	-	-	-
	λ_{14}	-7.3	-	-	-
PLL 2 (sc=27.5%)	$\lambda_{1,2}$	$-592.2 \pm 1866.7i$	0.302	297.1	C_F, L_g
	λ_3	-1259	-	-	-
	$\lambda_{4,5}$	$-157.5 \pm 842.1i$	0.184	134.0	C_F, L_g
	$\lambda_{6,7}$	$-32.5 \pm 385.0i$	0.084	61.3	C_g
	$\boldsymbol{\lambda_{8,9}}$	$\mathbf{1.3 \pm 92.2}\boldsymbol{i}$	**0.014**	**14.7**	**PLL**, $\boldsymbol{L}_{\Gamma}30823$
	λ_{10}	-66.5	-	-	-
	$\lambda_{11,12}$	$-15 \pm 14.9i$	0.709	2.4	Outer loop PI
	λ_{13}	-6.9	-	-	-
	λ_{14}	-6.9	-	-	-

Table 3.3: PFs of modes $\lambda_{6,7}$, $\lambda_{8,9}$ and $\lambda_{10,11}$ in Model 1.

Description	**State Variable**	**Power control**					
		PLL1(sc=17.5%)			PLL2(sc=27.5%)		
		$\lambda_{6,7}$	$\lambda_{8,9}$	$\boldsymbol{\lambda_{11,12}}$	$\lambda_{6,7}$	$\boldsymbol{\lambda_{8,9}}$	$\lambda_{11,12}$
Grid	$i^g_{1,d}$	0.0090	0.0738	0.0012	0.0168	0.0210	0.0083
	$i^g_{1,q}$	0.0082	0.0654	0.0120	0.0107	0.0563	0.0200
	$i^g_{g,d}$	0.0172	**0.4029**	0.0338	0.0233	**0.2042**	0.0588
	$i^g_{g,q}$	0.0060	**0.2577**	0.0289	0.0180	**0.2630**	0.0123
	$v^g_{PCC,d}$	0.0270	0.0492	0.0046	0.0615	0.0436	0.0014
	$v^g_{PCC,q}$	0.0544	0.0775	0.0046	0.0662	0.0373	0.0080
	$v^g_{c,d}$	**0.4642**	0.0496	0.0050	**0.4209**	0.0869	0.0048
	$v^g_{c,q}$	**0.4400**	0.0741	0.0066	**0.4163**	0.0698	0.0173
PLL	$\Delta\theta$	0.0011	**0.3879**	**0.3823**	0.0032	**0.6262**	0.1143
	$\Delta\omega$	0.0001	**0.1293**	**0.2891**	0.0006	**0.3644**	0.1417
Outer-loop	i^c_{1d}	0.0114	**0.5198**	**0.3279**	0.0178	0.1600	**0.6892**
	i^c_{1q}	0.0013	0.089	**0.4367**	0.0014	0.1045	**0.5567**
Inner-loop	u_d	0.0002	0.0023	0.0020	0.0004	0.0012	0.0040
	u_q	0.0001	0.0259	0.0718	0.0001	0.0280	0.0348

Table 3.3 indicates that $\lambda_{6,7}$ and $\lambda_{8,9}$ are related to the series RLC circuit dynamics. The $60 \sim 65$ Hz mode $\lambda_{6,7}$ moves to the LHP with an increasing series compensation level, while the $8 \sim 20$ Hz mode $\lambda_{8,9}$ moves to the RHP.

In the subsynchronous frequency range, the two oscillation modes $\lambda_{11,12}$ and $\lambda_{8,9}$ are affected significantly by the compensation level and PLL. The lower frequency mode $\lambda_{11,12}$ tends to move to left, while the higher frequency mode $\lambda_{8,9}$ tends to move to right. For the slower PLL with a lower bandwidth (PLL 1), the low-frequency mode at 3 Hz is the dominant mode and this mode moves to LHP with an increasing sc. Hence, increasing sc poses no risk of stability.

For the faster PLL with a higher bandwidth (PLL 2), the $8 \sim 20$ Hz frequency mode poses potential stability issues. When sc increases, this mode moves towards RHP. Higher PLL bandwidth makes this mode move further to the RHP.

Time-domain simulation results using Model 1 are presented in Fig. 3.8. The system initially operates with parallel transmission lines (one RL circuit and one RLC circuit). 27.5 % compensation level is assued. At $t = 1$ s, the RL circuit trips. For PLL 1 as shown in Fig. 3.8a, the system is stable. For PLL 2 as shwon in Fig. 3.8b, the system is unstable. The results corroborate with the eigenvalue analysis.

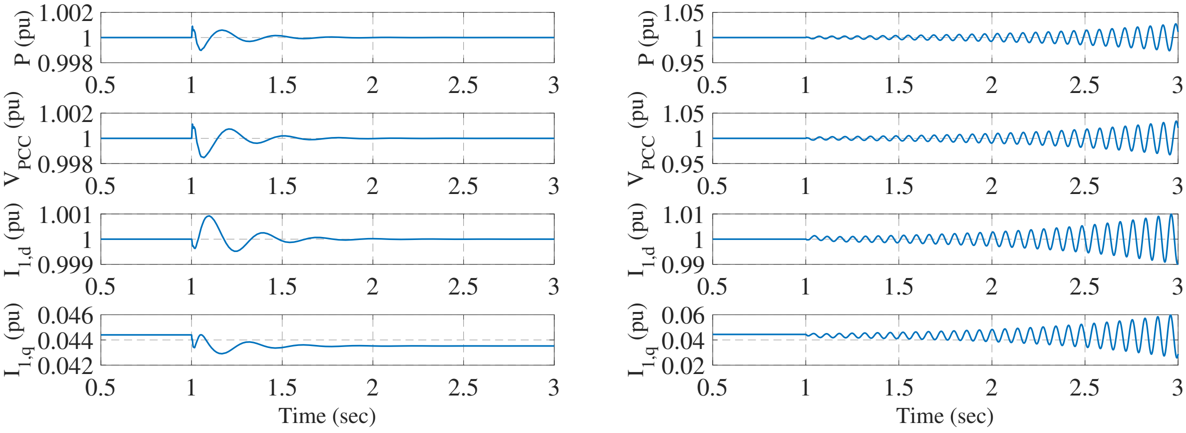

(a) (b)

Figure 3.8: Model 1 dynamic response following an event of a line trip at 1 sec.

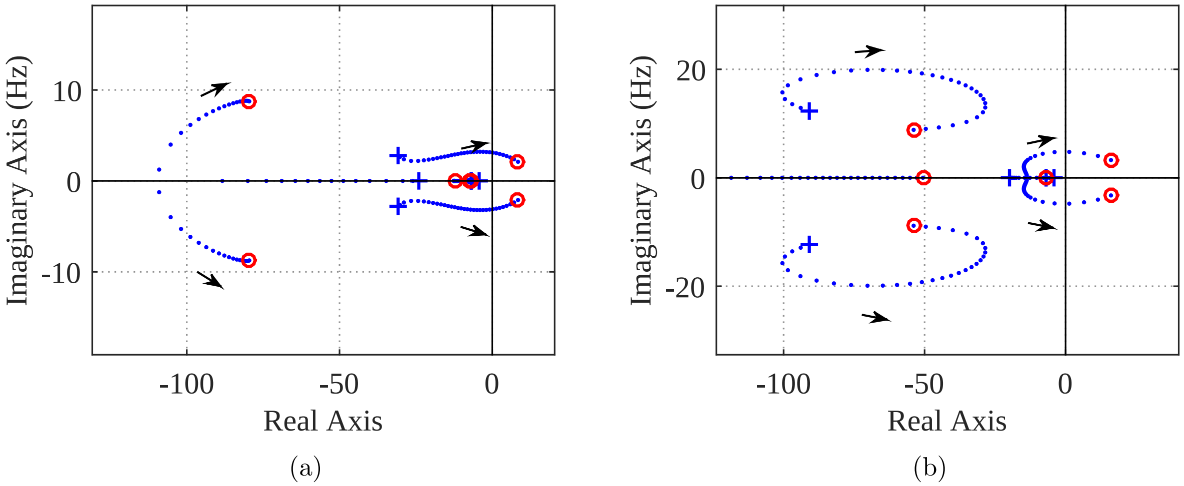

Figure 3.9: Model 1 eigenvalue loci with reduced grid strength for non-compensated transmission line.

3.4.2 Weak Grid Modes in Non-compensated Grid

As a comparison, we present eigenvalue loci in Fig. 3.9 when there is no series compensation. Fig. 3.9a is plotted with PLL 1, meanwhile Fig. 3.9b with PLL 2. X_g is varying from 0.2 pu to 1 pu with a step size of 2.5% to reflect a reducing grid strength. It can be seen the two modes in the frequency range of $2 \sim 20$ Hz move to right with the grid strength reducing. These two modes can be classified as modes related to weak grids. Increasing compensation level is similar as strengthening the grid. Thus, it is reasonable that the low frequency mode of 2-5 Hz moves to the left for an increasing compensation level. On the other hand, due to the interaction of the RLC mode at about 60 Hz, the mode in range of $8 \sim 20$ Hz will move to the right for an increasing compensation level.

3.4.3 EMT Testbed Validation

Finally, EMT testbed validation is given. In Testbed 1 shown in Fig. 3.1a, a type-4 based wind farm is connected to the power grid through two parallel power lines (one non-compensated line and one series compensated line). The non-compensated line is tripped due to a fault. Subsequently, the wind farm become radially connected to the series compensated line.

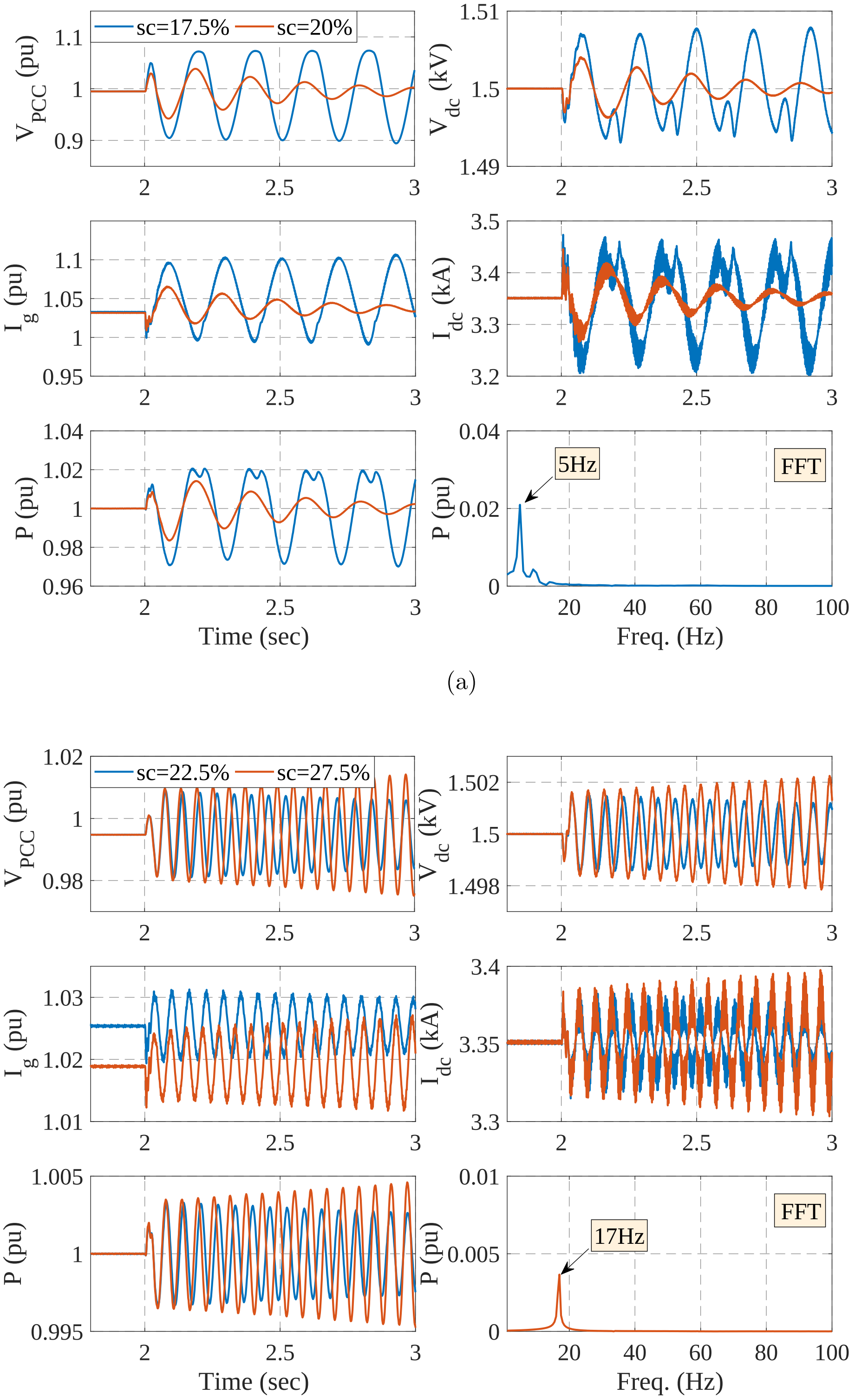

(a)

(b)

Figure 3.10: Dynamic performances of two different compensation levels under P control in PSCAD.

The dynamics of the PCC voltage, transmission line current, real power export from the wind, dc-link voltage, dc side current and Fast Fourier transform (FFT) of wind power export P are shown in Fig. 3.10. PLL 1 and PLL 2 are employed in Fig. 3.10a and Fig. 3.10b, respectively. At $t = 2$ s, the RL circuit is tripped. The system suffers a 5 Hz oscillations if PLL 1 is applied. Increasing the compensation level leads to enhanced stability. On the other hand, the system will suffer 17 Hz oscillations with PLL 2 in place. Moreover, these oscillations will be more severe if the series compensation increases.

The performance aligns with the analytical results presented in Fig. 3.7. If PLL 1 is applied, with the increasing compensation level, the low frequency mode will move to the LHP and the system is more stable. If PLL 2 is applied, the 8 $\sim$ 20 Hz mode becomes the dominant mode. Increasing series compensation level may cause instability.

3.5 Model 2 Analysis and Validation

In Model 2, GSC adopts dc-link voltage control mode, as shown in Fig. 3.3b. The system is assumed to operate at $V_{dc} = 1$ pu, $V_{PCC} = 1$ pu and $X_g = 0.7$ pu. Testbed 2 in MATLAB/Simscape will be used for validation. The system parameters are given in the Table 3.1.

3.5.1 Eigenvalues and Participation Factor Analysis

Fig. 3.11 presents the eigenvalue loci with the series compensation level (sc) varying from 10% to 75% with a step size of 2.5%. Figs. 3.11c and 3.11d are the zoom-in plots of Figs. 3.11a (adopts PLL 1) and 3.11b (adopts PLL 2) for subsynchronous range modes. There are fifteen states and fifteen eigenvalues in Model 2. They are listed in Table 3.4 along with the influential states. Further, Table 3.5 presents participation factors for the three modes with frequency below 100 Hz.

The eigenvalue loci in Fig. 3.11 and Table 3.4 identified two high-frequency mode above 100 Hz ($\lambda_{1,2}$ and $\lambda_{4,5}$), and three oscillation modes below 100 Hz ($\lambda_{6,7}$, $\lambda_{8,9}$, and $\lambda_{11,12}$) which are significantly influenced by the varying compensation level.

The high-frequency modes above 100 Hz are associated with the shunt capacitor and grid inductor dynamics. Mode $\lambda_{6,7}$ with a frequency range 50 $\sim$ 100 Hz is associated with the series capacitor. It moves to the LHP with increasing sc level. The 8 $\sim$ 20 Hz mode $\lambda_{8,9}$ is related to grid current and PLL. It moves towards the RHP with increasing series compensation level. The

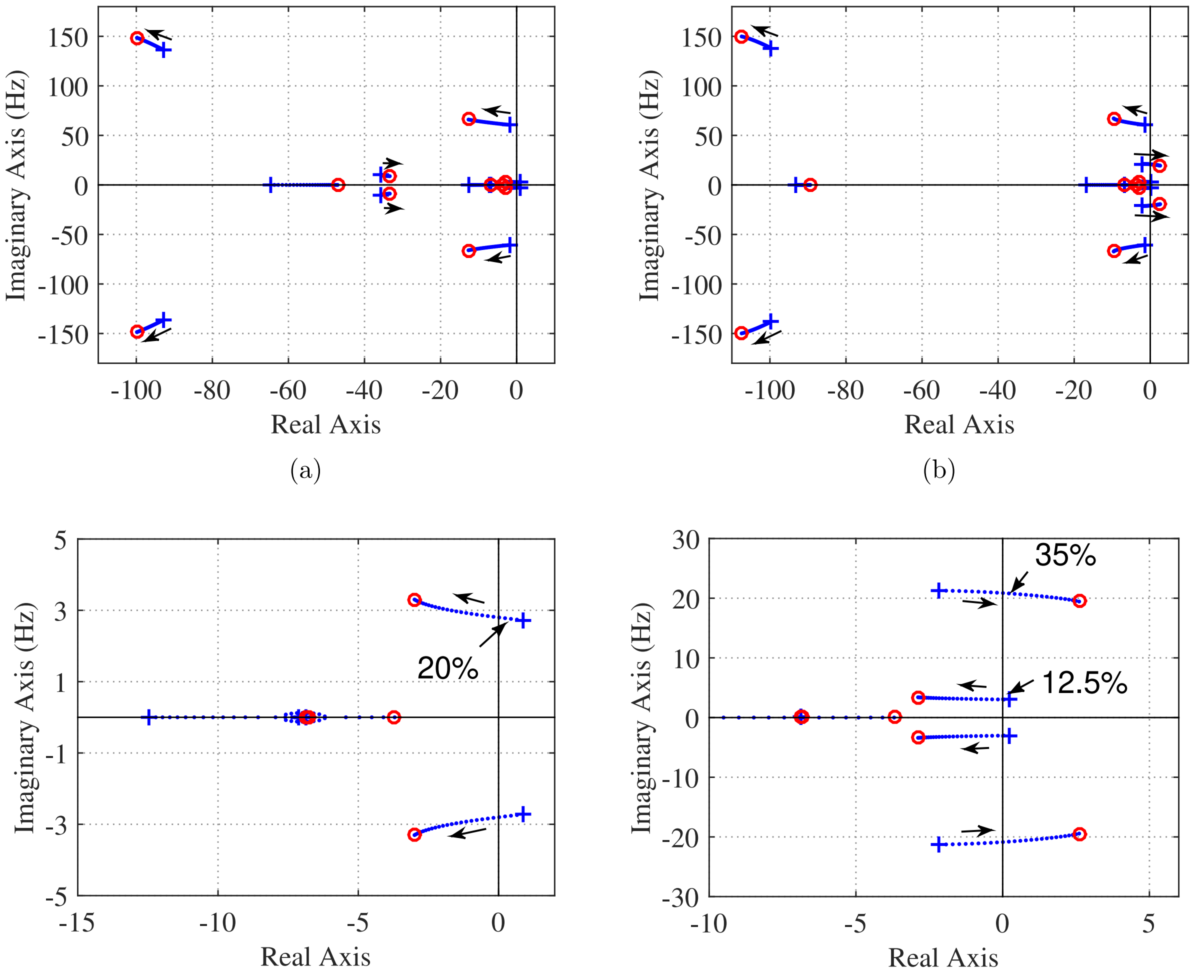

(a)

(b)

(c)

(d)

Figure 3.11: Eigenvalues loci for Model 2 where GSC is in V_{dc} control mode.

Table 3.4: Modes description for the V_{dc} control under marginal conditions.

	Mode	Eigenvalue	Damping ratio	Freq. (Hz)	Most relevant states
PLL 1 (sc=20%)	$\lambda_{1,2}$	$-497.5 \pm 1906.4i$	0.253	303.4	C_F, L_g
	λ_3	-1197.5	-	-	-
	$\lambda_{4,5}$	$-93.9 \pm 868.7i$	0.107	138.3	C_F, L_g
	$\lambda_{6,7}$	$-3.3 \pm 384.6i$	0.009	61.2	C_g
	$\lambda_{8,9}$	$-35.6 \pm 63.9i$	0.487	10.2	PLL, L_g
	λ_{10}	-60.6	-	-	-
	$\boldsymbol{\lambda_{11,12}}$	$\mathbf{0.02 \pm 17.6}\boldsymbol{i}$	**0.001**	**2.8**	$\boldsymbol{V_{dc}}$ **dynamic, Outer PI**
	λ_{13}	-11.4	-	-	-
	λ_{14}	-7.1	-	-	-
	λ_{15}	-6.9	-	-	-
PLL 2 (sc=35%)	$\lambda_{1,2}$	$-550.3 \pm 1914.2i$	0.276	304.7	C_F, L_g
	λ_3	-1199	-	-	-
	$\lambda_{4,5}$	$-102.4 \pm 898.3i$	0.113	143.0	C_F, L_g
	$\lambda_{6,7}$	$-5.3 \pm 394.1i$	0.013	62.7	C_g
	$\boldsymbol{\lambda_{8,9}}$	$\mathbf{0.0098 \pm 131.1}\boldsymbol{i}$	**0.00007**	**20.9**	**PLL**, $\boldsymbol{L}_{\Gamma}30823$
	λ_{10}	-91.3	-	-	-
	$\lambda_{11,12}$	$-1.5 \pm 19.9i$	0.075	3.2	V_{dc} dynamic, Outer PI
	λ_{13}	-11.1	-	-	-
	λ_{14}	-6.9	-	-	-
	λ_{15}	-6.9	-	-	-

Table 3.5: PFs of modes $\lambda_{6,7}$, $\lambda_{8,9}$ and $\lambda_{10,11}$ in Model 2.

Description	**State Variable**	**DC-link voltage control**					
		PLL1(sc=20%)			PLL2(sc=35%)		
		$\lambda_{6,7}$	$\lambda_{8,9}$	$\boldsymbol{\lambda_{11,12}}$	$\lambda_{6,7}$	$\boldsymbol{\lambda_{8,9}}$	$\lambda_{11,12}$
DC-link	V_{dc}^2	0.0026	0.1268	**0.3445**	0.0043	0.0148	**0.4713**
Grid	$i_{1,d}^g$	0.0056	0.0752	0.0014	0.0106	0.0286	0.0034
	$i_{1,q}^g$	0.0041	0.0512	0.0026	0.0066	0.0461	0.0019
	$i_{g,d}^g$	0.0204	0.1375	0.0093	0.0361	0.0604	0.0143
	$i_{g,q}^g$	0.0289	**0.4308**	0.0061	0.0623	**0.2875**	0.0009
	$v_{PCC,d}^g$	0.0515	0.0615	0.0006	0.0985	0.00293	0.0002
	$v_{PCC,q}^g$	0.0199	0.0254	0.0016	0.0231	0.0229	0.0002
	$v_{c,d}^g$	**0.4224**	0.0899	0.0012	**0.3428**	0.1242	0.0005
	$v_{c,q}^g$	**0.4591**	0.0302	0.0020	**0.4331**	0.0344	0.0052
PLL	$\Delta\theta$	0.0021	**0.9587**	0.1089	0.0113	**0.5515**	0.0139
	$\Delta\omega$	0.0001	**0.3438**	0.0869	0.0021	**0.2693**	0.0137
Outer-loop	i_{1d}^c	0.0001	0.1399	**0.3392**	0.0010	0.0090	**0.4692**
	i_{1q}^c	0.0008	0.1325	0.1109	0.0015	0.0376	0.0361
Inner-loop	u_d	0.0002	0.0014	0.0017	0.0001	0.0005	0.0024
	u_q	0.0001	0.00594	0.0237	0.0002	0.0196	0.0031

low-frequency (2 $\sim$ 5 Hz) mode $\lambda_{11,12}$ is related to dc-link capacitor dynamics, outer control loop. It moves towards the LHP with increasing series compensation level.

When PLL 1 is applied, the low-frequency mode is the dominant mode. When PLL 2 is applied, the 8 $\sim$ 20 Hz mode is the dominant mode. Further more, increasing sc level poses stability risk for the case with PLL 2. In another word, PLL with high bandwidth may pose oscillatory stability issue for type-4 wind in series compensated network.

Time-domain simulation results based on Model 2 are presented in Fig. 3.12. The parallel RL circuit is tripped at $t = 1$ s, which leaves the type-4 wind radially connected to the series compensated line (sc is 35%) with DC-link voltage control. Simulation results in Fig. 3.12a show that the system is stable for PLL 1. However, for PLL 2 as shown in Fig. 3.12b, the system is unstable.

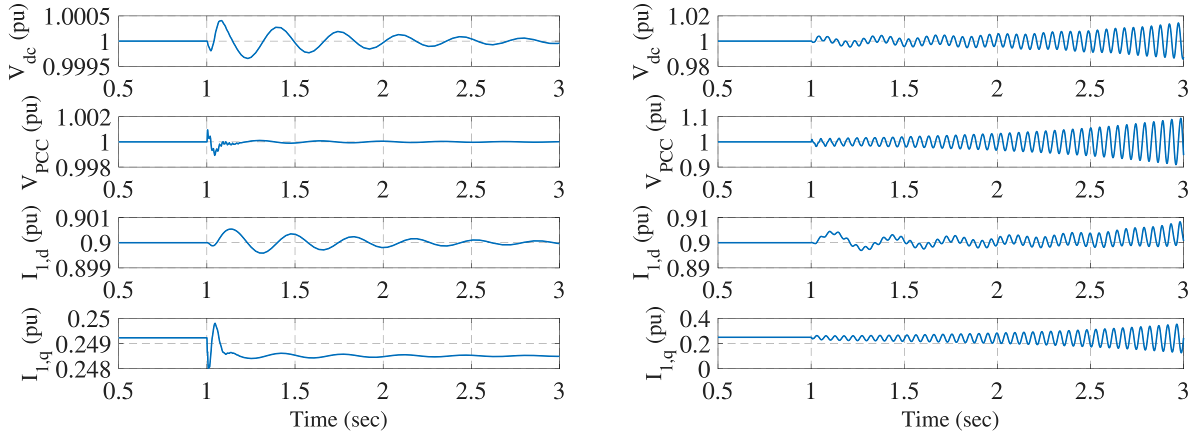

(a) (b)

Figure 3.12: Model 2 dynamic responses following an event of a line trip at 1 sec.

3.5.2 EMT Testbed Validation

The EMT dynamic validation results based on Testbed 2 are shown in Fig. 3.13. Fig. 3.13a adopts PLL 1 and Fig. 3.13b adopts PLL 2. At the $t = 2$ s, the non-compensated line is tripped. 3 Hz oscillations are observed for the system with PLL 1. Increasing the sc level from 20% to 30% makes the system stable. On the other hand, a 20 Hz oscillations occur if PLL 2 is used. Increasing sc level from 30% to 35% makes the system unstable.

The dynamic performances corroborate with the results based on eigenvalue analysis shown in Fig. 3.11. That is, with the increasing compensation level, the low-frequency mode moves to the left and the 8 ∼ 20 Hz mode moves to the right. PLL has a great influence on the 8 ∼ 20 Hz mode and system stability. High PLL bandwidth leads to a dominant 20 Hz mode.

3.6 Impedance-based Stability Analysis

In the literature, frequency-domain impedance models are either measured using harmonic injection method (e.g., [21]) or derived by conducting linearization at every stage for every equation (e.g., [76, 77]). Alternatively, small-signal time-domain state space model is first derived, with linearization conducted at every stage for every equation. With a device's terminal voltage treated as the input and the current flowing into the device as the output, the admittance of the device may be found as the frequency-domain transfer function. This approach has been adopted in [6,71,78,79] to find admittance or impedance models.

In this chapter, a computing efficient approach of finding impedance through nonlinear analytical model is presented. Compared to the approach in the literature, linearization is carried out in one step via numerical perturbation.

Approach for obtaining the admittances of wind farm from the analytical model is illustrated in Fig. 3.14. The admittance of the wind farm viewed from the PCC bus is desired. To find the admittance, the integration system is constructed to have the PCC bus directly connected to the grid voltage source. Based on this assumption, the analytical model of the system is constructed in the dq-frame. Using numerical perturbation (e.g., Matlab command `linmod`), lineraized model can be found. An input/output linearized model is found with the dq-axis voltages as input and the dq-axis currents as output. This input/output representation is indeed the admittance model of the wind farm.

The linear model is a 2 × 2 admittance matrix as follows.

$$\begin{bmatrix} i_{s,d}(s) \\ i_{s,q}(s) \end{bmatrix} = \underbrace{\begin{bmatrix} Y_{dd}(s) & Y_{dq}(s) \\ Y_{qd}(s) & Y_{qq}(s) \end{bmatrix}}_{Y_{\text{vsc},dq}} \begin{bmatrix} v_{s,d}(s) \\ v_{s,q}(s) \end{bmatrix} \tag{3.19}$$

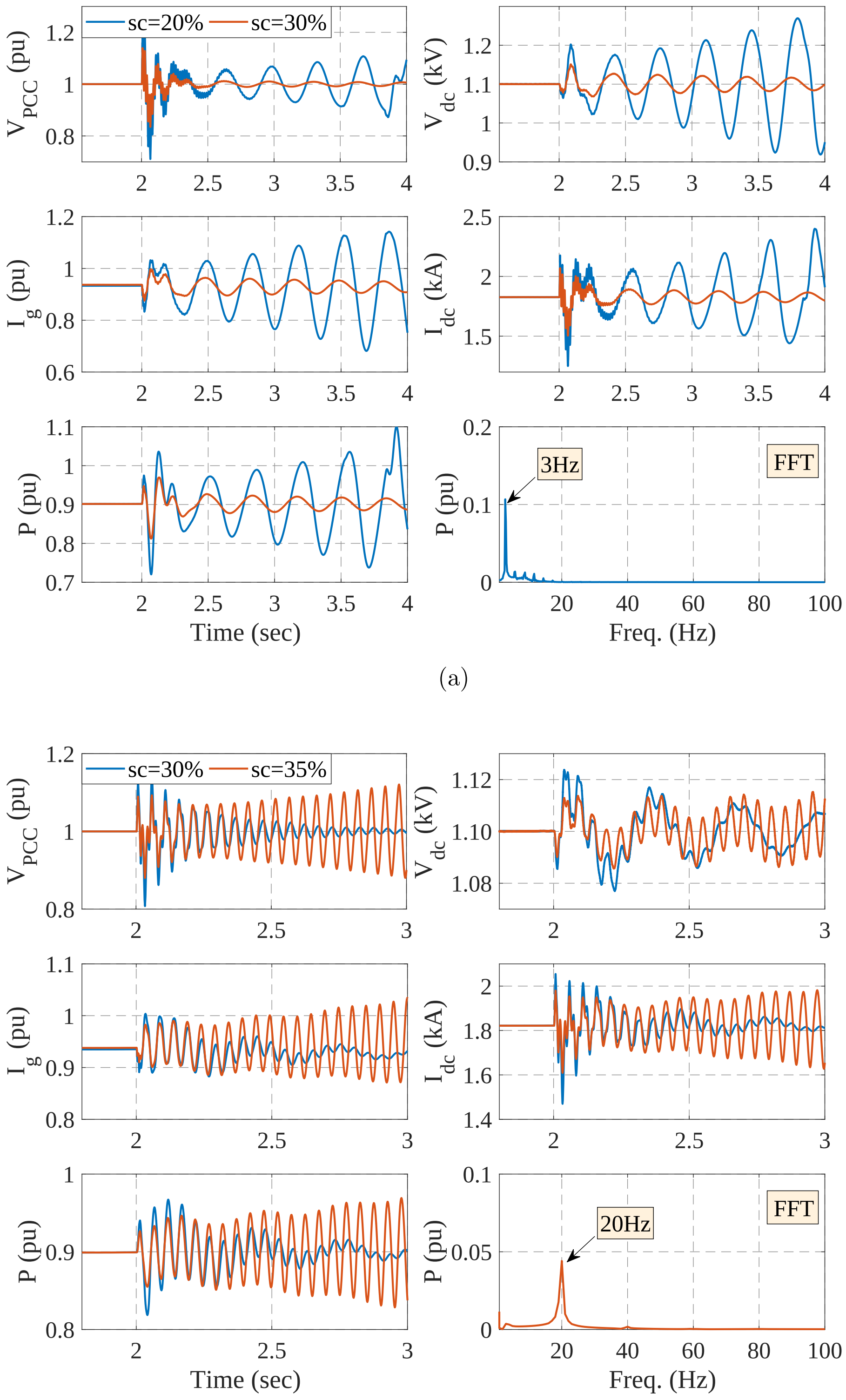

(a)

(b)

Figure 3.13: Dynamic performances of two different compensation levels under V_{dc} control in MATLAB/Simscape.

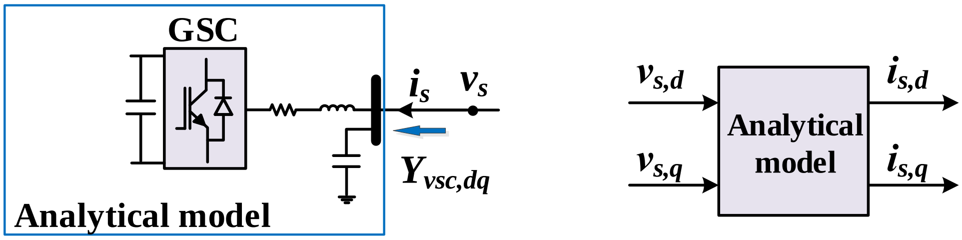

Figure 3.14: Approach to find impedance/admittance.

For a series compensated transmission line, the impedance model in dq-domain is expressed as [80]:

$$Z_{L,dq} = \begin{bmatrix} R + Ls + \frac{s}{C(s^2+\omega_0^2)} & -L\omega_0 + \frac{\omega_0}{C(s^2+\omega_0^2)} \\ L\omega_0 - \frac{\omega_0}{C(s^2+\omega_0^2)} & R + Ls + \frac{s}{C(s^2+\omega_0^2)} \end{bmatrix} \tag{3.20}$$

3.6.1 Stability Assessment

Impedance-based stability analysis is carried out for analytical model 2 (wind farm GSC in dc-link voltage control mode). Stability of a multi-input multi-output (MIMO) system can be assessed by the Generalized Nyquist Criterion (GNC), which has been popularly used in stability analysis, e.g., [26,81–83]. The loop gain of the system is defined in (3.21). The system will be unstable when characteristic loci of two eigenvalues of the loop gain (λ_1 and λ_2) encircle the point (-1, 0) clockwise in the Nyquist diagram. Instability is also reflected in Bode plots as the magnitude greater than 0 dB when the phase shift happens for the two eigenvalues.

$$L = Y_{\text{vsc},dq} \times Z_{L,dq} \tag{3.21}$$

Fig. 3.15 presents a stable case (case 1: $sc = 25\%$ for upper row Fig. 3.15a and Fig. 3.15b) and an unstable case (case 2: $sc = 40\%$ for lower row Fig. 3.15c and Fig. 3.15d) for Model 2 with a high bandwidth PLL considered (PLL 2). For case 1, Fig. 3.15a Bode plot shows that phase shifting occurs at 22.58 Hz. The magnitude of the eigenvalue at 22.58 Hz is less than 1. Hence the system is stable. The Nyquist diagram in Fig. 3.15b indicates the contour does not encircle

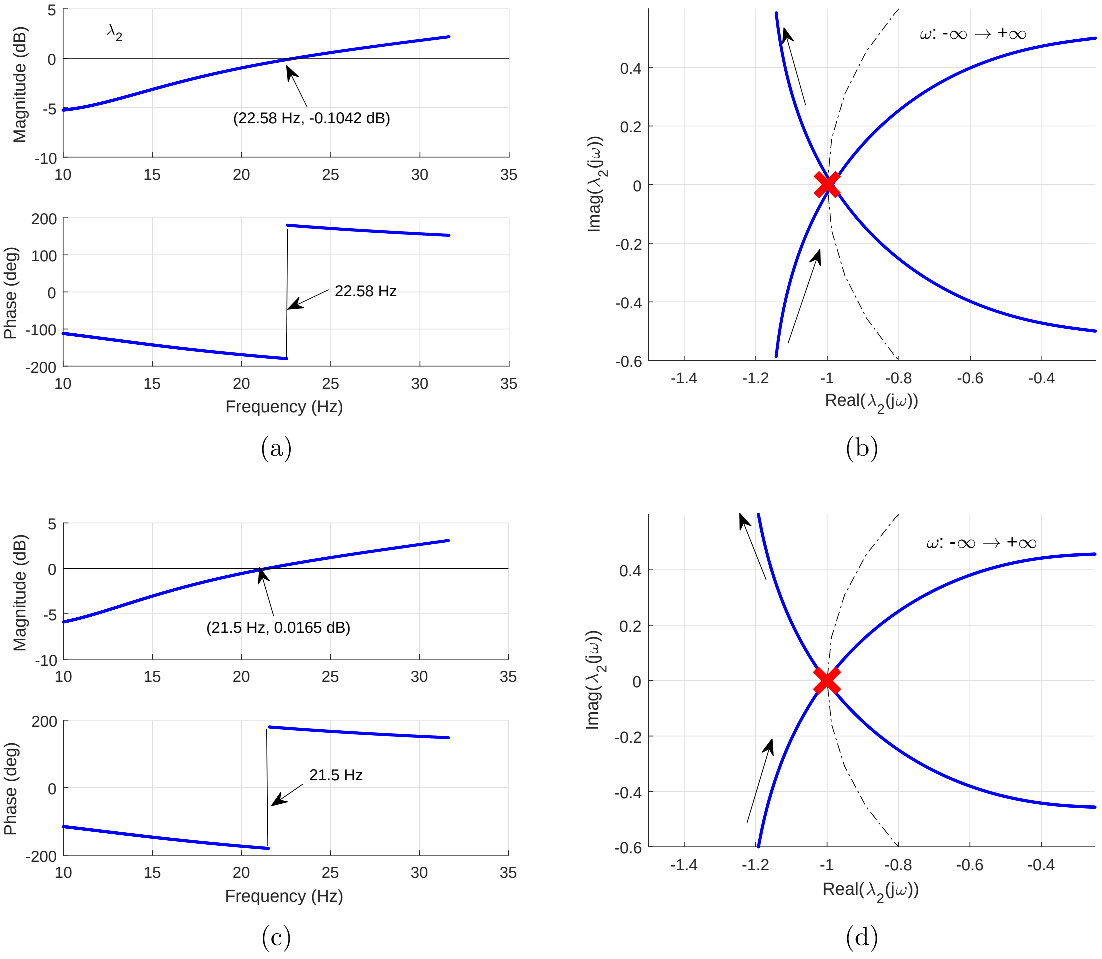

(a) (b)

(c) (d)

Figure 3.15: Impedance-based stability analysis for Analytical model 2 with high bandwidth PLL applied.

(-1,0). Hence the system is stable. For case 2, the Bode plot in Fig. 3.15c shows that phase shifting occurs at 21.5 Hz. The corresponding magnitude of the eigenvalue is greater than 1. Hence the system is unstable. Instability is also confirmed by the Nyquist diagram in Fig. 3.15d where (-1,0) is encircled clockwise.

The analysis results confirm the analysis in Section 3.5 and the major finding of this chapter: when series compensation is used to reduce electric distance for type-4 wind farm integration systems, instability may occur.

3.7 Conclusion

Small-signal stability analysis of type-4 wind in series compensated network is conducted relying on state-space analytical models and impedance models. Under weak grid conditions, increasing series compensation level may pose oscillatory stability issues due to interaction of a mode associated to voltage source converter (VSC) in weak grid (termed as "weak grid mode") and a mode associated to network LC resonance. Grid strength and Type-4 wind's GSC control parameters, including phase-locked-loop (PLL) parameters, play a big role on the dominant mode and stability. The analysis presented in this chapter is based on two analytical models built in *dq*-frames with grid dynamics and GSC control included. Analytical results and remarks are verified in two EMT testbeds with full dynamics, including grid dynamics, wind turbine mechanical and machine dynamics, and all stages of converter controls.

Chapter 4: Admittance Identification of IBGs for Stability Prediction

4.1 Introduction

This chapter [2] presents measuring admittance in the sequence- and/or *dq*-domain for type-3 and type-4 wind in series compensated networks. Frequency scans have been employed by the grid industry to obtain the frequency-domain measurements of wind farm admittances. The admittance can be in a scalar or a 2×2 matrix. The positive-sequence scalar admittance can be used assess subsynchronous resonance (SSR) for type-3 wind farms interconnected to series compensated networks. However, it is known that positive-sequence admittance has limitations for stability analysis of type-4 wind in weak grids because of significant frequency-coupling effect. Sequence-domain and *dq*-domain admittance, on the other hand, can provide accurate analysis results.

To the author' best knowledge, though the relationship between sequence-domain admittance and *dq*-domain admittance has been established in the literature, derivation that leads to the relationship is not thorough. Reference [26] gives a derivation based on the relationship between *dq*-domain phasors and sequence-domain phasors. Such derivation misses the critical link: the static *abc*-frame. Thus, the derivation in [26] lacks the capability to demonstrate the mirror frequency component. This research will fill the gap to demonstrate that both primary ω_1 component and the mirror frequency $(2\omega_0 - \omega_1)$ component appears in the static *abc*-frame currents for a voltage perturbation at ω_1 frequency. The theoretic analysis also leads to a direct implementation procedure on how to use the fast Fourier transform (FFT) analysis results to assemble sequence-domain admittance matrix.

Frequency scans result in frequency-domain measurement points, instead of a model. Additional method (e,g., Vector fitting) is required to arrive at a model. To address this concern, time-domain data-base method relying on system identification algorithm proposed in [30] is implemented. Only

---

[2] The majority of this chapter was under review in Electric Power Systems Research [84], 2021.

two experiments are required to identify a dq-domian admittance model. The obtained admittance model is compared with that obtained from frequency scans and shows close match in frequency-domain responses. Eigenvalue-based stability analysis employing the identified admittance model further demonstrates the practical use of admittance model in accurate stability analysis.

In this chapter, three methods to measure or identify admittances for a type-4 wind farm will be presented: frequency scan in the static frame and dq-frame, and time-domain data-based identification in the dq-frame. The first method leads to sequence-domain admittance, which can be further converted to a dq-domain admittance. The latter two lead to dq-domain admittances. The resulting dq-domain admittance measurements are compared for consistency. Further, s-domain admittance model-based eigenvalue analysis is carried out to demonstrate the effectiveness of stability prediction.

4.2 Limitation of Positive-sequence Impedance-based Analysis

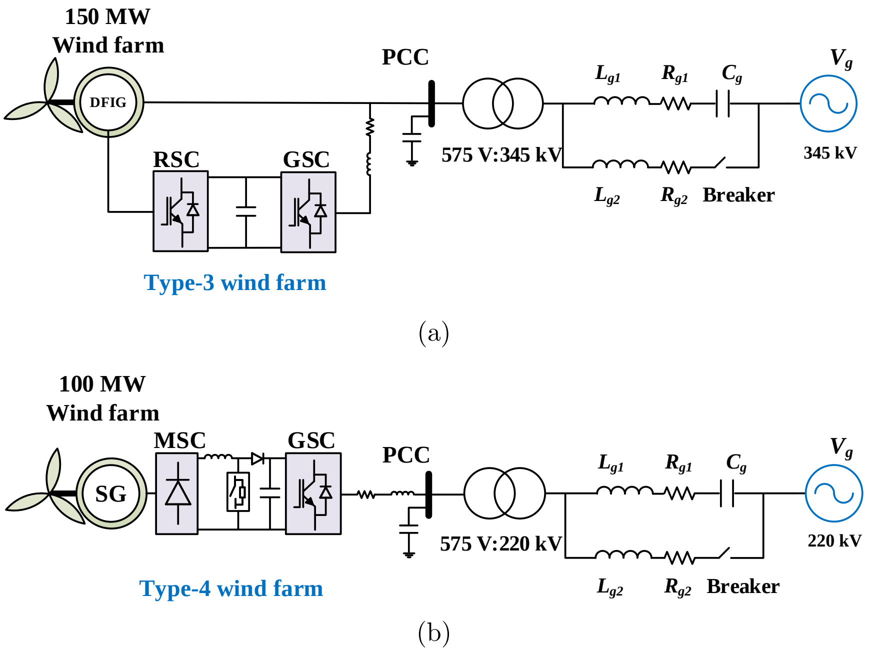

(a)

(b)

Figure 4.1: EMT testbeds: Type-3 wind farm and type-4 wind farm in a series compensated network.

In this section, two oscillatory incidents will be demonstrated in a grid-connected type-3 wind farm and a grid-connected type-4 wind system, see Fig. 4.1. Both testbeds are developed based

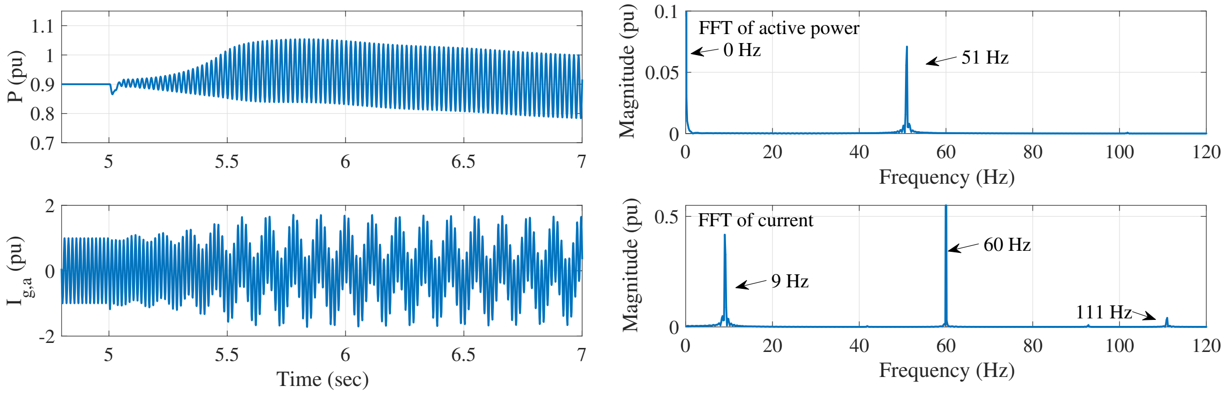

(a) (b)

Figure 4.2: Dynamic responses of type-3 wind at compensation level 20%.

on Matlab/SimPowerSystems demos. Full details of electromagnetic transients related to machines and circuits, as well as various converter controls have all been included. Both wind farms are connected to the power grid through two parallel transmission lines (one non-compensated line and one series compensated line). The compensated line is represented by a RLC line with the impedance $R_g + j(X_L - X_C)$. Resistance R_g is 10% of the reactance and 20 % series compensation (SC) level is assumed.

At 5 seconds, the non-compensated line is tripped. Subsequently, the wind farm will be connected to the series compensated line only. The dynamic responses of active power export from the wind, phase-a grid current from the point of common coupling (PCC) bus to the grid, and corresponding fast Fourier transform (FFT) results of the two testbeds are shown in Figs. 4.2-4.3. Instabilities are observed in both wind farms. The type-3 wind farm suffers a 9 Hz and a 111 Hz oscillation in current. The power shows oscillations with a complementary frequency at 51 Hz. For the type-4 wind testbed, the current shows two oscillation components (57.2 Hz and 62.8 Hz) and power has an oscillation component at 2.8 Hz.

It is noted that FFT is an important tool to find Fourier coefficients or phasors at different frequency. The frequency domain f can be calculated using

$$f = \frac{nf_s}{L}$$

where f_s is sampling frequency, L is length of signal, and n is frequency index starting from 0 to L/2. While, the single-sided magnitude spectrum of signal (M) can be found from

$$M = 2\frac{Y_1}{L_1}$$

where Y_1 is the even-valued Fourier coefficients of Y (obtained using Matlab command `fft`) and L_1 is even-valued signal length based on L. In this research, the EMT testbed is simulated for 10 seconds. FFT calculation is carried out over the selected time (4s-10s) that the signal was acquired. The sampling frequency and the size of the signal samples for FFT are selected as 20000 Hz and 120002, respectively.

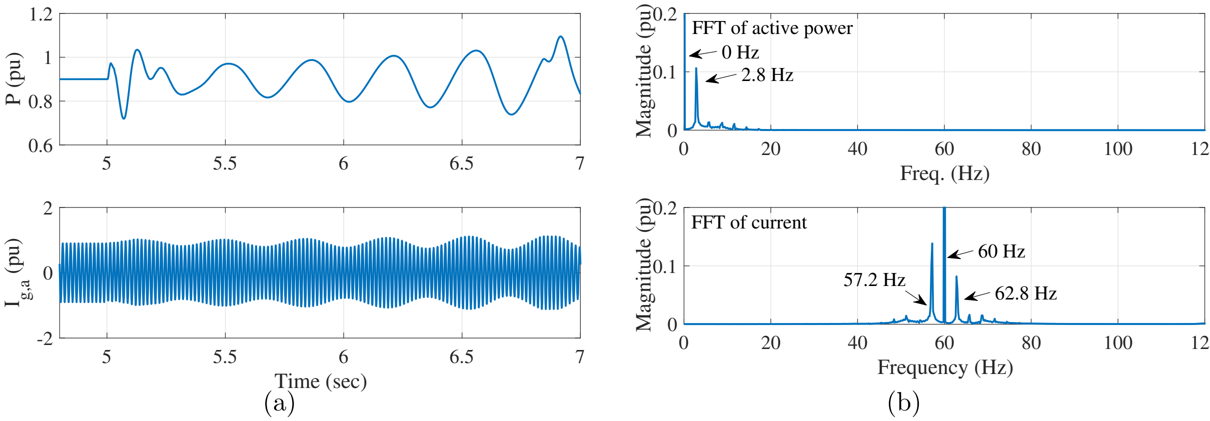

Figure 4.3: Dynamic responses of type-4 wind at compensation level 20%.

4.2.1 Positive-sequence Impedance-based Analysis

The impedance measurement testbeds are shown in Fig. 4.4. In the measurement testbeds, an ideal voltage source with nominal frequency ω_0 is connected to the PCC bus. Considering that the grid side converter (GSC) adopts PCC voltage control, a small inductive impedance is inserted between the PCC bus and grid voltage. The wind farm is at the same operating condition as it is in the EMT simulation testbed.

A series voltage source v_{inj} at a specific frequency is connected in series with the grid voltage source V_g. The current leaving the PCC bus to the grid voltage is measured. FFT is performed to

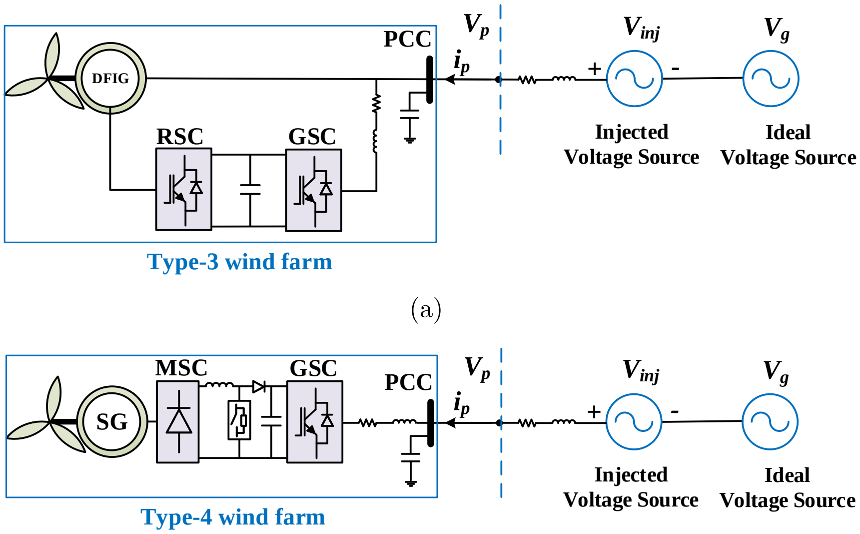

(a)

(b)

Figure 4.4: Measurement testbeds of type-3 wind and type-4 wind.

find Fourier coefficients for frequency components. Ratio between the Fourier coefficients of voltage and current is called impedance.

The mirror frequency coupling effect has been discovered for converters [26]. Assume that ω_1 is injected frequency, then the mirror frequency is defined as ω_2 and $\omega_2 = 2\omega_0 - \omega_1$. The coupling effects will be theoretically demonstrated in Section III.

If frequency coupling effect is ignored, for each perturbed frequency, frequency scans will give a scalar or positive-sequence impedance. References [34,80] have demonstrated that positive-sequence impedance is suitable to assess the stability of type-3 wind with series compensation interconnection. The positive-sequence impedance of a type-3 wind farm or a type-4 wind farm can be obtained as follows.

$$Z_{\text{Type}-3}(j\omega_1)(\text{or } Z_{\text{Type}-4}(j\omega_1)) = \frac{v_{\text{inj}}(j\omega_1)}{i_p(j\omega_1)} = \frac{\bar{V}_{\text{inj}}}{\bar{I}_1} \tag{4.1}$$

where $\bar{V}_{\text{inj}}$ and $\bar{I}_1$ respectively represent the complex Fourier coefficients of the injected voltage and the grid current at ω_1.

The impedance of series compensated transmission line viewed from the static frame can be expressed as

$$Z_{\text{net}} = R_g + L_g s + \frac{1}{C_g s}. \tag{4.2}$$

The line impedances of type-3 and type-4 wind farm testbeds are different and they are hereafter named as as Z_{net1} and Z_{net2}, respectively. The parameters of series compensated transmission line for both testbeds are given in Table 4.1. The values are in pu if not specified.

Table 4.1: Parameters of series compensated transmission line.

Description		**Values**
Testbed 1 **Type-3 wind**	Power base	156 MW
	Vbase	345 kV
	Grid frequency	60 Hz
	Line inductance L_{g1}	0.9
	Line X/R ratio	11.2
	Series line compensation level	20%
Testbed 2 **Type-4 wind**	Power base	100 MW
	Vbase	220 kV
	Grid frequency	60 Hz
	Line inductance L_{g2}	0.7
	Line X/R ratio	10
	Series line compensation level	20%

The Bode plots of positive-sequence wind impedance ($Z_{\text{Type}-3}/Z_{\text{Type}-4}$) and network impedance ($Z_{\text{net1}}/Z_{\text{net2}}$) at compensation level 20% are plotted in Fig. 4.5.

The difference between the phase angles at the point of matching magnitudes at 8.9 Hz is about -180° for the type-3 wind turbine case, which indicates SSO at 8.9 Hz. Since the impedance is in the static *abc*-frame, in the *dq*-frame or power measurement, the oscillation frequency is 51 Hz. This analysis result corroborates with the EMT testbed simulation results presented in Fig. 4.2.

For the type-4 wind, it is observed that the phase angle of $Z_{\text{net}}/Z_{\text{Type}-4}$ is greater than -180° at 7 Hz and 43 Hz when its magnitude is 1 or 0 dB. Based on the Bode plot, the system is stable, which is not the case, as shown in Fig. 4.3. It demonstrates that the positive-sequence impedance has limitation on the stability analysis of grid integrated type-4 wind systems.

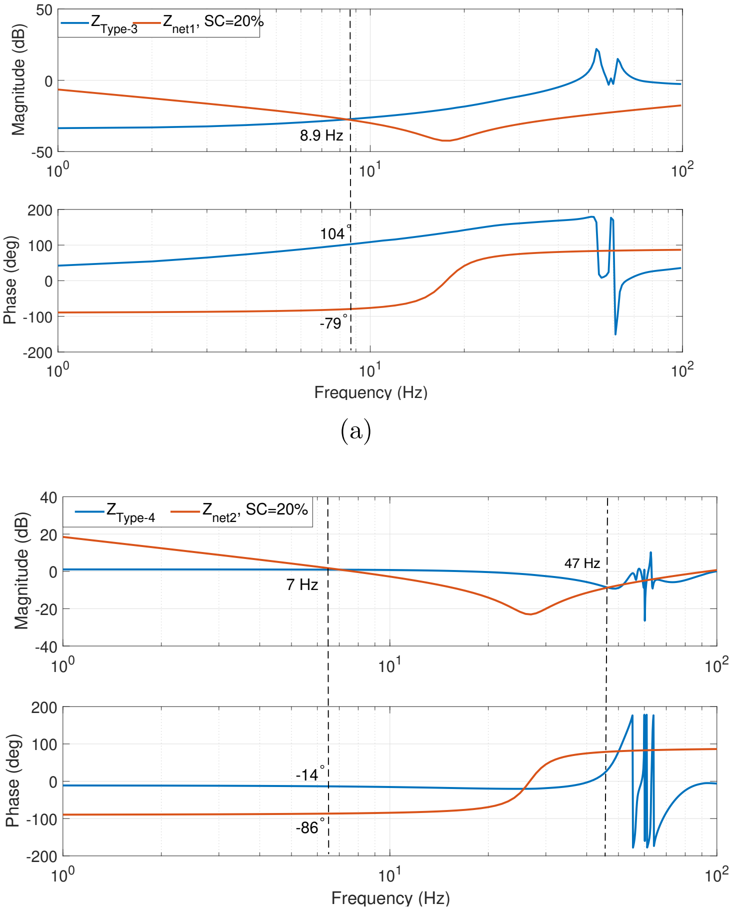

(a)

(b)

Figure 4.5: Bode plots of $Z_{\text{Type}-3}$, $Z_{\text{Type}-4}$, $Z_{\text{net}1}$, and $Z_{\text{net}2}$.

One plausible reason is that for type-3 wind turbine, frequency coupling effect is insignificant in the subsynchronous range. Thus, positive-sequence impedance analysis is feasible. On the other hand, for type-4 wind, frequency coupling effect cannot be ignored. This difference has been found for commercial wind turbines at National Renewable Energy Center, as documented in Chapter 3.5 of the Wind SSO Task Force report [17].

4.2.2 Frequency Coupling Effects

Fig. 4.6 presents the frequency coupling effects in type-3 and type-4 wind. In both plots, not only the perturbation frequency component, but also the mirror frequency component are plotted. $\bar{I}_2$ represents the current's Fourier coefficient of at the coupling frequency (ω_2). The primary admittance $I_1(s)/V_p(s)$ and coupling admittance $I_2(j2\omega_0 - s)/V_p(s)$ are compared over a spectrum of frequencies from 1 Hz to 100 Hz. In Fig. 4.6a, it is seen that I_1/V_p is significantly larger than I_2/V_p in the frequency range from $1 - 50$ Hz, which indicates that frequency coupling effect can be ignored for this frequency range in type-3 wind. On the other hand, in Fig. 4.6b, the primary admittance and the coupling admittance are almost identical, which implies that the coupling effect is significant. Thus, coupling effect must be considered for type-4 wind stability analysis.

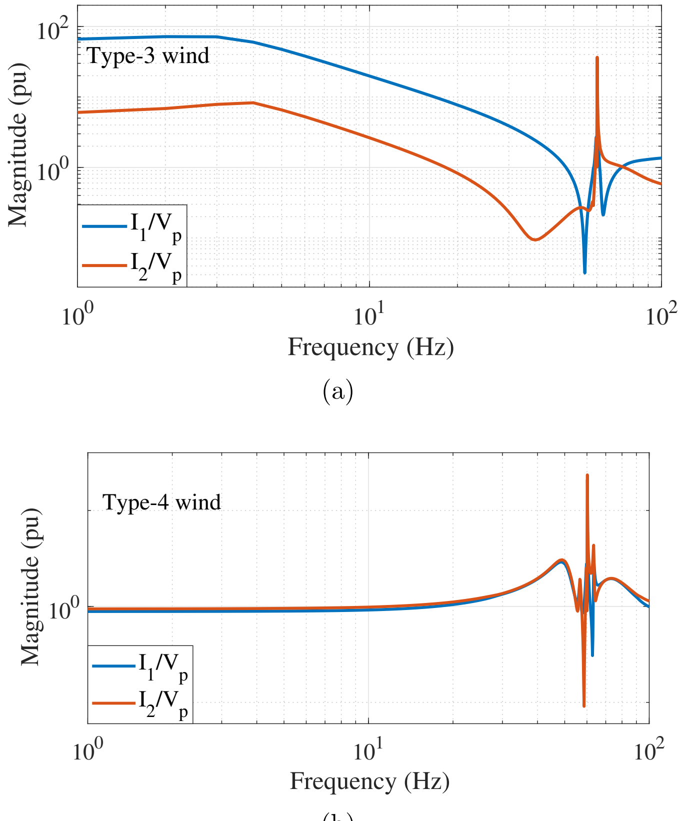

(a)

(b)

Figure 4.6: Impedance measurement of type-3 wind and type-4 wind to reflect the coupling effect.

4.3 Measuring Sequence-domain Admittance

This section presents the measurement procedure of finding sequence-domain admittance using frequency scans in the static *abc*-frame. Theoretical analysis is provided to prove the existence of mirror frequency component due to unsymmetrical *dq*-domain admittance. The detailed mathematical relationship between the current space vector and the admittance in *dq*-domain is given.

The goal of the derivation is to find in the static *abc*-frame, what are the frequency components of the current for a given voltage perturbation at ω_1 frequency. The *dq*-domain admittance is assumed to be given. The derivation procedure can be summarized as a four-step procedure: (i) converting the voltage perturbation in *abc*-frame to *dq*-frame and finding the phasors, (ii) using the *dq*-domain admittance to find current phasors in the *dq*-frame, (iii) converting the phasors into time-domain signals in the *dq*-frame, and (iv) finally converting the time-domain signals in the *dq*-frame back to the static *abc*-frame.

4.3.1 Injection Frequency Above the Fundamental Frequency

Assume that the injected voltage has a frequency above the fundamental frequency and below the 2nd harmonic frequency: $\omega_0 < \omega_1 < 2\omega_0$. The space vector of the injected three-phase voltage can be expressed in the following form:

$$\overrightarrow{v}_p = \overline{V}_p e^{j\omega_1 t} = |V_p| e^{j\theta_p} e^{j\omega_1 t} \tag{4.3}$$

where $\overline{V}_p$ is the phasor and $\overline{V}_p = |V_p| e^{j\theta_p}$, $|V_p|$ is the amplitude, and θ_p is the phase angle.

4.3.1.1 Step 1

When this space vector is viewed in the *dq*-frame where the *d*-axis is ahead of the static reference frame by an angle $\omega_0 t$ and *q*-axis is 90 degree ahead of the *d*-axis, it is expressed as follows.

$$\overline{V}_{dq} = \overrightarrow{v}_p e^{-j\omega_0 t} = \overline{V}_p e^{j\omega t} \tag{4.4}$$

where ω_0 is the nominal frequency and $\omega = \omega_1 - \omega_0$.

This vector $\overline{V}_{dq}$ is projected into the *d*-axis and the *q*-axis. The components are expressed as follows in the time-domain.

$$\begin{bmatrix} v_d(t) \\ v_q(t) \end{bmatrix} = \begin{bmatrix} \text{Real}(\overline{V}_{dq}) \\ \text{Imag}(\overline{V}_{dq}) \end{bmatrix} = \begin{bmatrix} |V_p|\cos(\omega t + \theta_p) \\ |V_p|\sin(\omega t + \theta_p) \end{bmatrix} \tag{4.5}$$

Eq. (4.5) leads to the following phasor expression.

$$\begin{bmatrix} \overline{V}_d \\ \overline{V}_q \end{bmatrix} = \begin{bmatrix} 1 \\ -j \end{bmatrix} \overline{V}_p \tag{4.6}$$

4.3.1.2 Step 2

The voltage phasors are related to the current phasors through the dq-frame admittance, which is represented by a transfer function matrix $Y_{dq}^m(s)$ as

$$\begin{bmatrix} \bar{I}_d \\ \bar{I}_q \end{bmatrix} = \underbrace{\begin{bmatrix} Y_{dd}(j\omega) & Y_{dq}(j\omega) \\ Y_{qd}(j\omega) & Y_{qq}(j\omega) \end{bmatrix}}_{Y_{dq}^m(j\omega)} \begin{bmatrix} \bar{V}_d \\ \bar{V}_q \end{bmatrix} \tag{4.7}$$

where the superscript m notates a matrix.

4.3.1.3 Step 3

In Step 3, the phasor expressions will be converted to the time-domain expressions. If a phasor is expressed as $\overline{V}$ at a frequency ω, this means that its analytic form is defined as $\widetilde{v}(t)$ and $\widetilde{v}(t) = \overline{V}e^{j\omega t}$. In turn, its time-domain expression $v(t)$ can be found as

$$v(t) = \text{Real}(\widetilde{v}(t)) = \frac{\widetilde{v}(t) + \widetilde{v}^*(t)}{2}. \tag{4.8}$$

where superscript $*$ represents complex conjugate.

Substituting (4.6) into (4.7), the analytical form of the dq-axis current at frequency ω can be represented as

$$\begin{bmatrix} \widetilde{i}_d(t) \\ \widetilde{i}_q(t) \end{bmatrix} = \begin{bmatrix} \bar{I}_d \\ \bar{I}_q \end{bmatrix} e^{j\omega t} = Y_{dq}^m(j\omega) \begin{bmatrix} 1 \\ -j \end{bmatrix} \overline{V}_p e^{j\omega t} \tag{4.9}$$

The conjugate of (4.9) can be expressed as

$$\begin{bmatrix} \tilde{i}_d^*(t) \\ \tilde{i}_q^*(t) \end{bmatrix} = \left(Y_{dq}^m(j\omega)\right)^* \begin{bmatrix} 1 \\ j \end{bmatrix} \bar{V}_p^* e^{-j\omega t} \tag{4.10}$$

From (4.9) and (4.10), the time-domain expressions $i_d(t)$ and $i_q(t)$ can be found by use of (4.8). Further the complex vector in the *dq*-frame $\overline{I}_{dq} = i_d(t) + ji_q(t)$ can be found as follows.

$$\begin{aligned} \overline{I}_{dq}(t) &= \begin{bmatrix} 1 & j \end{bmatrix} \begin{bmatrix} i_d(t) \\ i_q(t) \end{bmatrix} = \frac{1}{2} \begin{bmatrix} 1 & j \end{bmatrix} \left(\begin{bmatrix} \widetilde{i}_d(t) \\ \widetilde{i}_q(t) \end{bmatrix} + \begin{bmatrix} \tilde{i}_d^*(t) \\ \tilde{i}_q^*(t) \end{bmatrix} \right) \\ &= \underbrace{\frac{1}{2} \begin{bmatrix} 1 & j \end{bmatrix} Y_{dq}^m(j\omega) \begin{bmatrix} 1 \\ -j \end{bmatrix} \overline{V}_p \, e^{j\omega t}}_{\overline{I}_1} \\ &+ \underbrace{\frac{1}{2} \begin{bmatrix} 1 & j \end{bmatrix} (Y_{dq}^m(j\omega))^* \begin{bmatrix} 1 \\ j \end{bmatrix} \overline{V}_p^* \, e^{-j\omega t}}_{\overline{I}_2} \end{aligned} \tag{4.11}$$

It is clear that the current vector in the *dq*-frame has two components: one rotating counter clockwise at ω speed, the other rotating clockwise at the same speed.

4.3.1.4 Step 4

Hence, the current's space vector in the static frame *abc*-frame can be found as:

$$\overrightarrow{i}(t) = \overline{I}_{dq}(t) e^{j\omega_0 t} = \underbrace{\overline{I}_1 e^{j\omega_1 t}}_{\overrightarrow{i_1}} + \underbrace{\overline{I}_2 e^{j(2\omega_0 - \omega_1)t}}_{\overrightarrow{i_2}} \tag{4.12}$$

Two frequency components are observed in the *abc*-frame current. For phase a current, one component is the primary component $i_1(t)$ with frequency ω_1 and the other is the coupling component $i_2(t)$ at the mirror frequency $(2\omega_0 - \omega_1)$.

4.3.1.5 Remarks

The derivation clearly demonstrates the existence of the mirror frequency component. The relationship between the perturbation voltage phasor and the two current phasors can be defined as follows:

$$Y_{pp}(j\omega) = \frac{\overline{I}_1}{\overline{V}_p},\ \ Y^*_{np}(j\omega) = \frac{\overline{I}^*_2}{\overline{V}_p} \tag{4.13}$$

From (4.11), it can be found that

$$\begin{bmatrix} Y_{pp}(j\omega) \\ Y^*_{np}(j\omega) \end{bmatrix} = \frac{1}{2} \begin{bmatrix} 1 & j \\ 1 & -j \end{bmatrix} Y^m_{dq}(j\omega) \begin{bmatrix} 1 \\ -j \end{bmatrix} \tag{4.14}$$

The above derivation shows that with sinusoidal voltage injection, based on the two frequency components in the current, the primary admittance and the coupling admittance can be found. On the other hand, with two admittance components, the full *dq*-domain admittance matrix with 4 components cannot be recovered yet. Hence, a second experiment may be carried out to have two more admittance components.

4.3.2 Injection Frequency at the Mirror Frequency ω_2

In this experiment, the perturbation voltage has a frequency at ω_2, and $\omega_2 = 2\omega_0 - \omega_1$. If the previous experiment uses a frequency at 70 Hz as perturbation frequency, this experiment uses 50 Hz as the perturbation frequency. The space vector of the perturbation voltage is expressed as follows.

$$\overrightarrow{v}_n = \overline{V}_n e^{j(2\omega_0 - \omega_1)t} \tag{4.15}$$

The space vector viewed in the *dq*-frame is

$$\overline{V}_{dq} = \overrightarrow{v}_n e^{-j\omega_0 t} = \overline{V}_n e^{-j\omega t} \tag{4.16}$$

The real and imaginary components of $\overline{V}_{dq}$ are $v_d(t)$ and $v_q(t)$. Their phasors at ω frequency are as follows.

$$\begin{bmatrix} \overline{V}_d \\ \overline{V}_q \end{bmatrix} = \begin{bmatrix} 1 \\ j \end{bmatrix} \overline{V}^*_n \tag{4.17}$$

Following the same procedure as Step 3, the current space vector viewed in the dq-frame can be written as:

$$\overline{I}_{dq} = \underbrace{\frac{1}{2}\begin{bmatrix}1 & j\end{bmatrix} Y_{dq}^{m}(j\omega) \begin{bmatrix}1\\ j\end{bmatrix} \overline{V}_{n}^{*}\, e^{j\omega t}}_{\overline{I}_3} \\ \underbrace{+\frac{1}{2}\begin{bmatrix}1 & j\end{bmatrix} (Y_{dq}^{m}(j\omega))^{*} \begin{bmatrix}1\\ -j\end{bmatrix} \overline{V}_{n}\, e^{-j\omega t}}_{\overline{I}_4} \tag{4.18}$$

The current space vector in the abc-frame can be expressed as

$$\overrightarrow{i} = \overline{I}_3 e^{j\omega_1 t} + \overline{I}_4 e^{j(2\omega_0 - \omega_1)t}. \tag{4.19}$$

Thus the abc-frame current will have two frequency component: one at the primary frequency ω_1 and the other at the mirror frequency $(2\omega_0 - \omega_1)$.

The following definitions are given:

$$Y_{pn}(j\omega) = \frac{\overline{I}_3}{\overline{V}_n^{*}},\ \ Y_{nn}^{*}(j\omega) = \frac{\overline{I}_4^{*}}{\overline{V}_n^{*}} \tag{4.20}$$

From (4.18), it can be found that the two admittance components are related to the dq-domain admittance.

$$\begin{bmatrix}Y_{pn}(j\omega)\\ Y_{nn}^{*}(j\omega)\end{bmatrix} = \frac{1}{2}\begin{bmatrix}1 & j\\ 1 & -j\end{bmatrix} Y_{dq}^{m}(j\omega) \begin{bmatrix}1\\ j\end{bmatrix} \tag{4.21}$$

4.3.3 Relationship between Sequence and dq-domain Admittance Matrices

Based on (4.14) and (4.21), the coupling effects can be mathematically modeled by a 2 × 2 admittance in sequence domain notated as Y_{pn}^{m}. It has the following relationship with the dq-

domain admittance:

$$\underbrace{\begin{bmatrix} Y_{pp} & Y_{pn} \\ Y_{np}^* & Y_{nn}^* \end{bmatrix}}_{Y_{pn}^m} = \frac{1}{2} \underbrace{\begin{bmatrix} 1 & j \\ 1 & -j \end{bmatrix}}_{H} Y_{dq}^m(s) \underbrace{\begin{bmatrix} 1 & 1 \\ -j & j \end{bmatrix}}_{H^*}. \tag{4.22}$$

From (4.22), it can also be found the following relationship.

$$Y_{dq}^m(s) = \frac{1}{2} H^* Y_{pn}^m(s) H. \tag{4.23}$$

Fig. 4.7 presents the sequence-domain admittance measurement based on the above procedure. It can be clearly seen that Y_{pn} and Y_{np}^* components have comparable magnitudes as the diagonal components, indicating significant frequency coupling effect.

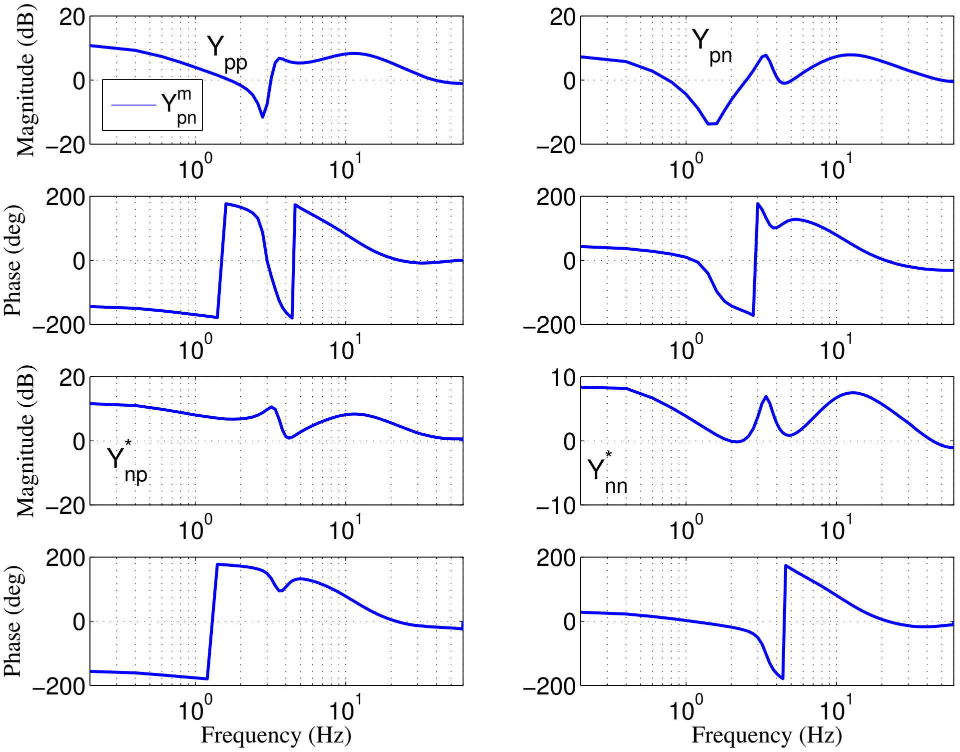

Figure 4.7: Sequence-domain admittance measurement.

4.3.4 Measurement Procedure

To summarize, in order to find the sequence-domain admittance Y_{pn}^m at any frequency ω, two perturbation tests are required. In the first test, perturbation voltage's frequency is ω_1 ($\omega+\omega_0$) (its phasor is notated as $\overline{V}_p$) while in the second test, perturbation voltage's frequency is the mirror frequency $2\omega_0 - \omega_1$ (or $-\omega + \omega_0$, its phasor is notated as $\overline{V}_n$). In the above discussion, ω is in the range of $0-60$ Hz so that the two perturbation frequencies are in the range of $60-120$ Hz or $0-60$ Hz. In both tests, the three-phase perturbation voltage is positive sequence.

This can be extended to a random frequency range. For example, in case to obtain the admittance at 70 Hz, the perturbation frequencies will be 130 Hz and -10 Hz. -10 Hz means that the perturbation voltage is negative sequence at 10 Hz.

For each test, FFT analysis will be conducted on three-phase currents to extract two component: one at ω_1 or $\omega+\omega_0$ and the other at the mirror frequency $2\omega_0-\omega_1$ or $-\omega+\omega_0$. With the four current phasors and the known perturbation voltage, the sequence-domain admittance can be found. Table 4.2 lists the two tests and the resulting current phasors.

Table 4.2: Voltage perturbation tests and the resulting current phasors.

Perturbation		**Response**	
Voltage	**Freq.**	**Current**	**Freq.**
$\overline{V}_p$	$\omega+\omega_0$	$\bar{I}_1$	$\omega+\omega_0$
		$\bar{I}_2$	$-\omega+\omega_0$
$\overline{V}_n$	$-\omega+\omega_0$	$\bar{I}_3$	$\omega+\omega_0$
		$\bar{I}_4$	$-\omega+\omega_0$

The sequence-domain admittance at frequency ω can be found as

$$Y_{pn}^m(j\omega) = \begin{bmatrix} \overline{I}_1/\overline{V}_p & \overline{I}_3/\overline{V}_n^* \\ \overline{I}_2^*/\overline{V}_p & \overline{I}_4^*/\overline{V}_n^* \end{bmatrix} \tag{4.24}$$

4.3.5 Example of Transfer Matrix Admittance Modeling

An example is presented to provide great insight. System is disturbed at 1 sec by injecting a positive sequence voltage at a certain frequency 70 Hz. Note that the injected voltage magnitude

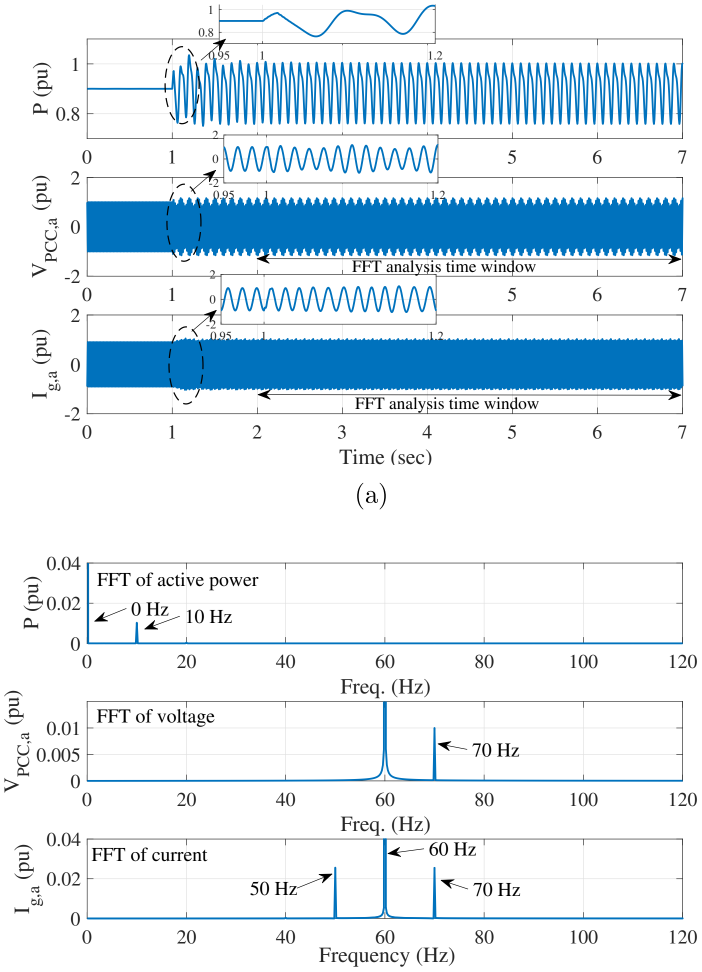

(a)

(b)

Figure 4.8: Time-domain measurements when 70 Hz voltage perturbation is injected at 1 sec.

should be kept relatively small [28, 85, 86]. In our study, $V_p = 0.01\angle 0$ pu is applied. Fig. 4.8 shows time-domain measurements of active power export from the type-4 wind farm, phase-A voltage at PCC bus, phase-A grid current from PCC bus to the grid, and the corresponding FFT results. Recording successive sections of voltage and current time-domain measurements, during the perturbation duration from 2 seconds to 7 seconds, to guarantee that an integer number of periods are acquired. Based on the finite set of data, Fast Fourier Transformation (FFT) calculate the frequency components of voltage and current and display them as frequency spectrum. The FFT results are shown in Fig. 4.8b. It is seen that current has sequence-domain harmonic components at 70 and 50 Hz. Correspondingly, *dq*-domain harmonic component with a complementary frequency (60 Hz-50 Hz=10 Hz) is observed in power. These are fully consistent with Table 4.2. The same procedure is applied when voltage perturbation is injected at 50 Hz. Calculated harmonic components of voltage and current for two independent perturbations (70 Hz and 50 Hz) are respectively recorded in Table 4.3 where the relevant frequency is indicated in the subscript.

Table 4.3: Harmonic components of voltage and current for two independent perturbations.

Perturbation		**Response**	
Phasor	**Freq.**	**Phasor**	**Freq.**
$\bar{V}_{p,70Hz} = 0.01\angle 0$	70 Hz	$\bar{I}_{1,70Hz} = 0.0256\angle 81.80°$	70 Hz
		$\bar{I}_{2,50Hz} = 0.0257\angle 101.97°$	50 Hz
$\bar{V}'_{p,50Hz} = 0.01\angle 0$	50 Hz	$\bar{I}'_{1,,50Hz} = 0.0218\angle -81.4°$	50 Hz
		$\bar{I}'_{2,70Hz} = 0.0233\angle -100.1°$	70 Hz

Using (4.13) and (4.20), the elements of transfer matrix admittance Y^m_{pn} are given, in the sequence-domain, as

$$Y_{pp} = \frac{\bar{I}_{1,70Hz}}{\bar{V}_{p,70Hz}} = 1.877\angle 84.10°,\ Y_{pn} = \frac{\bar{I}'_{2,70Hz}}{\bar{V}'^{*}_{p,50Hz}} = 2.96\angle -102.53°$$

$$Y_{np} = \frac{\bar{I}_{2,50Hz}}{\bar{V}^{*}_{p,70Hz}} = 1.88\angle 99.67°,\ Y_{nn} = \frac{\bar{I}'_{1,50Hz}}{\bar{V}'_{p,50Hz}} = 2.77\angle -78.94°$$

Using (4.23), transfer matrix admittance Y_{dq}^{m}, in the dq-domain, is computed subsequently. Repeating the same procedure for all injected frequency of interest (0 Hz-120 Hz). The admittance with the varying frequency can be obtained for further stability analysis.

4.4 dq-domain Admittance: Frequency Scans and System Identification

In this section, two methods will be introduced to give admittance measurement or lead to an input/output model. Both methods are based on the dq-frame. The first method is based on frequency scans and the second method is based on step-response data-driven method relying on Eigensystem Realization Algorithm (ERA). The details of the latter method has been introduced in [30]. The key idea is to use the system identification method, e.g., ERA, to identify the eigenvalues and residues from a time-domain signal. The objective of ERA is to find the s-domain expressions of the dq-frame currents. If the voltage perturbation transfer function is known, e.g., a step change, then an s-domain admittance model can be quickly found.

Both methods use the same measurement testbed as shown in Fig. 4.9. The grid source is represented by a controlled voltage source in the grid dq-frame. The steady-state v_d and v_q are 1 and 0 pu, respectively. The dq-frame is based on a synchronous rotating frame. The difference compared to the testbed in Fig. 4.4b, is that the perturbation is carried out in the dq-frame.

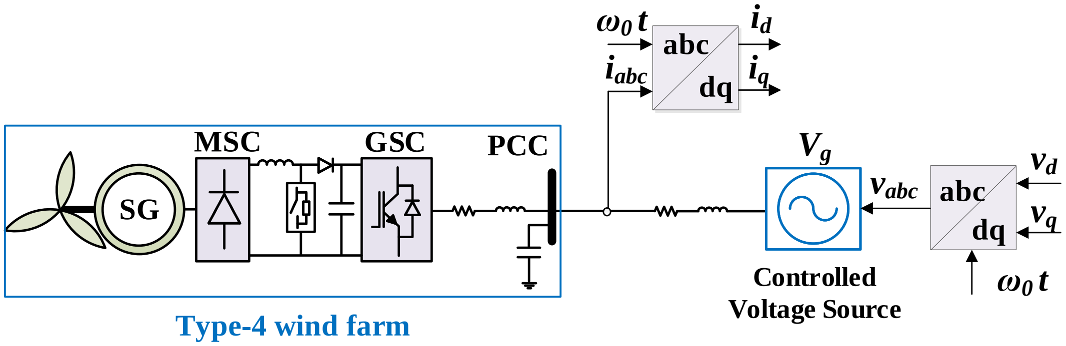

Figure 4.9: Dq-domain admittance measurement testbed.

4.4.1 Admittance Measurement based Frequency Scans

The admittance matrix at a single frequency can be obtained through two perturbation tests, one to perturb the d-axis voltage and the other to perturb the q-axis voltage.

1. Case 1: A sinusoidal voltage perturbation at frequency ω with small magnitude 0.01 pu is added to the steady-state v_d. The phasor of the perturbation voltage is notated as $\overline{V}_d$. The q-axis voltage is at its steady-state value. dq-axis currents are measured and FFT analysis are conducted to extract components at frequency ω. The two current phasors are notated as $\overline{I}_d^{(1)}$ and $\overline{I}_q^{(1)}$. From there, Y_{dd} and Y_{qd} are found.

2. Case 2: A sinusoidal voltage perturbation with small magnitude 0.01 pu is injected in v_q while the d-axis voltage is at its steady-state value. The phasor of the perturbation voltage is notated as $\overline{V}_q$. dq-axis currents are measured and FFT analysis are conducted to extract components at frequency ω. The two current phasors are notated as $\overline{I}_d^{(2)}$ and $\overline{I}_q^{(2)}$. From there, Y_{dq} and Y_{qq} can be found.

The admittance is associated to the dq-axis currents and dq-axis voltages as follows.

$$\begin{bmatrix} \Delta i_d(s) \\ \Delta i_q(s) \end{bmatrix} = -\underbrace{\begin{bmatrix} Y_{dd}(s) & Y_{dq}(s) \\ Y_{qd}(s) & Y_{qq}(s) \end{bmatrix}}_{Y_{dq}^m(s)} \begin{bmatrix} \Delta v_d(s) \\ \Delta v_q(s) \end{bmatrix} \tag{4.25}$$

The elements of admittance matrix at $s = j\omega$ can be computed as

$$\begin{aligned} Y_{dd}(j\omega) &= -\frac{\overline{I}_d^{(1)}}{\overline{V}_d},\ Y_{dq}(j\omega) = -\frac{\overline{I}_d^{(2)}}{\overline{V}_q} \\ Y_{qd}(j\omega) &= -\frac{\overline{I}_q^{(1)}}{\overline{V}_d},\ Y_{qq}(j\omega) = -\frac{\overline{I}_q^{(2)}}{\overline{V}_q} \end{aligned} \tag{4.26}$$

where superscript 1 indicates case 1 and superscript 2 indicates case 2. Negative signs are due to the current direction is out of the converter.

The aforementioned admittance Y_{dq}^m is built based on a dq-reference frame whose d-axis is aligned with the grid voltage.

4.4.2 Time-domain Step-response based Admittance Identification

Frequency scans require numerous experiments and FFT analysis to extract phasors from time-domain responses. In addition, the outcome is measurement instead of an s-domain model.

The method proposed in [30] requires only two experiments.

1. Experiment 1: A step change of 0.01 pu is applied in v_d ($\Delta v_d = 0.01/s$). From the time-domain responses of dq-current deviations, their d-domain expressions will be identified as $\Delta i_d^{(1)}(s)$ and $\Delta i_q^{(1)}(s)$. This step requires dynamic system identification algorithm, e.g., ERA. From there, $Y_{dd}(s)$ and $Y_{qd}(s)$ expressions are found as $-\Delta i_d^{(1)}(s)/\Delta v_d(s)$ and $-\Delta i_q^{(1)}(s)/\Delta v_d(s)$.
2. Experiment 2: A step change of 0.01 pu is applied in v_q and the s-domain expressions for the dq-axis currents are found $\Delta i_d^{(2)}(s)$ and $\Delta i_q^{(2)}(s)$. From there, $Y_{dq}(s)$ and $Y_{qq}(s)$ expressions are found as $-\Delta i_d^{(2)}(s)/\Delta v_q(s)$ and $-\Delta i_q^{(2)}(s)/\Delta v_q(s)$.

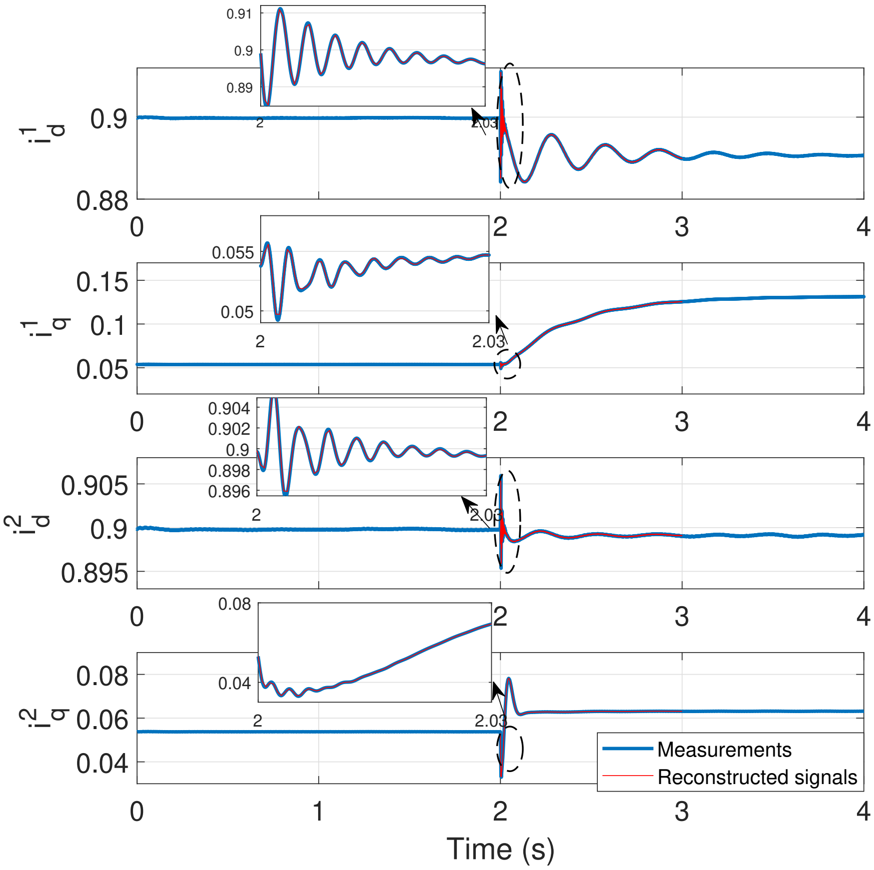

Figure 4.10: Time-domain current measurements from two experiments: $i_d^{(1)}, i_q^{(1)}$ for the experiment 1, and $i_d^{(2)}, i_q^{(2)}$ for the experiment 2 with step change of 0.01 pu is applied at t = 2 sec.

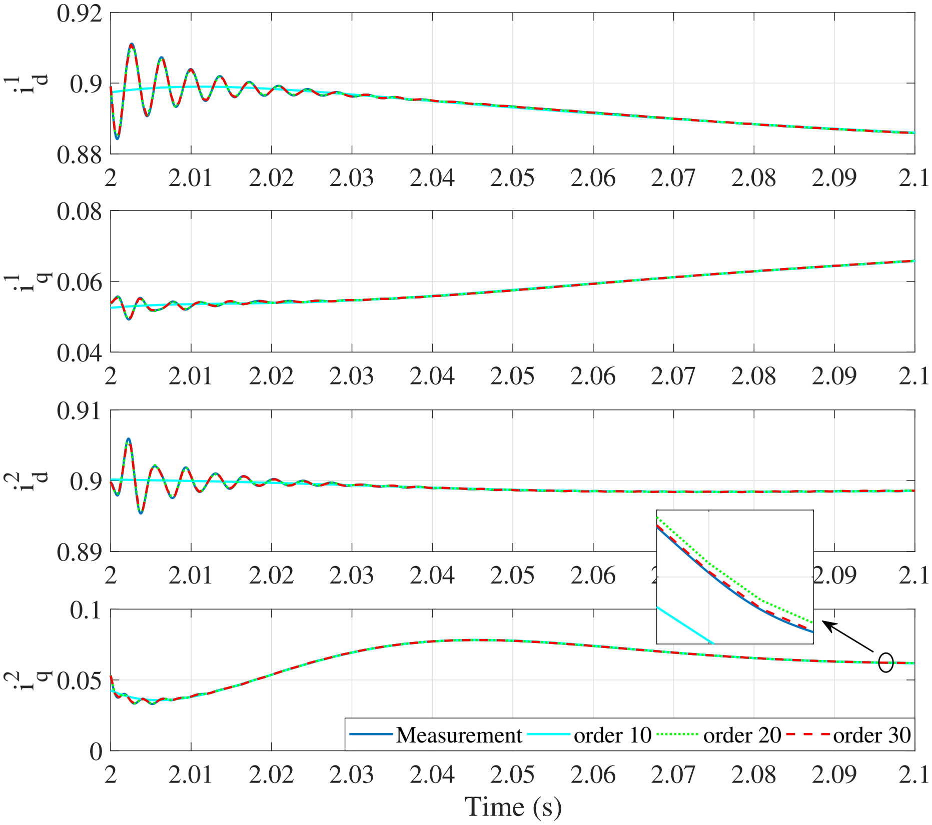

Figure 4.11: Comparison of 10th order, 20th order, and 30th order model from Eigensystem Realization Algorithm.

Fig. 4.10 shows the current dynamic responses $i_d^{(1)}, i_q^{(1)}$ for the experiment 1, and $i_d^{(2)}, i_q^{(2)}$ for the experiment 2. Blue curves are the recorded data. Data from 2-3 seconds are used for learning. The red curves are the reconstructed data after learning. It is observed that two curves match very well with 1000 Hz sampling frequency and 30^{th} system order. The order is chosen to be 30 after trial and error. At lower order, e.g., 10 or 20, the reconstructed signal poorly matches the measurements as shown in Fig. 4.11. The admittance is found and its Bode plots are shown in Fig. 4.12. This admittance is notated as Y_{ERA}. It is compared with the admittances obtained through frequency scan in the dq-frame (Y_{dq}^m) and $\frac{1}{2}H^*Y_{pn}^m(s)H$, where Y_{pn}^m is obtained from frequency scans in the stationary frame. Fig. 4.12 presents the comparison. It is observed the identified admittance matrices using different approaches have matching frequency responses.

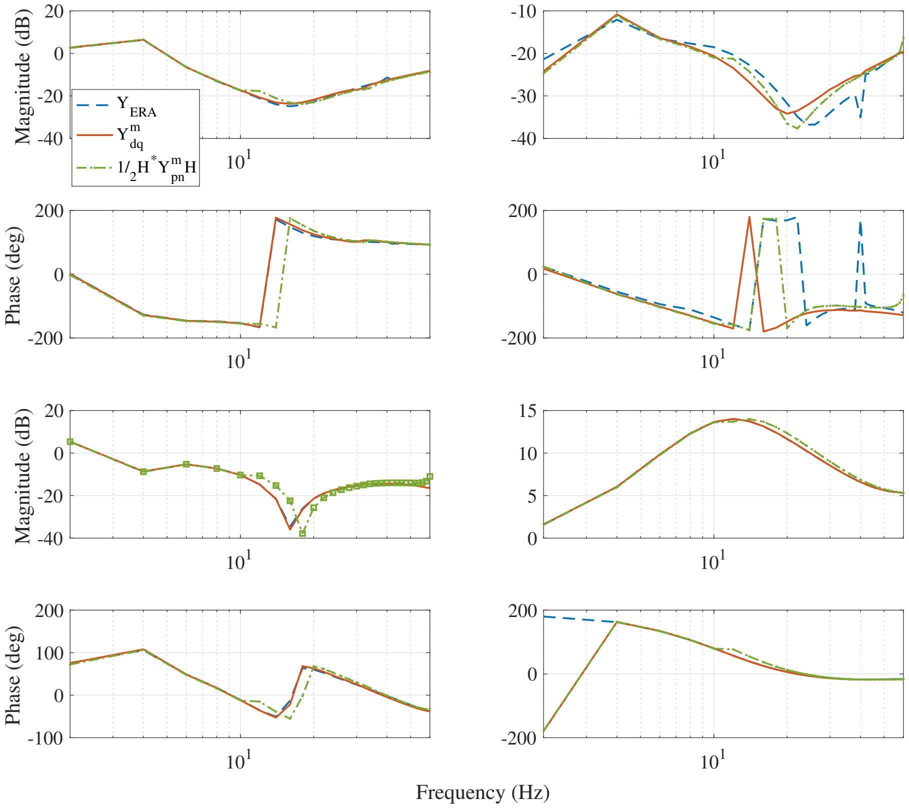

Figure 4.12: Comparison of dq-domain admittances obtained from three methods: Y_{ERA} using ERA, Y_{dq}^m using frequency scan in the dq-frame, and $\frac{1}{2}H^*Y_{pn}^m(s)H$ using frequency scan in the static-frame.

4.5 s-domain Admittance-based Eigenvalue Analysis

For a series compensated transmission line, the dq-domain impedance matrix is expressed as follows.

$$Z_{L,dq} = \begin{bmatrix} R + Ls + \frac{s}{C(s^2+\omega_0^2)} & -L\omega_0 + \frac{\omega_0}{C(s^2+\omega_0^2)} \\ L\omega_0 - \frac{\omega_0}{C(s^2+\omega_0^2)} & R + Ls + \frac{s}{C(s^2+\omega_0^2)} \end{bmatrix} \tag{4.27}$$

The total admittance viewed at the PCC bus is

$$Y_{\text{total}} = Y_{\text{ERA}} + Y_{L,dq} \tag{4.28}$$

where $Y_{L,dq} = Z_{L,dq}^{-1}$. If there is a shunt current injection at the PCC bus, notated as I_{inj}, the resulting PCC bus voltage deviation can be expressed as

$$Y_{\text{total}} \Delta V_{\text{PCC}} = \Delta I_{\text{inj}}.$$

With the current injection treated as the input and the PCC voltage treated as the output, the system's transfer function is Y_{total}^{-1}. Hence, the system's eigenvalues are the poles of Y_{total}^{-1}, or the zeros of Y_{total}. This approach of finding system eigenvalues through an s-domain admittance was proposed in [**?**] in 1990s. On the other hand, this approach finds few applications due to two reasons. For a simple circuit that can be viewed by a source and a load, frequency-domain analysis methods such as Generalized Nyquist Criterion is popular. On the other hand, for a sophisticated power grid with many nodes, the state-space modeling approach is popular and has been adopted by major power system dynamic analysis software packages, e.g., PowerTech Lab's SSAT. Indeed, the s-domain admittance-based method was re-introduced only most recently in [30, 87] for converter penetrated power grids.

The trajectory of eigenvalues is shown in Fig. 4.13 when the compensation level increases. It is observed that the dominant eigenvalues move toward left half-plane (LHP) with compensation level increasing from 10% to 75% with a step size of 2.5%. When compensation level is at 20%, a pair of eigenvalues $0.343 \pm j2\pi \times 3$ with a oscillation frequency 3 Hz, indicates instability. Increasing compensation is the same as increasing system strength and this mode moves to the LHP. The unstable mode identified by the eigenvalue analysis corroborates with the EMT testbed simulation results presented in Fig. 4.3, where FFT identifies 2.8 Hz oscillations. The above study demonstrates that admittance-based eigenvalue analysis leads to accurate stability prediction.

4.6 Conclusion

In this chapter, three methods to measure or identify admittance of type-4 wind farms, in sequence- or dq-domain, are presented along with the theoretical derivations. Details of the measurement testbed setup, measuring procedures are presented with theoretic explanation. The resulting admittances are compared for consistency. Furthermore, eigeevalue-based stability assessment

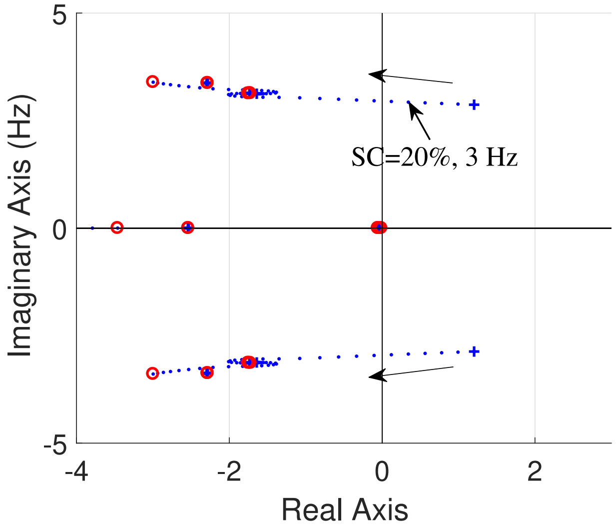

Figure 4.13: Trajectory of eigenvalues for increasing series compensation level from 10% to 75%.

relying on the admittance model identified gives accurate analysis results which corroborate with the EMT simulation results.

Chapter 5: Three-Phase Hybrid Boost Converter for IBGs

5.1 Introduction

This chapter presents a single-stage multi-port hybrid boost converter (HBC) to correctly regulate the dc and ac output while maintaining the closed-loop stability. A grid-connected DC-based power system (see chapter 1.5) is shown in Fig. 5.1(a). A IBG such as solar PV can be treated as a single dc input. The step-up dc-dc converter is used to supply dc loads and the grid connected voltage source converter (VSC) is cascaded to step-up dc-dc converter to supply ac loads. Separate converter with individual controller is required to achieve dc/dc and dc/ac conversions. This increases power loss, system complexity, and reduces the reliability. Hence, it is necessary to implement a HBC with lesser number of switches to supply dc and ac loads simultaneously as shown in Fig. 5.1(b) [88–90]. The HBC-based architecture reduces the unnecessary processes of dc/dc and dc/ac conversions compared with conventional converter-based architecture.

In this research, a scenario of the dc input and utility ac grid maintain continuous dc power supply is investigated. Detailed modeling of the HBC in the closed-loop control is developed to demonstrate the operating behavior. The vector control and hybrid pulse width modulation (PWM) methodology are presented. The performance of the HBC is investigated in a electromagnetic transient (EMT) testbed which is developed in MATLAB/Simscape. It is found that the HBC is capable of maintaining the smooth power transfer between the ac and dc outputs, correctly regulating the dc bus voltage while maintaining closed-loop stability.

5.2 Grid Connected Operation of the HBC

The circuit topology of the study system is shown in Fig. 5.2, where a dc source is connected to an utility grid and dc loads through a single stage three-phase HBC. It is noted that the dc source can be easily extended to most existing IBG such as solar PV operated in the maximum power point tracking (MPPT) mode to provide maximum power output. Symbols V_{in}, V_{dc}, and V_{pcc}

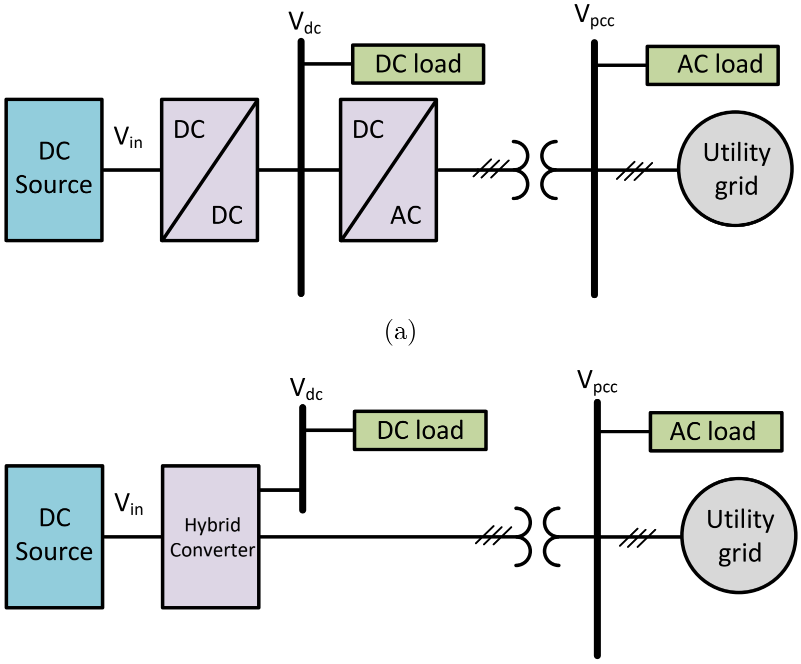

(a)

(b)

Figure 5.1: Representative schematic of grid-connected DC-based system: top is conventional converter-based architecture and bottom is HBC-based architecture.

represent the dc input voltage, dc output voltage, and point of common connection (PCC) voltage, respectively. The dc side includes one diode and one capacitor (C_{dc}) to provide a dc output at a different voltage level. The ac side is connected to the power grid though an RLC filter (R_f, L_f, C_f), two step-up transformers, and a transmission line (R_g, L_g) to get the sinusoidal ac output.

Compared to the separate converters to achieve dc/dc and dc/ac conversion, a single HBC performing both operations simultaneously. A single dc input provides a dc and ac output through the three-phase bridge network switches ($Q_1 - Q_6$), where the power switches can use either IGBT or MOSFET with anti-parallel diodes. Three operation modes of the HBC based on the switching states are shown in the Fig. 5.3 and described in the following.

5.2.1 Shoot-through Mode (m_{st})

Fig. 5.3(a) shows the power direction (blue line) in the study system for the shoot-through mode. In this mode, the shoot-through occurs by gating-on both switches of any one or two or all particular legs (either Q_1Q_4, Q_3Q_6, or Q_5Q_2) at the same time. In this work, all the legs are

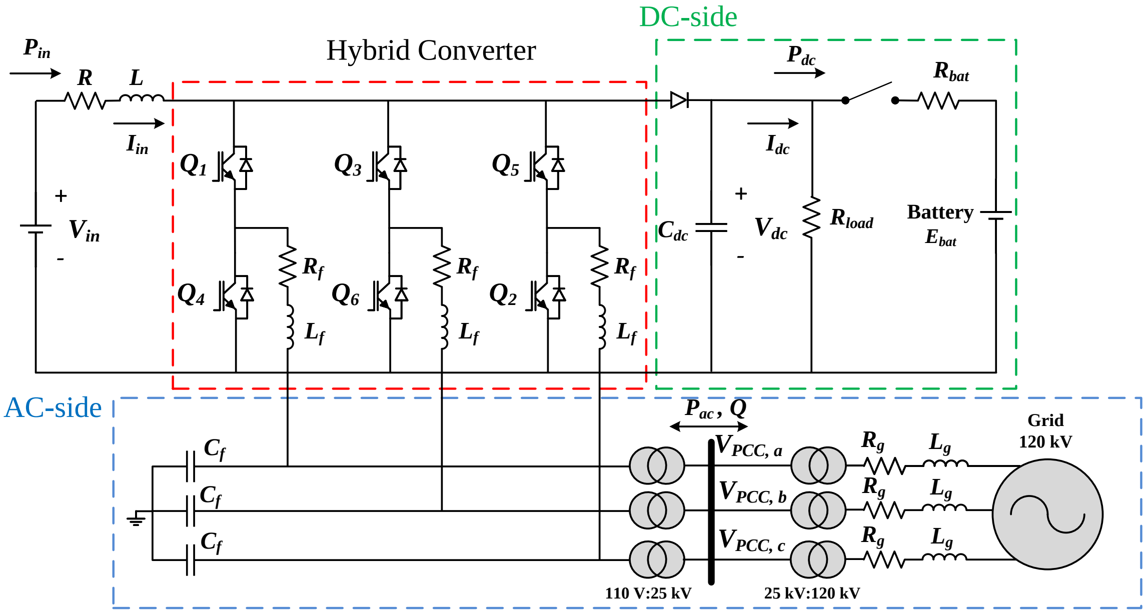

Figure 5.2: Three-phase HBC topology.

turned on to achieve the shoot through. The diode of the dc side is reversed biased and the current circulates in the bridge network switches. That is to say, the dc and ac output are zero. Moreover, L is charging in order to provide higher dc output voltage than the dc input voltage. The duration period of the shoot-through mode is defined as the duty cycle (D_{st}).

5.2.2 Power Mode (m_p)

The power mode is realized by gating on any two top or bottom switches and the opposite switch in the remaining leg. In this work, Q_1, Q_5, and Q_6 are turned on. In this mode, the diode of the dc side conducts and current partially flows to the ac side. The power direction is shown in Fig. 5.3(b) where the dc input powering both dc and ac output simultaneously.

5.2.3 Zero Mode (m_z)

Zero mode is activated when either all top or bottom switches are turned on. Q_2, Q_4, and Q_6 are on in this work. As shown in Fig. 5.3(c), the dc input power the dc side but no power flows into the ac side.

Similar to conventional boost converter, the duty cycle (D_{st}) regulates the dc output. The dc output voltage (V_{dc}) can be expressed in terms of the dc input voltage and the duty cycle as follows:

$$V_{dc} = \frac{V_{in}}{1 - D_{st}} \tag{5.1}$$

The modulation index (M_i) is used to regulate the ac output that is similar with that in the conventional VSC. The rms value of the line to line ac output voltage (V_{ac}) can be derived in terms of the dc input voltage, the duty cycle, and the modulation index as follows:

$$V_{ac} = \frac{\sqrt{3}}{2\sqrt{2}} M_i \frac{V_{in}}{1 - D_{st}} \tag{5.2}$$

To achieve continuous operation of the HBC, a limitation to the duty cycle and the modulation index must be satisfied.

$$M_i + D_{st} \leq 1 \tag{5.3}$$

The maximum ac output voltage can be obtained as $\frac{\sqrt{3}}{2\sqrt{2}} V_{in}$ at the equality condition of (5.3).

5.3 Control Modeling of the HBC

The HBC is designed to control the reactive power Q at the PCC and the dc output voltage V_{dc} to regulate the ac and dc output, respectively. Fig. 5.4 shows the overall closed-loop control scheme of the HBC, which includes the outer Q and V_{dc} feedback control loops, the inner current (i_d, i_q) control loop, the phase-locked-loop (PLL) control, and the pulse width modulation (PWM). The outer and inner controllers adopt proportional-integral (PI) controllers and are modeled in the converter reference frame that rotates synchronously with the PCC voltage. The HBC ac-side output voltage (v_d, v_q) are generated from the current orders i_d^* and i_q^* by the decoupled inner current control loop. The value of reference current (i_d^*, i_q^*) are determined by the outer V_{dc} and Q control feedback loops, respectively. Except the inner current control loop is same with that in the section 2.2.2, the remaining modeling details are described as follows.

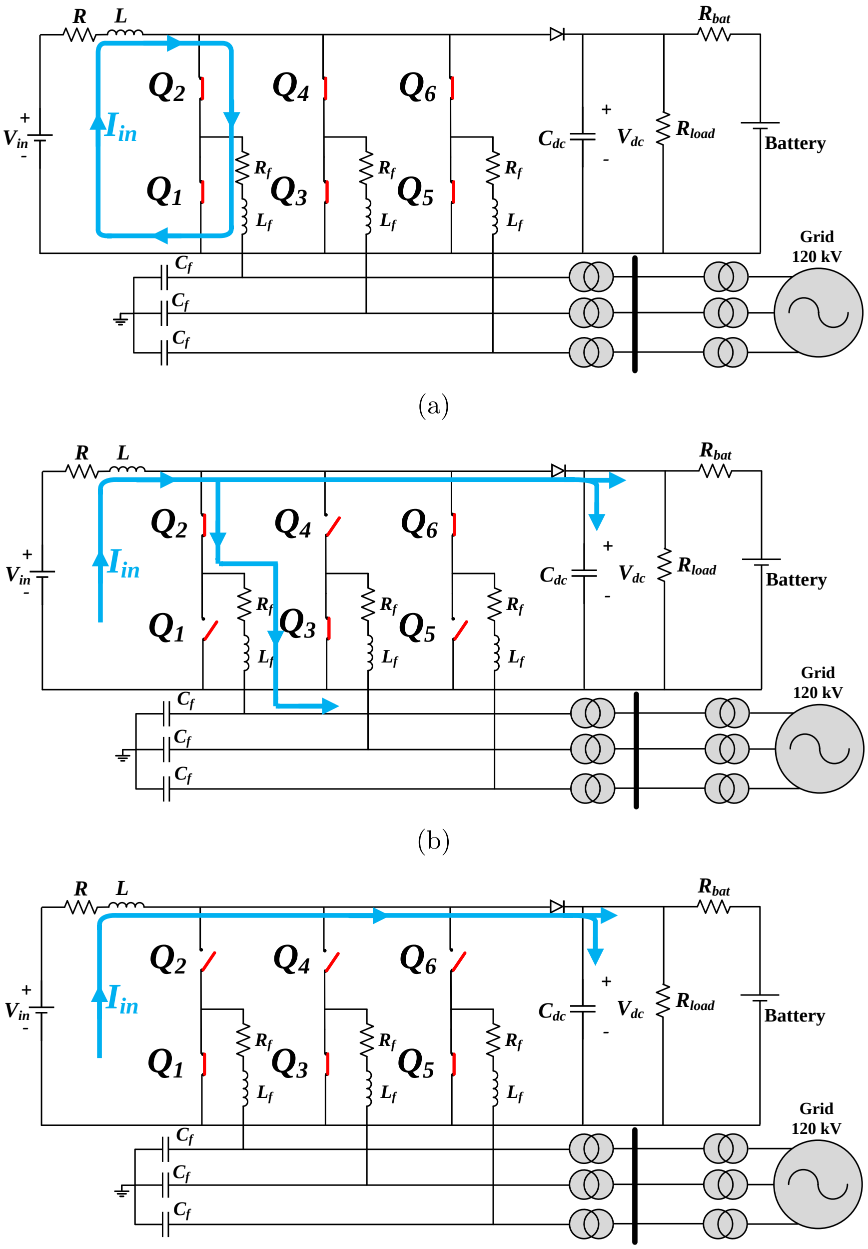

(a)

(b)

(c)

Figure 5.3: Three operating modes of the three-phase HBC: (a) Short through mode, (b) Power mode, (c) Zero mode.

5.3.1 Outer Control Loop

The modeling of outer control loop of the HBC is similar with that in the section 2.2.1. The difference is the output power of the converter include ac and dc power in this research.

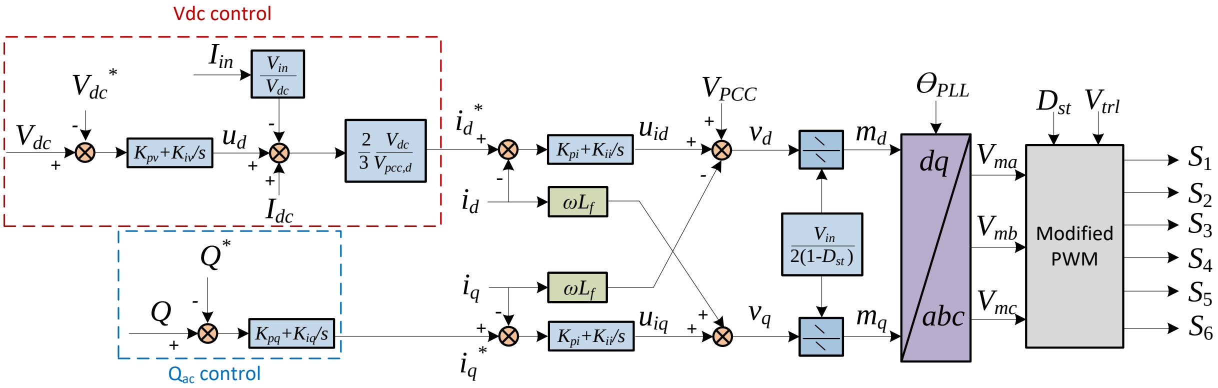

Figure 5.4: Closed-loop control structure for the three-phase HBC.

The energy in the capacitor can be written as

$$\frac{C_{\mathrm{dc}}}{2}\frac{dV_{\mathrm{dc}}^2}{dt} = P_{\mathrm{in}} - P_{\mathrm{ac}} - P_{\mathrm{dc}} \tag{5.4}$$

where P_{in}, P_{ac}, and P_{dc} are the active power at the dc input, ac output, and dc output, respectively. The active and reactive powers flowing into the power grid are expressed as

$$\begin{cases} P_{\mathrm{ac}} &= \frac{3}{2}(v_{\mathrm{pcc,d}}i_{\mathrm{d}} + v_{\mathrm{pcc,q}}i_{\mathrm{q}}) \\ Q_{\mathrm{ac}} &= \frac{3}{2}(v_{\mathrm{pcc,q}}i_{\mathrm{d}} - v_{\mathrm{pcc,d}}i_{\mathrm{q}}) \end{cases} \tag{5.5}$$

With the PLL, the powers can be simplified as $P = \frac{3}{2}V_{\mathrm{pcc}}i_{\mathrm{d}}$ and $Q = -\frac{3}{2}V_{\mathrm{pcc}}i_{\mathrm{q}}$. As a result, (5.4) can be further expressed as follows:

$$\frac{C_{\mathrm{dc}}}{2}\frac{dV_{\mathrm{dc}}^2}{dt} = V_{\mathrm{in}}I_{\mathrm{in}} - \frac{3}{2}V_{\mathrm{pcc}}i_{\mathrm{d}} - V_{\mathrm{dc}}I_{\mathrm{dc}} \tag{5.6}$$

Simplifying the above equation leads to

$$C_{\mathrm{dc}}\frac{dV_{\mathrm{dc}}}{dt} = \underbrace{\frac{V_{\mathrm{in}}}{V_{\mathrm{dc}}}I_{\mathrm{in}} - \frac{3}{2}\frac{V_{\mathrm{pcc}}}{V_{\mathrm{dc}}}i_{\mathrm{d}} - I_{\mathrm{dc}}}_{u_{\mathrm{d}}} \tag{5.7}$$

It is found that the dc output voltage can be controlled by the d-axis current i_d. The PI controller drive the difference between V_{dc}^* and V_{dc} near zero. Based on the u_{d} which is output of PI controller, the current reference i_d^* can be obtained as

$$i_d^* = -\frac{2}{3}\frac{V_{\text{dc}}}{V_{\text{pcc}}}(u_d - \frac{V_{\text{in}}}{V_{\text{dc}}} I_{\text{in}} + I_{\text{dc}}). \tag{5.8}$$

Similarly, the outer reactive power control loop using the same criterion as that for the dc output voltage control loop design. The reactive power exchange between the grid and the HBC is controlled by the q-axis current i_q.

5.3.2 Hybrid PWM Methodology

As discussed in section 5.2, the HBC achieve the dc/dc and dc/ac conversion through three operating modes. The switching scheme based on the operating modes is shown in Fig. 5.5. The carrier triangular signal (V_{trl}) is compared with a dc signal $\pm V_{st}$ and the magnitudes of the phase voltages (v_{ma}, v_{mb}, v_{mc}) to generate gating pulses ($S_1 - S_6$) for regulating dc and ac output, respectively. Fig. 5.6 shows the PWM control strategy to get required switching pattern.

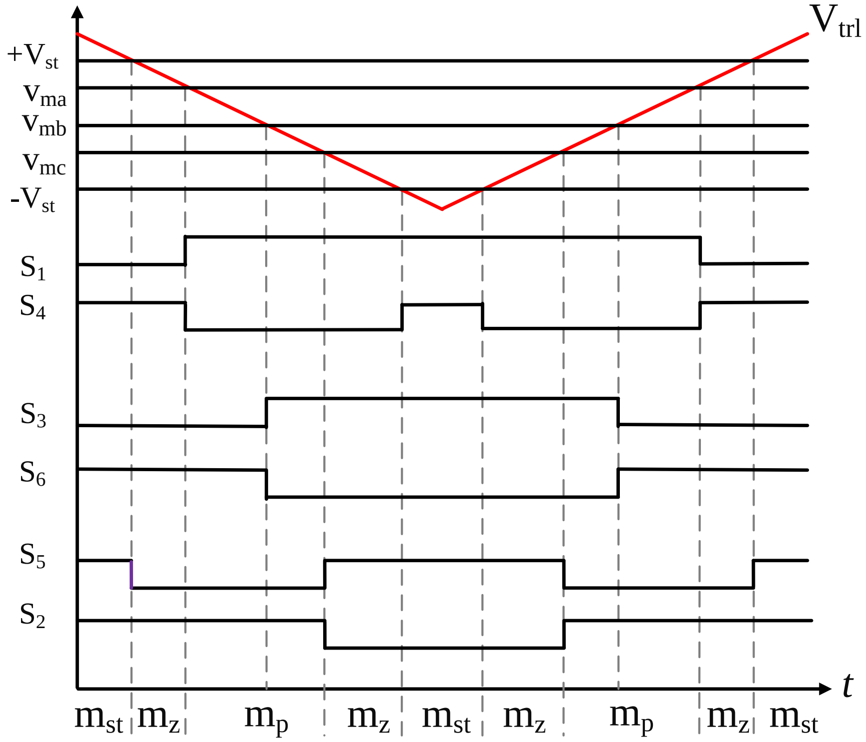

Figure 5.5: Gating pulses for switches ($S_1 - S_6$) and operating waveforms of carrier signal V_{trl}, phase voltages V_m, and dc signal V_{st} for the three-phase HBC.

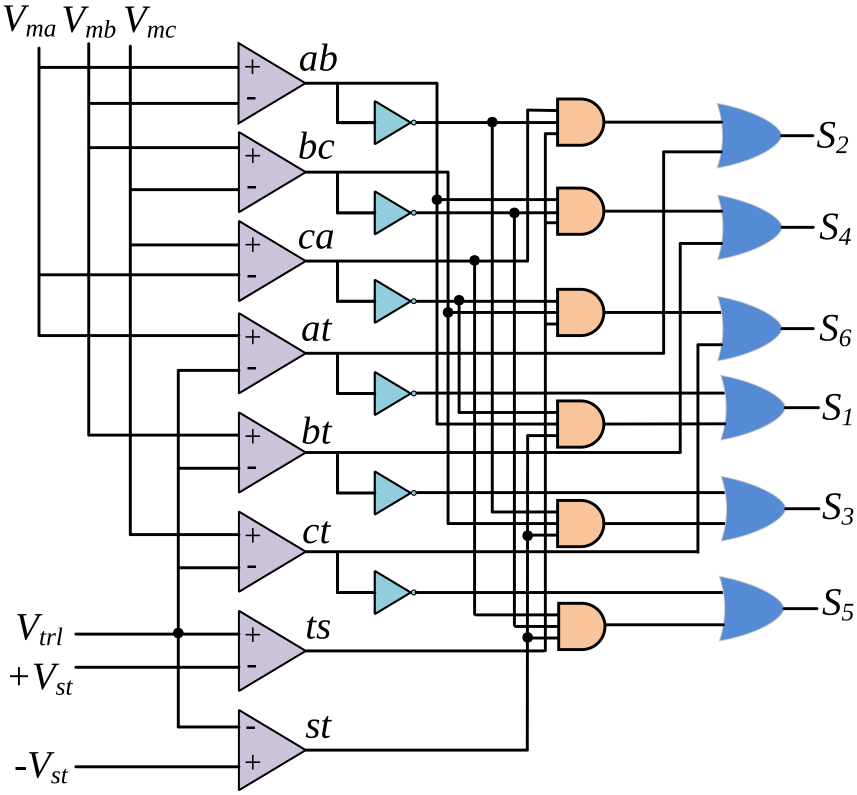

Figure 5.6: PWM control strategy for the three-phase HBC.

5.4 Simulation Results

The HBC can be operated as a rectifier or inverter based on the power exchange between the dc source, dc load, and the utility grid. The utility grid in this case like an energy storage with unlimited storage capacity to balance the load supply and demand. The dc source can either power the dc side and utility grid or cooperate with utility grid to power the dc load. In this research, the latter will be used to test the performance of the bidirectional HBC. In this scenario, the dc source is insufficient to supply the dc load. The utility grid will be acted as a secondary power source to continuously supply the power shortage.

The study system as shown in Fig. 5.2 is established in the MATLAB/Simscape environment. The dc source provides the dc electricity then passes through the HBC to achieve dc output at a different voltage level. At the same time, the electricity from ac grid is rectified to dc electricity to power the power shortage at the dc side. The dc input voltage is always maintained at 200 V. The

Table 5.1: Parameters of the simulation system.

Parameter	Value	Parameter	Value
Rated capacity	100 MVA	DC-side capacitor $\mathrm{C_{dc}}$	12000 uF
System frequency	60 Hz	DC-side voltage $\mathrm{V_{dc}}$	300 V
Input voltage $\mathrm{V_{in}}$	200 V	DC-side load $\mathrm{R_{load}}$	10 Ω
Input resistore R	6.1 Ω	Li-ion battery voltage	230 V
Input inductor L	56 mH	Li-ion battery capacity	5.4 Ah
AC-side voltage base	110 V	Current control $(\mathrm{K_{pi}}, \mathrm{K_{ii}})$	0.63, 10
AC-side resistor $\mathrm{R_f}$	2 mΩ	V_{dc} control $(\mathrm{K_{pv}}, \mathrm{K_{iv}})$	0.3, 0.8
AC-side inductor $\mathrm{L_f}$	125 uH	Q control $(\mathrm{K_{pq}}, \mathrm{K_{iq}})$	0.8, 300
AC-side capacitor $\mathrm{C_f}$	47 uF	PLL $(\mathrm{K_p}, \mathrm{K_i})$	180, 3200
Grid resistor $\mathrm{R_g}$	0.9 Ω	Switching frequency	5 kHz
Grid inductor $\mathrm{L_g}$	16.6 mH		

dc output voltage and reactive power at PCC are controlled as the predetermined reference orders of 300 V and 0, respectively. The parameters of the simulation model are given in the table 5.1.

Fig. 5.7 shows the system dynamic performance of the three-phase HBC in closed-loop condition. The dc output voltage (V_{dc}), reactive power at PCC (Q), duty cycle (D_{st}), modulation index (M_i), power exchange (P), and ac output voltage (V_{ab}) are plotted. The dc load resistance is fixed at 10 Ω and the Li-ion battery will be connected to the system at 2 sec to emulate the increased penetration of dc loads. The events are described as follows:

5.4.1 Reference V_{dc}^* Step Change

At 1 sec, the dc output voltage reference V_{dc}^* step up to 350 V. It is observed that V_{dc} properly follow V_{dc}^*. Meanwhile, D_{st} increase to 0.43 and M_i decrease to 0.54. This satisfies the relation (5.3) to achieve the continuous operation of the HBC. Further, the magnitude of V_{ab} has an increase when the change of D_{st} is greater than that in M_i. This is consistent with principle in equation (5.2), that is, the ac output voltage depends on both D_{st} and M_i. In addition, the power is drawn from the grid to supply dc load. This validates the bidirectional feature of the three-phase HBC.

5.4.2 Reference Q^* Step Change

At 1.5 sec, the ac output reactive power reference Q^* step change from 0 to 10 kVar. Q tracks its reference value correctly and V_{dc} remains at 350 V. This shows the HBC can control dc output voltage and reactive power at PCC independently. Meanwhile, D_{st} remains static but the M_i has a increase which leading to a slight increase of the magnitude of V_{ab}.

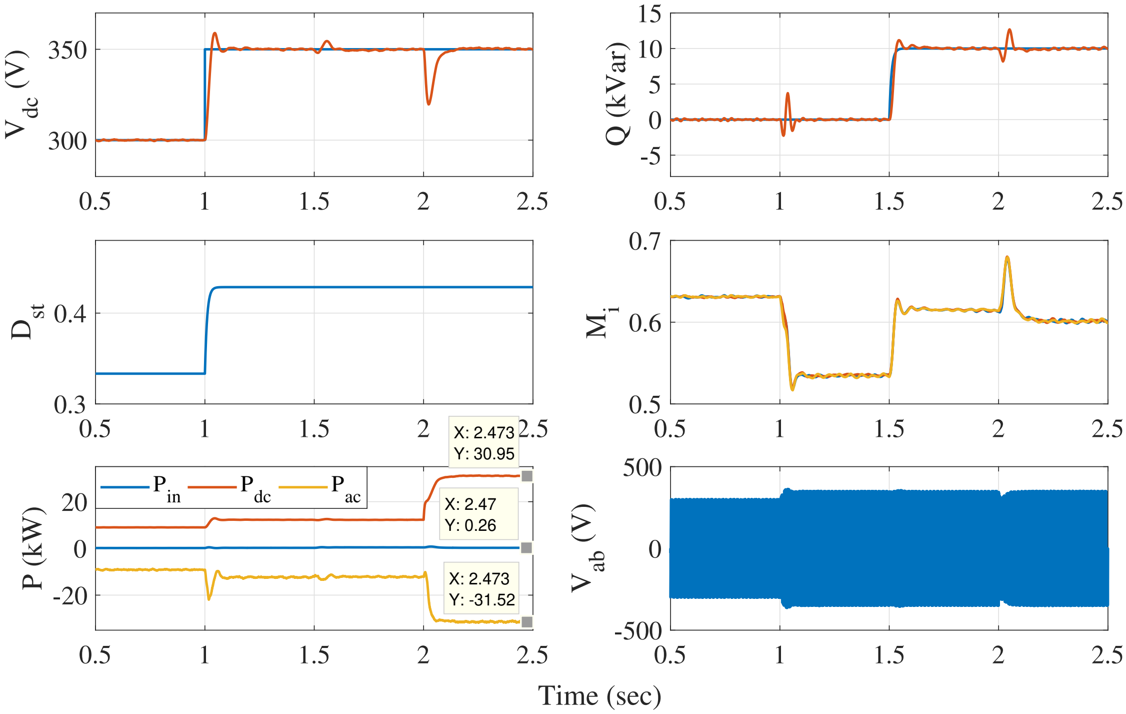

Figure 5.7: Dynamic performance of the three-phase HBC.

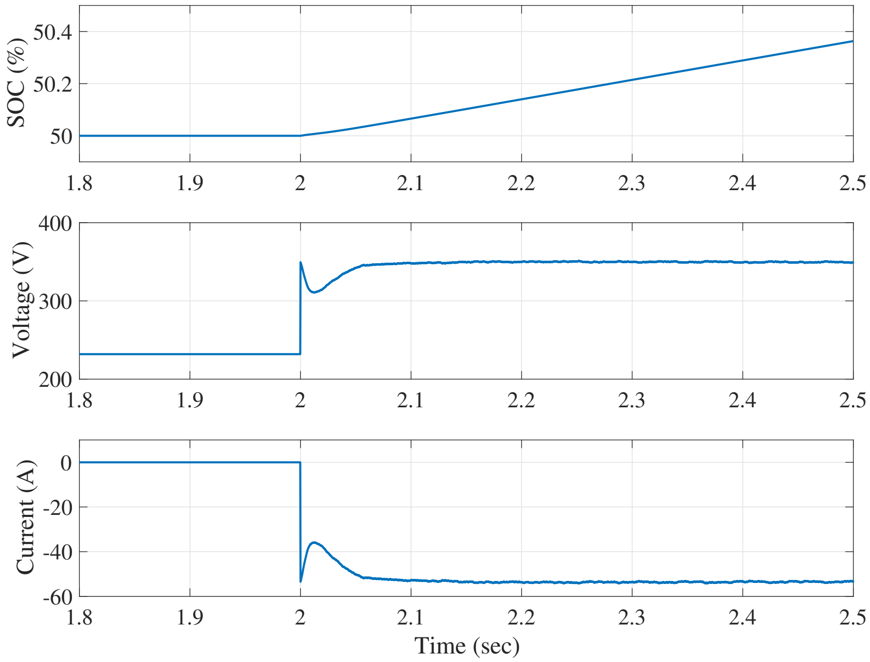

Figure 5.8: Behavior of the battery during the charging.

5.4.3 Battery Charging

At 2 sec, a Li-ion battery is connected to the system. The dc output power increases (P_{dc}= 30.95 kW). After a short transient, the ac grid transfers more power (P_{ac}= 31.52 kW) with the dc input power (P_{in}= 0.26 kW). Meanwhile, it is observed that V_{dc} and Q return to the reference value quickly. The behavior of the battery is shown in Fig. 5.8 that indicates a stable and continuous charging. These results validate the HBC can provide a smooth transition when the dc load has perturbations.

The behavior of three-phase HBC discussed in Section 5.2 has been validated by the time-domain simulation results, that is, the three-phase HBC is able to regulate the dc and ac output while maintaining closed-loop stability.

5.5 Conclusion

This chapter examines the effectiveness and robustness of the HBC with simultaneous ac and dc output when a single dc input is presented. Detailed modeling of the converter in the closed-loop control is developed to demonstrate the operating behavior. The performance is evaluated when the dc input and ac grid maintain continuous dc power supply. The computer simulation results validate that the three-phase HBC is able to correctly regulate the dc and ac output as well as the dc output voltage and the reactive power at PCC.

Chapter 6: Conclusion and Future Work

6.1 Conclusion

The conclusion derived in each chapter will be given as follows:

Chapter 2 presents a detailed characteristics of low inertia IBGs in the power grids. Extensive modeling assumptions and the cascade vector control of grid-following inverter are elaborated to address the challenges of high penetration of the renewable integration.

Chapter 3 presents the modeling and analysis of IBGs in series compensated networks under weak grid conditions. The subsynchronous oscillation (SSO) is thoroughly investigated in type-4 wind farm using the large and small signal analysis. This chapter provide a comprehensive scope of work that investigates two major types of type-4 wind turbines for grid integration into series compensated networks. A rigorous study approach is addressed that analytical results based on simplified models are validated by simulation results based on EMT models with full details. Furthermore, this chapter introduces a powerful modeling frame with the capability of not only well-known eigenvalue analysis, participation factor analysis but also impedance-based frequency-domain stability analysis. The major contribution is an insightful finding of potential stability issues in series compensated grids with high penetration of type-4 wind power. The analysis results find that instability is caused by the interaction of LC resonance mode associated to series compensation level and a weak grid mode associated to voltage-source converter (VSC) control parameters, including phase-locked-loop (PLL) bandwidth. Higher PLL bandwidth may make the weak grid mode lose stability. In noncompensated networks, the weak grid mode moves to the left half plane (more stable) when grid strength increases. On the contrary, when grid strength is increased with increasing the series compensation degree in series compensated network, the weak grid mode moves to the right half plane (more unstable).

Chapter 4 presents the admittance identification of IBGs for stability prediction. The impedance modeling of type-3 or type-4 wind farms are introduced to investigate the SSO. The positive-sequence scalar admittance can be used to assess SSO for type-3 wind farms. However, it is known that positive-sequence admittance has limitations for stability analysis of type-4 wind because of significant frequency-coupling effect. Sequence-domain or dq-domain admittance is capable to provide accurate analysis results for type-4 wind farm. Three methods to find admittance matrices are presented: frequency scan in the static frame and *dq*-frame, and time domain data-based identification in the *dq*-frame. The first method leads to sequence-domain admittance, which can be further converted to a *dq*-domain admittance. The latter two lead to *dq*-domain admittances. The resulting *dq*-domain admittance measurements are compared for consistency. This chapter provides the theoretic derivation to sheds insights on frequency coupling effect on the static *abc*-frame variables, and provides a clear guidance of sequence-domain admittance measuring procedure. Furthermore, a stability analysis approach, *s*-domain admittance model-based eigenvalue analysis, is presented to demonstrate the effectiveness of stability prediction.

Chapter 5 presents a single-stage multi-port hybrid boost converter (HBC) to supply dc load and ac load simultaneously in grid connected IBGs. The goal of the proposed HBC is reducing the conversion process to a minimum to achieve a more efficient architecture of DC-based power system compared to the conventional structure which includes dc/dc and dc/ac conversions. The critical aspects of the operation of the HBC, including the grid-following control strategy and hybrid pulse width modulation methodology, is presented. It is validated that the HBC has capability of maintaining the smooth power flow between the ac and dc outputs, correctly regulating the dc bus voltage while maintaining closed-loop stability.

6.2 Future Work

The future work of this dissertation can contain the following parts.

First, although the performance of HBC is validated using computer simulation in chapter 5, it can be further validated through the experimental simulation using a NI sbRIO General Purpose Inverter Controller (GPIC) board. The control schematic described in Section 5.3 will be employed in the Labview field programmable gate array (FPGA) using a host computer. The gating pulses then send to National instruments (NI) 9683 sbRIO General Purpose Inverter Controller (GPIC) to drive the switches. The real-time measurements of ac and dc output voltage/currents are obtained through the sensors in GPIC board. The capability of regulating the dc and ac output while maintain the closed-loop stability can be investigated. Furthermore, a high step-up dc voltage is expected to observe.

Second, this dissertation only studies a single IBG equivalent connected to the power grid. However, if a more comprehensive power system including multiple IBGs (e.g., wind, solar, and energy storage) is presented, the dynamics will be different from that impacted by a single IBG. In this case, the impact of these IBGs on the stability and dynamic performance will be explored.

Last, a microgrid includes IBGs operated in the grid-following (GFL) and grid-forming (GFM) control can be investigated. This dissertation only investigate the prevalent GFL control which has fast response to any event. However, GFL merely regulates its grid angle and frequency output. On the contrary, the droop inverter deployed with GFM control actively control its voltage and frequency output. Combining with the integration of Battery Energy Storage System (BESS), GFM has capability to provide a broad scope of the grid support services to enhance the reliability of the system. This topic still needs intensive research effort.

References

[1] K. O. S. Lindenberg, B. Smith and E. DeMeo, "20 Percent Wind Energy by 2030: Increasing Wind Energy's Contribution to U.S. Electricity Supply," https://www.nrel.gov/docs/fy08osti/41869.pdf, 2008, [Online; U.S. Department of Energy].

[2] NREL, "SunShot 2030 for Photovoltaics (PV): Envisioning a Low-cost PV Future," https://www.nrel.gov/docs/fy17osti/68105.pdf, 2017, [Online].

[3] I. W. Group *et al.*, "Ieee guide for planning dc links terminating at ac locations having low short-circuit capacities," 1997.

[4] S.-H. Huang, J. Schmall, J. Conto, J. Adams, Y. Zhang, and C. Carter, "Voltage control challenges on weak grids with high penetration of wind generation: Ercot experience," in *Power and Energy Society General Meeting, 2012 IEEE.* IEEE, 2012, pp. 1–7.

[5] A. Dissanayaka and A. Isaacs, "System Strength Assessment of the Panhandle System PSCAD Study," http://www.ercot.com/content/news/presentations/2016/Panhandle%20System%20Strength%20Study%20Feb%2023%202016%20(Public).pdf, 2016, [Online].

[6] H. Liu, X. Xie, J. He, T. Xu, Z. Yu, C. Wang, and C. Zhang, "Subsynchronous interaction between direct-drive pmsg based wind farms and weak ac networks," *IEEE Transactions on Power Systems*, vol. 32, no. 6, pp. 4708–4720, 2017.

[7] L. Fan, Z. Miao, and M. Zhang, "Subcycle overvoltage dynamics in solar pvs," *IEEE Transactions on Power Delivery*, vol. 36, no. 3, pp. 1847–1858, 2021.

[8] M. Zhang, Z. Miao, and L. Fan, "Reduced-order analytical model of grid-connected solar photovoltaic system for low-frequency oscillation analysis," *IEEE Transactions on Sustainable Energy*, 2021.

[9] N. G. ESO, "Technical Report on the events of 9 August 2019," https://www.nationalgrideso.com/document/152346/download, 2019, [Online].

[10] NERC, "April and May 2018 Fault Induced Solar Photovoltaic Resource Interruption Disturbances Report," https://www.nerc.com/pa/rrm/ea/Pages/April-May-2018-Fault-Induced-Solar-PV-Resource-Interruption-Disturbances-Report.aspx, 2019, [Online].

[11] K. Narendra, D. Fedirchuk, R. Midence, N. Zhang, A. Mulawarman, P. Mysore, and V. Sood, "New microprocessor based relay to monitor and protect power systems against sub-harmonics," in *2011 IEEE Electrical Power and Energy Conference.* IEEE, 2011, pp. 438–443.

[12] X. Xie, X. Zhang, H. Liu, H. Liu, Y. Li, and C. Zhang, "Characteristic analysis of subsynchronous resonance in practical wind farms connected to series-compensated transmissions," *IEEE Transactions on Energy Conversion*, vol. 32, no. 3, pp. 1117–1126, 2017.

[13] J. Adams, C. Carter, and S.-H. Huang, "Ercot experience with sub-synchronous control interaction and proposed remediation," in *Transmission and Distribution Conference and Exposition (T&D), 2012 IEEE PES*. IEEE, 2012, pp. 1–5.

[14] S. Huang and Y. Gong, "South Texas SSR," http://www.ercot.com/content/wcm/key_documents_lists/139265/10._South_Texas_SSR_ERCOT_ROS_May_2018_rev1.pdf, May 2018.

[15] H. Ma, P. Brogan, K. Jensen, and R. Nelson, "Sub-synchronous control interaction studies between full-converter wind turbines and series-compensated ac transmission lines," in *Power and Energy Society General Meeting, 2012 IEEE*. IEEE, 2012, pp. 1–5.

[16] M. Beza and M. Bongiorno, "On the risk for subsynchronous control interaction in type 4 based wind farms," *IEEE Transactions on Sustainable Energy*, vol. 10, no. 3, pp. 1410–1418, 2018.

[17] "Ieee pes task force report: Modeling subsynchronous oscillations in wind energy interconnected systems, author=WindSSO Taskforce."

[18] J. Sun, "Impedance-based stability criterion for grid-connected inverters," *IEEE Transactions on Power Electronics*, vol. 26, no. 11, pp. 3075–3078, 2011.

[19] L. Fan and Z. Miao, "Nyquist-stability-criterion-based ssr explanation for type-3 wind generators," *IEEE Transactions on Energy Conversion*, vol. 27, no. 3, pp. 807–809, 2012.

[20] M. Cespedes and J. Sun, "Three-phase impedance measurement for system stability analysis," in *2013 IEEE 14th Workshop on Control and Modeling for Power Electronics (COMPEL)*. IEEE, 2013, pp. 1–6.

[21] B. Badrzadeh, M. Sahni, Y. Zhou, D. Muthumuni, and A. Gole, "General methodology for analysis of sub-synchronous interaction in wind power plants," *IEEE Transactions on Power Systems*, vol. 28, no. 2, pp. 1858–1869, 2012.

[22] J. Huang, K. A. Corzine, and M. Belkhayat, "Small-signal impedance measurement of power-electronics-based ac power systems using line-to-line current injection," *IEEE Transactions on Power Electronics*, vol. 24, no. 2, pp. 445–455, 2009.

[23] Y. A. Familiant, J. Huang, K. A. Corzine, and M. Belkhayat, "New techniques for measuring impedance characteristics of three-phase ac power systems," *IEEE Transactions on Power Electronics*, vol. 24, no. 7, pp. 1802–1810, 2009.

[24] M. K. Bakhshizadeh, X. Wang, F. Blaabjerg, J. Hjerrild, Ł. Kocewiak, C. L. Bak, and B. Hesselbæk, "Couplings in phase domain impedance modeling of grid-connected converters," *IEEE Transactions on Power Electronics*, vol. 31, no. 10, pp. 6792–6796, 2016.

[25] A. S. Trevisan, Â. Mendonça, R. Gagnon, J. Mahseredjian, and M. Fecteau, "Analytically validated ssci assessment technique for wind parks in series compensated grids," *IEEE Transactions on Power Systems*, vol. 36, no. 1, pp. 39–48, 2020.

[26] A. Rygg, M. Molinas, C. Zhang, and X. Cai, "A modified sequence-domain impedance definition and its equivalence to the dq-domain impedance definition for the stability analysis of ac power electronic systems," *IEEE Journal of Emerging and Selected Topics in Power Electronics*, vol. 4, no. 4, pp. 1383–1396, 2016.

[27] S. Shah and L. Parsa, "Impedance modeling of three-phase voltage source converters in dq, sequence, and phasor domains," *IEEE Transactions on Energy Conversion*, vol. 32, no. 3, pp. 1139–1150, 2017.

[28] S. D. Shah, P. J. Koralewicz, R. B. Wallen, and V. Gevorgian, "Impedance characterization of utility-scale renewable energy and storage systems," National Renewable Energy Lab.(NREL), Golden, CO (United States), Tech. Rep., 2019.

[29] B. Gustavsen and A. Semlyen, "Rational approximation of frequency domain responses by vector fitting," *IEEE Transactions on power delivery*, vol. 14, no. 3, pp. 1052–1061, 1999.

[30] L. Fan and Z. Miao, "A modular small-signal analysis framework for inverter penetrated power grids: Measurement, assembling, aggregation, and stability assessment," *arXiv preprint arXiv:2003.03860*, 2020.

[31] L. Fan, "Admittance-based stability analysis: Bode plots, nyquist diagrams or eigenvalue analysis?" *IEEE Transactions on Power Systems*, vol. 35, no. 4, pp. 3312–3315, 2020.

[32] L. Fan, R. Kavasseri, Z. L. Miao, and C. Zhu, "Modeling of dfig-based wind farms for ssr analysis," *IEEE Transactions on Power Delivery*, vol. 25, no. 4, pp. 2073–2082, 2010.

[33] L. Fan, "Modeling type-4 wind in weak grids," *IEEE Transactions on Sustainable Energy*, vol. 10, no. 2, pp. 853–864, April 2019.

[34] Z. Miao, "Impedance-model-based ssr analysis for type 3 wind generator and series-compensated network," *IEEE Transactions on Energy Conversion*, vol. 27, no. 4, pp. 984–991, 2012.

[35] J. Sun, Z. Bing, and K. J. Karimi, "Input impedance modeling of multipulse rectifiers by harmonic linearization," *IEEE Transactions on Power Electronics*, vol. 24, no. 12, pp. 2812–2820, 2009.

[36] M. Cespedes and J. Sun, "Impedance modeling and analysis of grid-connected voltage-source converters," *IEEE Transactions on Power Electronics*, vol. 29, no. 3, pp. 1254–1261, 2014.

[37] M. Amin and M. Molinas, "Small-signal stability assessment of power electronics based power systems: A discussion of impedance- and eigenvalue-based methods," *IEEE Transactions on Industry Applications*, vol. 53, no. 5, pp. 5014–5030, Sep. 2017.

[38] R. H. Park, "Two-reaction theory of synchronous machines generalized method of analysis-part i," *Transactions of the American Institute of Electrical Engineers*, vol. 48, no. 3, pp. 716–727, 1929.

[39] J. Undrill and T. Kostyniak, "Subsynchronous oscillations part 1 comprehensive system stability analysis," *IEEE Transactions on Power apparatus and Systems*, vol. 95, no. 4, pp. 1446–1455, 1976.

[40] S. Kouro, J. I. Leon, D. Vinnikov, and L. G. Franquelo, “Grid-connected photovoltaic systems: An overview of recent research and emerging pv converter technology,” *IEEE Industrial Electronics Magazine*, vol. 9, no. 1, pp. 47–61, 2015.

[41] O. Abdel-Rahim, M. Orabi, E. Abdelkarim, M. Ahmed, and M. Z. Youssef, “Switched inductor boost converter for pv applications,” in *2012 Twenty-Seventh Annual IEEE Applied Power Electronics Conference and Exposition (APEC)*. IEEE, 2012, pp. 2100–2106.

[42] P. Shukl and B. Singh, “Delta-bar-delta neural-network-based control approach for power quality improvement of solar-pv-interfaced distribution system,” *IEEE Transactions on Industrial Informatics*, vol. 16, no. 2, pp. 790–801, 2019.

[43] P. Mishra, A. K. Pradhan, and P. Bajpai, “Adaptive distance relaying for distribution lines connecting inverter-interfaced solar pv plant,” *IEEE Transactions on Industrial Electronics*, vol. 68, no. 3, pp. 2300–2309, 2020.

[44] A. K. Singh, S. Kumar, and B. Singh, “Solar pv energy generation system interfaced to three phase grid with improved power quality,” *IEEE Transactions on Industrial Electronics*, vol. 67, no. 5, pp. 3798–3808, 2019.

[45] A. Alzahrani, “A hybrid dc–dc quadrupler boost converter for photovoltaic panels integration into a dc distribution system,” *Electronics*, vol. 9, no. 11, p. 1965, 2020.

[46] O. Ray and S. Mishra, “Boost-derived hybrid converter with simultaneous dc and ac outputs,” *IEEE transactions on Industry applications*, vol. 50, no. 2, pp. 1082–1093, 2013.

[47] O. Ray, V. Dharmarajan, S. Mishra, R. Adda, and P. Enjeti, “Analysis and pwm control of three-phase boost-derived hybrid converter,” in *2014 IEEE Energy Conversion Congress and Exposition (ECCE)*. IEEE, 2014, pp. 402–408.

[48] O. Ray and S. Mishra, “Integrated hybrid output converter as power router for renewable-based nanogrids,” in *IECON 2015-41st Annual Conference of the IEEE Industrial Electronics Society*. IEEE, 2015, pp. 001 645–001 650.

[49] CIGRE and C. joint working groups. (2018) Modeling of inverter-based generator for power system dynamic studies. [Online]. Available: http://cired.net/uploads/default/files/727-web.pdf

[50] V. Akhmatov, “Analysis of dynamic behavior of electric power systems with large amount of wind power,” *Electrical Power Engineering*, 2003.

[51] L. M. Fernández, F. Jurado, and J. R. Saenz, “Aggregated dynamic model for wind farms with doubly fed induction generator wind turbines,” *Renewable energy*, vol. 33, no. 1, pp. 129–140, 2008.

[52] E. Muljadi and B. Parsons, “Comparing single and multiple turbine representations in a wind farm simulation: Preprint,” National Renewable Energy Laboratory (NREL), Golden, CO., Tech. Rep., 2006.

[53] M. Pyller and S. Achilles, “Aggregated wind park models for analyzing power system dynamics,” 2003.

[54] R. E. Torres-Olguin, M. Molinas, and T. Undeland, “Offshore wind farm grid integration by vsc technology with lcc-based hvdc transmission,” *IEEE Transactions on Sustainable Energy*, vol. 3, no. 4, pp. 899–907, 2012.

[55] Y. Li, L. Fan, and Z. Miao, “Wind in weak grids: Low-frequency oscillations, subsynchronous oscillations, and torsional interactions,” *IEEE Transactions on Power Systems*, vol. 35, no. 1, pp. 109–118, 2020.

[56] L. Piyasinghe, Z. Miao, J. Khazaei, and L. Fan, “Impedance model-based ssr analysis for tcsc compensated type-3 wind energy delivery systems,” *IEEE Transactions on Sustainable Energy*, vol. 6, no. 1, pp. 179–187, 2015.

[57] A. E. Leon and J. A. Solsona, “Sub-synchronous interaction damping control for dfig wind turbines,” *IEEE Transactions on Power Systems*, vol. 30, no. 1, pp. 419–428, 2015.

[58] M. S. El-Moursi, B. Bak-Jensen, and M. H. Abdel-Rahman, “Novel statcom controller for mitigating ssr and damping power system oscillations in a series compensated wind park,” *IEEE Transactions on Power Electronics*, vol. 25, no. 2, pp. 429–441, 2010.

[59] H. A. Mohammadpour and E. Santi, “Ssr damping controller design and optimal placement in rotor-side and grid-side converters of series-compensated dfig-based wind farm,” *IEEE Transactions on Sustainable Energy*, vol. 6, no. 2, pp. 388–399, 2015.

[60] “First benchmark model for computer simulation of subsynchronous resonance,” *IEEE Transactions on Power Apparatus and Systems*, vol. 96, no. 5, pp. 1565–1572, 1977.

[61] H. Zhang, L. Harnefors, X. Wang, H. Gong, and J. Hasler, “Stability analysis of grid-connected voltage-source converters using siso modeling,” *IEEE Transactions on Power Electronics*, vol. 34, no. 8, pp. 8104–8117, 2019.

[62] M. G. Taul, X. Wang, P. Davari, and F. Blaabjerg, “An overview of assessment methods for synchronization stability of grid-connected converters under severe symmetrical grid faults,” *IEEE Transactions on Power Electronics*, vol. 34, no. 10, pp. 9655–9670, 2019.

[63] Y. Huang, X. Yuan, J. Hu, and P. Zhou, “Modeling of vsc connected to weak grid for stability analysis of dc-link voltage control,” *IEEE Journal of Emerging and Selected Topics in Power Electronics*, vol. 3, no. 4, pp. 1193–1204, 2015.

[64] S. Cuk and R. Middlebrook, “A general unified approach to modelling switching dc-to-dc converters in discontinuous conduction mode,” in *1977 IEEE Power Electronics Specialists Conference*. IEEE, 1977, pp. 36–57.

[65] Y. Zhou, D. Nguyen, P. Kjaer, and S. Saylors, “Connecting wind power plant with weak grid-challenges and solutions,” in *Power and Energy Society General Meeting (PES), 2013 IEEE*. IEEE, 2013, pp. 1–7.

[66] N. P. Strachan and D. Jovcic, “Stability of a variable-speed permanent magnet wind generator with weak ac grids,” *IEEE Transactions on Power Delivery*, vol. 25, no. 4, pp. 2779–2788, 2010.

[67] B. Wu, Y. Lang, N. Zargari, and S. Kouro, *Power conversion and control of wind energy systems.* John Wiley & Sons, 2011, vol. 76.

[68] X. Yuan, F. Wang, D. Boroyevich, Y. Li, and R. Burgos, “Dc-link voltage control of a full power converter for wind generator operating in weak-grid systems,” *IEEE Transactions on Power Electronics*, vol. 24, no. 9, pp. 2178–2192, Sept 2009.

[69] K. Liao and Y. Wang, “A comparison between voltage and reactive power feedback schemes of dfigs for inter-area oscillation damping control,” *Energies*, vol. 10, no. 8, p. 1206, 2017.

[70] J. H. Chow, F. F. Wu, and J. A. Momoh, “Applied mathematics for restructured electric power systems,” in *Applied mathematics for restructured electric power systems.* Springer, 2005, pp. 1–9.

[71] K. M. Alawasa, Y. A.-R. I. Mohamed, and W. Xu, “Modeling, analysis, and suppression of the impact of full-scale wind-power converters on subsynchronous damping,” *IEEE Systems Journal*, vol. 7, no. 4, pp. 700–712, 2013.

[72] Y. Xu, M. Zhang, L. Fan, and Z. Miao, “Small-signal stability analysis of type-4 wind in series compensated networks,” *IEEE Transactions on Energy Conversion*, 2019.

[73] (2018, Dec) Type-4 Wind Turbine Model. [Online]. Available: https://hvdc.ca/uploads/knowledge_base/type_4_wind_turbine_model_v46.pdf?t=1544110359

[74] J. Khazaei, Z. Miao, L. Piyasinghe, and L. Fan, “Initialization of unbalanced radial distribution systems for small signal stability analysis,” in *2015 IEEE Power & Energy Society General Meeting.* IEEE, 2015, pp. 1–5.

[75] A. R. Bergen, *Power systems analysis.* Pearson Education India, 2009.

[76] L. Harnefors, M. Bongiorno, and S. Lundberg, “Input-admittance calculation and shaping for controlled voltage-source converters,” *IEEE transactions on industrial electronics*, vol. 54, no. 6, pp. 3323–3334, 2007.

[77] X. Wang, L. Harnefors, and F. Blaabjerg, “Unified impedance model of grid-connected voltage-source converters,” *IEEE Transactions on Power Electronics*, vol. 33, no. 2, pp. 1775–1787, 2017.

[78] H. Liu and X. Xie, “Comparative studies on the impedance models of vsc-based renewable generators for ssi stability analysis,” *IEEE Transactions on Energy Conversion*, vol. 34, no. 3, pp. 1442–1453, Sep. 2019.

[79] K. M. Alawasa, Y. A.-R. I. Mohamed, and W. Xu, “Active mitigation of subsynchronous interactions between pwm voltage-source converters and power networks,” *IEEE Transactions on Power Electronics*, vol. 29, no. 1, pp. 121–134, 2013.

[80] L. Piyasinghe, Z. Miao, J. Khazaei, and L. Fan, “Impedance model-based ssr analysis for tcsc compensated type-3 wind energy delivery systems,” *IEEE Transactions on Sustainable Energy*, vol. 6, no. 1, pp. 179–187, 2014.

[81] C. Desoer and Y.-T. Wang, “On the generalized nyquist stability criterion,” *IEEE Transactions on Automatic Control*, vol. 25, no. 2, pp. 187–196, 1980.

[82] A. Nakhmani, M. Lichtsinder, and E. Zeheb, “Generalized nyquist criterion and generalized bode diagram for analysis and synthesis of uncertain control systems,” in *2006 IEEE 24th Convention of Electrical & Electronics Engineers in Israel.* IEEE, 2006, pp. 250–254.

[83] D. Lumbreras Magallón, R. Barrios, A. Urtasun Erburu, A. Ursúa Rubio, L. Marroyo Palomo, P. Sanchís Gúrpide *et al.*, “On the stability of advanced power electronic converters: the generalized bode criterion,” *IEEE Transactions on Power Electronics, vol. 34, no. 9, September 2019*, 2019.

[84] Y. Xu and Z. Miao, “Wind farm admittance identification for eigenvalue analysis,” *Under review, Electric Power Systems Research*, 2021.

[85] T. Roinila, T. Messo, and E. Santi, “Mimo-identification techniques for rapid impedance-based stability assessment of three-phase systems in dq domain,” *IEEE Transactions on Power Electronics*, vol. 33, no. 5, pp. 4015–4022, 2017.

[86] M. Jakšić, Z. Shen, I. Cvetković, D. Boroyevich, R. Burgos, C. DiMarino, and F. Chen, “Medium-voltage impedance measurement unit for assessing the system stability of electric ships,” *IEEE Transactions on Energy Conversion*, vol. 32, no. 2, pp. 829–841, 2017.

[87] L. Fan and Z. Miao, “Admittance-based stability analysis: Bode plots, nyquist diagrams or eigenvalue analysis?” *IEEE Transactions on Power Systems*, vol. 35, no. 4, pp. 3312–3315, 2020.

[88] P. Wang, L. Goel, X. Liu, and F. H. Choo, “Harmonizing ac and dc: A hybrid ac/dc future grid solution,” *IEEE Power and Energy Magazine*, vol. 11, no. 3, pp. 76–83, 2013.

[89] P. Wang, X. Liu, C. Jin, P. Loh, and F. Choo, “A hybrid ac/dc micro-grid architecture, operation and control,” in *2011 IEEE Power and Energy Society General Meeting*, 2011, pp. 1–8.

[90] O. Ray and S. Mishra, “Integrated hybrid output converter as power router for renewable-based nanogrids,” in *IECON 2015 - 41st Annual Conference of the IEEE Industrial Electronics Society*, 2015, pp. 001 645–001 650.

Appendix A: Reuse Permissions of Published Papers

The permission below is for Figure 1.1.

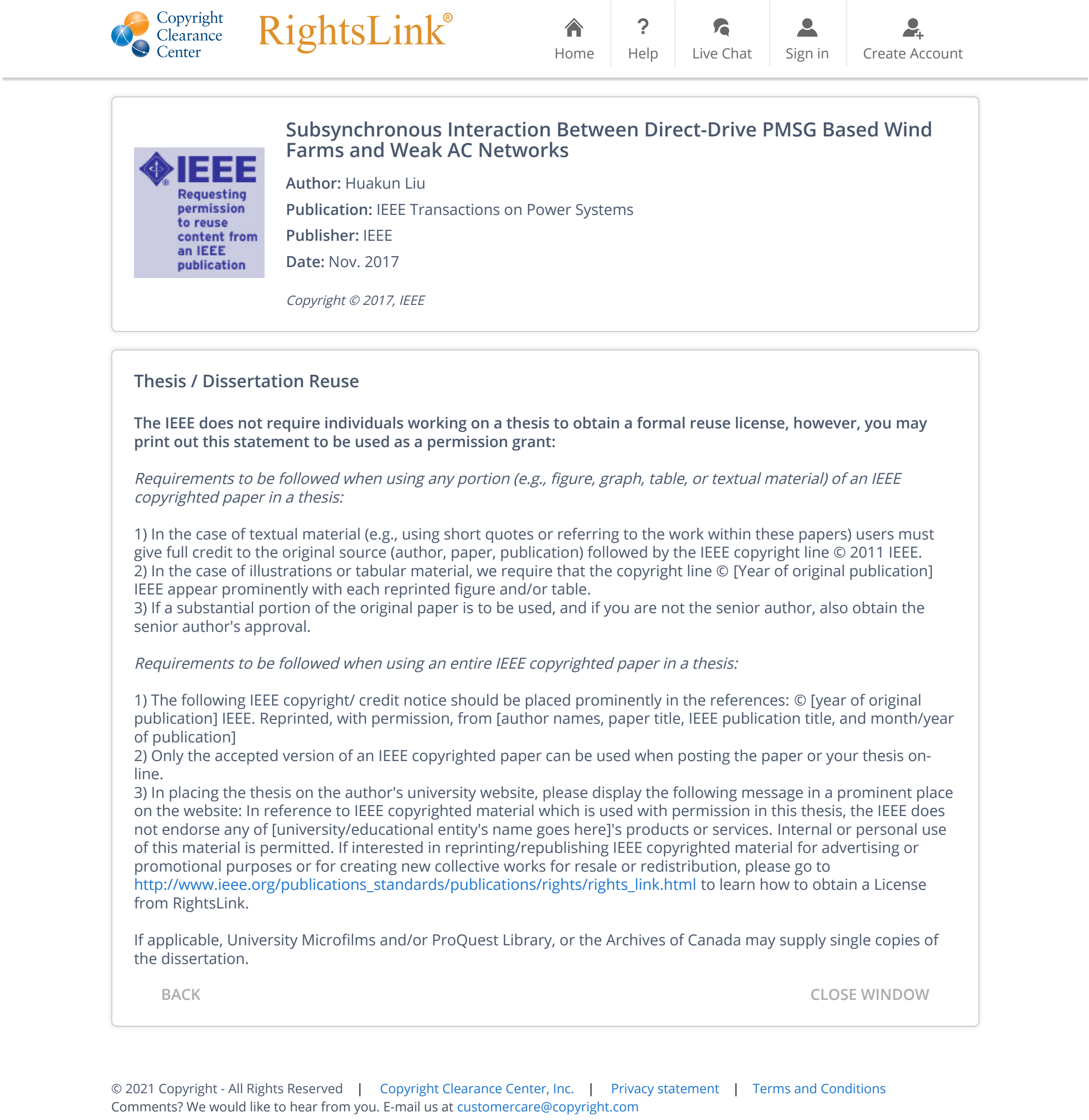

Subsynchronous Interaction Between Direct-Drive PMSG Based Wind Farms and Weak AC Networks

Author: Huakun Liu

Publication: IEEE Transactions on Power Systems

Publisher: IEEE

Date: Nov. 2017

Copyright © 2017, IEEE

Thesis / Dissertation Reuse

The IEEE does not require individuals working on a thesis to obtain a formal reuse license, however, you may print out this statement to be used as a permission grant:

Requirements to be followed when using any portion (e.g., figure, graph, table, or textual material) of an IEEE copyrighted paper in a thesis:

1) In the case of textual material (e.g., using short quotes or referring to the work within these papers) users must give full credit to the original source (author, paper, publication) followed by the IEEE copyright line © 2011 IEEE.
2) In the case of illustrations or tabular material, we require that the copyright line © [Year of original publication] IEEE appear prominently with each reprinted figure and/or table.
3) If a substantial portion of the original paper is to be used, and if you are not the senior author, also obtain the senior author's approval.

Requirements to be followed when using an entire IEEE copyrighted paper in a thesis:

1) The following IEEE copyright/ credit notice should be placed prominently in the references: © [year of original publication] IEEE. Reprinted, with permission, from [author names, paper title, IEEE publication title, and month/year of publication]
2) Only the accepted version of an IEEE copyrighted paper can be used when posting the paper or your thesis on-line.
3) In placing the thesis on the author's university website, please display the following message in a prominent place on the website: In reference to IEEE copyrighted material which is used with permission in this thesis, the IEEE does not endorse any of [university/educational entity's name goes here]'s products or services. Internal or personal use of this material is permitted. If interested in reprinting/republishing IEEE copyrighted material for advertising or promotional purposes or for creating new collective works for resale or redistribution, please go to http://www.ieee.org/publications_standards/publications/rights/rights_link.html to learn how to obtain a License from RightsLink.

If applicable, University Microfilms and/or ProQuest Library, or the Archives of Canada may supply single copies of the dissertation.

© 2021 Copyright - All Rights Reserved | Copyright Clearance Center, Inc. | Privacy statement | Terms and Conditions
Comments? We would like to hear from you. E-mail us at customercare@copyright.com

The permission below is for Figure 1.2.

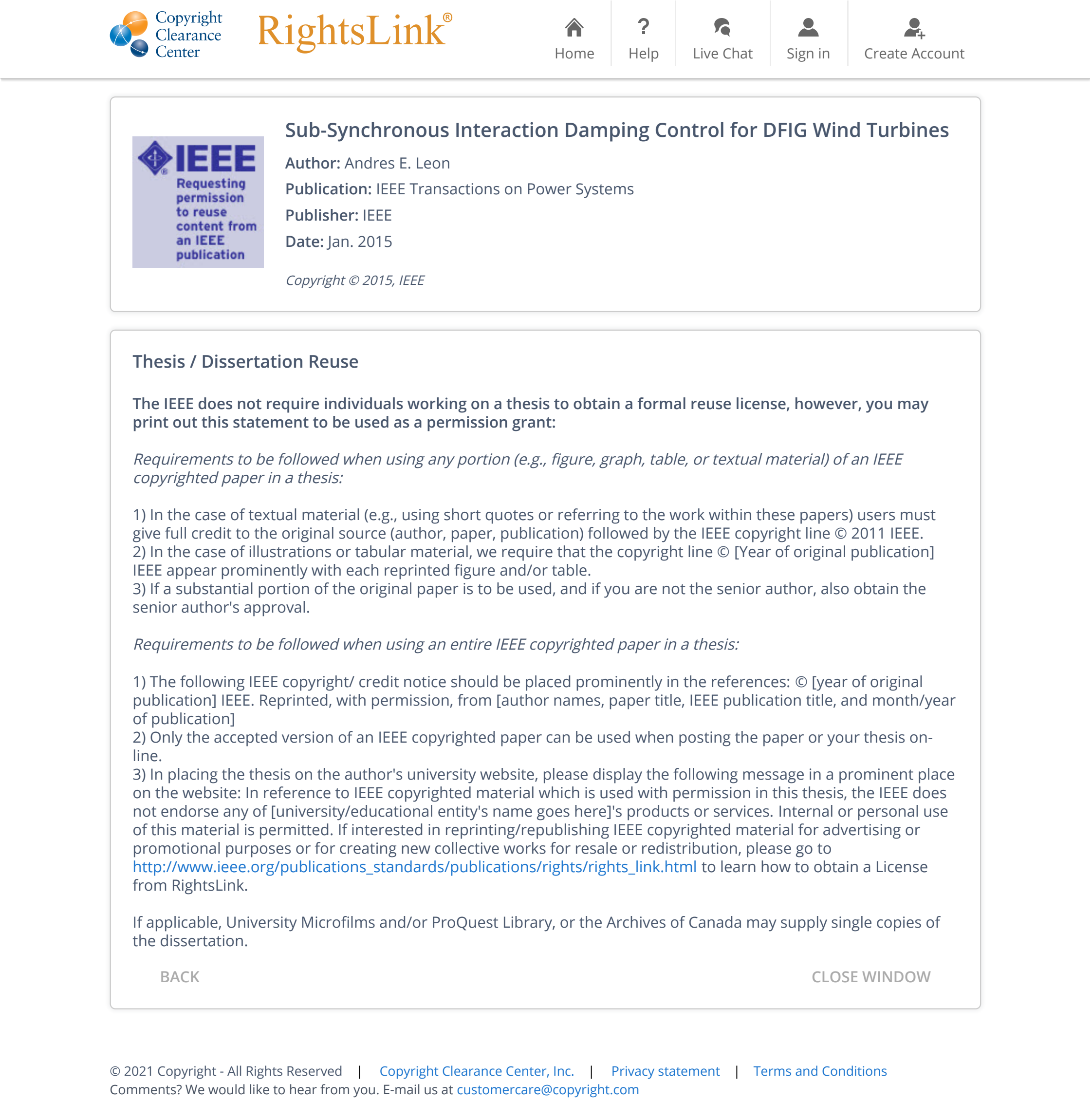

Sub-Synchronous Interaction Damping Control for DFIG Wind Turbines

Author: Andres E. Leon
Publication: IEEE Transactions on Power Systems
Publisher: IEEE
Date: Jan. 2015

Copyright © 2015, IEEE

Thesis / Dissertation Reuse

The IEEE does not require individuals working on a thesis to obtain a formal reuse license, however, you may print out this statement to be used as a permission grant:

Requirements to be followed when using any portion (e.g., figure, graph, table, or textual material) of an IEEE copyrighted paper in a thesis:

1) In the case of textual material (e.g., using short quotes or referring to the work within these papers) users must give full credit to the original source (author, paper, publication) followed by the IEEE copyright line © 2011 IEEE.
2) In the case of illustrations or tabular material, we require that the copyright line © [Year of original publication] IEEE appear prominently with each reprinted figure and/or table.
3) If a substantial portion of the original paper is to be used, and if you are not the senior author, also obtain the senior author's approval.

Requirements to be followed when using an entire IEEE copyrighted paper in a thesis:

1) The following IEEE copyright/ credit notice should be placed prominently in the references: © [year of original publication] IEEE. Reprinted, with permission, from [author names, paper title, IEEE publication title, and month/year of publication]
2) Only the accepted version of an IEEE copyrighted paper can be used when posting the paper or your thesis on-line.
3) In placing the thesis on the author's university website, please display the following message in a prominent place on the website: In reference to IEEE copyrighted material which is used with permission in this thesis, the IEEE does not endorse any of [university/educational entity's name goes here]'s products or services. Internal or personal use of this material is permitted. If interested in reprinting/republishing IEEE copyrighted material for advertising or promotional purposes or for creating new collective works for resale or redistribution, please go to http://www.ieee.org/publications_standards/publications/rights/rights_link.html to learn how to obtain a License from RightsLink.

If applicable, University Microfilms and/or ProQuest Library, or the Archives of Canada may supply single copies of the dissertation.

The permission below is for Chapter 2.

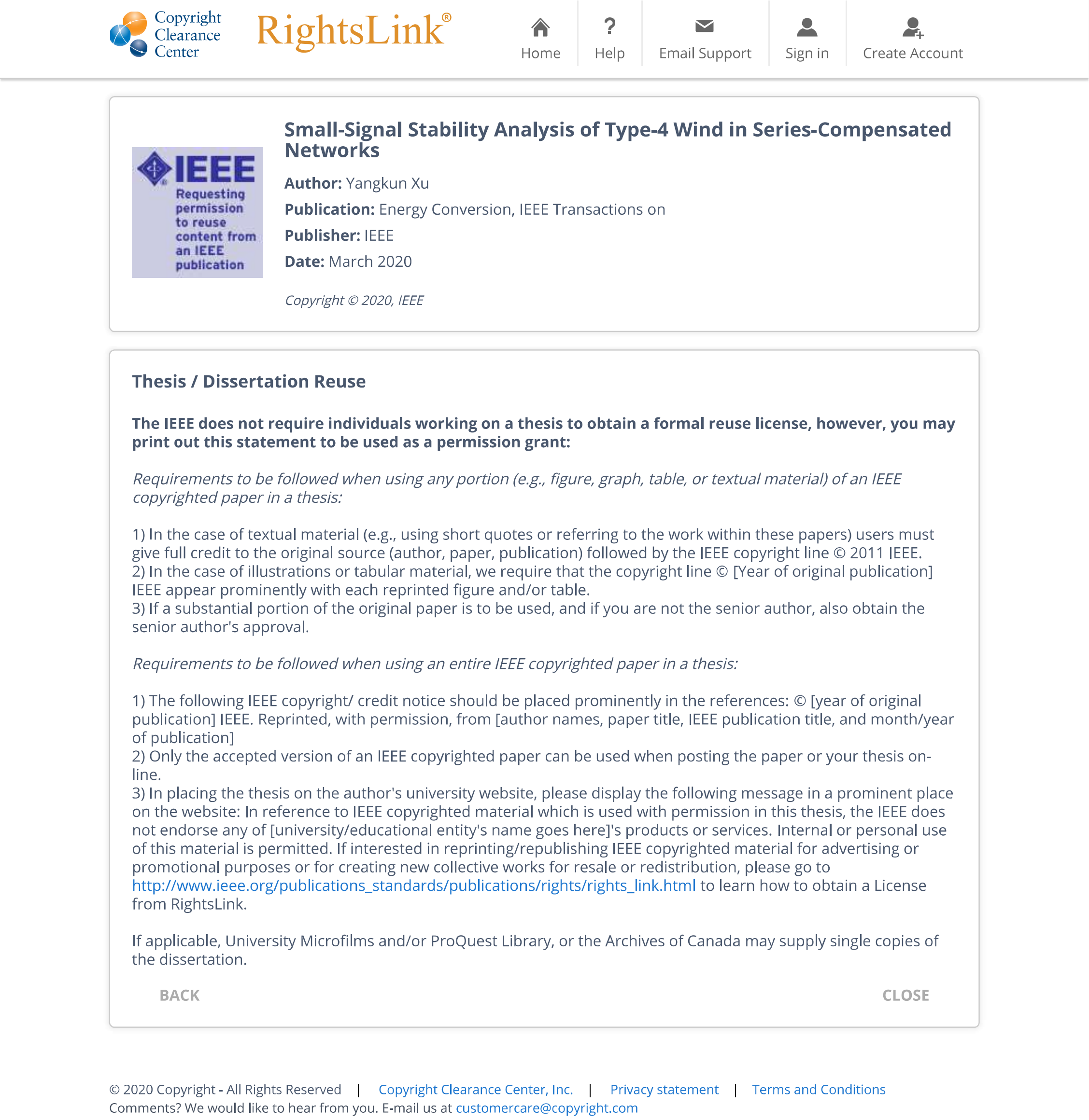

Small-Signal Stability Analysis of Type-4 Wind in Series-Compensated Networks

Author: Yangkun Xu
Publication: Energy Conversion, IEEE Transactions on
Publisher: IEEE
Date: March 2020

Copyright © 2020, IEEE

Thesis / Dissertation Reuse

The IEEE does not require individuals working on a thesis to obtain a formal reuse license, however, you may print out this statement to be used as a permission grant:

Requirements to be followed when using any portion (e.g., figure, graph, table, or textual material) of an IEEE copyrighted paper in a thesis:

1) In the case of textual material (e.g., using short quotes or referring to the work within these papers) users must give full credit to the original source (author, paper, publication) followed by the IEEE copyright line © 2011 IEEE.
2) In the case of illustrations or tabular material, we require that the copyright line © [Year of original publication] IEEE appear prominently with each reprinted figure and/or table.
3) If a substantial portion of the original paper is to be used, and if you are not the senior author, also obtain the senior author's approval.

Requirements to be followed when using an entire IEEE copyrighted paper in a thesis:

1) The following IEEE copyright/ credit notice should be placed prominently in the references: © [year of original publication] IEEE. Reprinted, with permission, from [author names, paper title, IEEE publication title, and month/year of publication]
2) Only the accepted version of an IEEE copyrighted paper can be used when posting the paper or your thesis on-line.
3) In placing the thesis on the author's university website, please display the following message in a prominent place on the website: In reference to IEEE copyrighted material which is used with permission in this thesis, the IEEE does not endorse any of [university/educational entity's name goes here]'s products or services. Internal or personal use of this material is permitted. If interested in reprinting/republishing IEEE copyrighted material for advertising or promotional purposes or for creating new collective works for resale or redistribution, please go to http://www.ieee.org/publications_standards/publications/rights/rights_link.html to learn how to obtain a License from RightsLink.

If applicable, University Microfilms and/or ProQuest Library, or the Archives of Canada may supply single copies of the dissertation.

© 2020 Copyright - All Rights Reserved | Copyright Clearance Center, Inc. | Privacy statement | Terms and Conditions
Comments? We would like to hear from you. E-mail us at customercare@copyright.com

About the Author

Yangkun Xu was born in 1991 in Xuancheng, China. He received his B.E. degree in Electrical Engineering from University of Shandong University of Technology, China, in 2012, and the M.E. degree from the Florida Institute of Technology, Melbourne, USA, in 2014. He is currently pursuing the Ph.D. degree in Electrical Engineering in the University of South Florida, Tampa, USA. His research interests include grid integration of renewable energies (Wind, solar and storage), modeling and control of Microgrid in islanded and grid-connected modes, power system stability analysis, design and development of electronic system.